

**Four-Dimensional Seismic Uncertainty
Quantification of the Hebron Field, Offshore
Newfoundland, Canada**

by

©Steven Lethbridge

A thesis submitted to the School of Graduate Studies in partial fulfillment of the requirements for the degree of Master of Science.

**Department of Earth Sciences
Memorial University of Newfoundland**

May 2022

St. John's, Newfoundland Labrador, Canada

Abstract

The time-lapse or four-dimensional (4D) seismic method is used to image subsurface changes within a reservoir through acquiring multiple three-dimensional (3D) seismic surveys over the same area some time apart. The concept extends from the assumption that any changes in the seismic signal between surveys are due to perturbations in subsurface properties (i.e. fluid saturation, pressure, and temperature) caused by the production of a reservoir interval. In this thesis, we determine velocity estimates for a synthetic production-related time-lapse seismic anomaly in the Pool 1 reservoir of the Hebron Field located within the Jeanne d'Arc Basin, offshore Newfoundland, Canada. We use a time-lapse seismic uncertainty quantification algorithm to compute 1,000,000 velocity estimates of the time-lapse seismic change in the Pool 1 reservoir. We compute these models across four Markov chains with an acceptance rate of 13.5 - 16.0% in 5.4 days on a standard desktop (i7 6700 3.4 GHz processor and 16 GB memory). Repeated sampling generates end ranges of possible velocity models representing the synthetic production-related time-lapse change created for Pool 1 in this thesis. Quantities of interest (QoI) are defined to highlight the ability of these velocity models to represent the size and magnitude of the true synthetic production time-lapse change. We plot statistical versions of the velocity models recovered by an arbitrary Markov chain to visually showcase the recovered mean and maximum likelihood model representations of the true synthetic time-lapse velocity perturbation.

Acknowledgements

Firstly, I would like to thank my supervisors, Dr. Alison Malcolm and Dr. J. Kim Welford. Both Kim and Alison were essential in providing feedback on the writing, material, presentation, and planning of this entire thesis. I enjoyed our weekly chats over coffee despite most of them having to take place over Webex. These conversations were not always focused on the science at hand, but they kept me focused on the task at hand.

Although Dr. Maria Kotsi was not a direct supervisor on this project, without her input and help, this thesis would not have been the same without her. For that, I would like to express my sincerest gratitude.

Next, I would like to thank both Dr. Alison Malcolm and Dr. J. Kim Welford's research groups for their input and feedback throughout the work completed in this thesis.

I would like to thank the many friends I have made at Memorial University of Newfoundland over the last six years across my undergraduate and graduate degrees. I would like to thank Jacob Newman and Miguel Shano specifically for all the support, advice, fun times, and Friday afternoons at the Breezeway (when it was still open) over these last six years.

To my girlfriend Jana Hall and my entire family, I would like to thank them for their support in every way imaginable throughout the completion of this degree.

Finally, I would like to thank the following organizations: Chevron Canada, Natural Sciences and Engineering Research Council of Canada, and InnovateNL for funding this work.

Table of Contents

Abstract	ii
Acknowledgments	iii
List of Tables	x
List of Figures	xx
1 Introduction and Overview	1
1.1 Motivation	1
1.2 Seismic Reflection Method	2
1.2.1 Time-Lapse Seismic Studies	4
1.3 Full Waveform Inversion	6
1.3.1 Full Waveform Inversion Applied to the Time-Lapse Case . . .	6
1.4 Uncertainty Quantification in Seismic Imaging	7
1.4.1 Uncertainty Quantification Applied to the Time-Lapse Case .	8
1.5 Data	8
1.5.1 Seismic Data Set	9
1.5.2 Well Data	11
2 Geologic Overview	13

2.1	The Jeanne d’Arc Basin	15
2.1.1	Structure of the Jeanne d’Arc Basin	15
2.1.2	Lithostratigraphy of the Jeanne d’Arc Basin	17
2.1.3	Petroleum System of the Jeanne d’Arc Basin	18
2.2	Hebron Field Overview	21
2.2.1	Structure of the Hebron Field	23
2.2.2	Reservoir Geology of the Hebron Field	24
3	Seismic Data Interpretation	26
3.1	Fault Interpretation	26
3.1.1	Quality Control of Fault Interpretations	30
3.2	Horizon Interpretation	31
3.2.1	Quality Control of Horizon Interpretations	35
3.2.2	Horizon Interpretation Outputs	37
4	Hebron Field Pool 1 Geological Model	39
4.1	Pool 1 Geological Model Inputs	40
4.1.1	Pool 1 Geological Model 3D Surfaces	40
4.1.2	Pool 1 Geological Model Well Log Preparation	40
4.1.3	Pool 1 Geological Model Boundary Polygon	44
4.2	Building the Geological Model in Petrel	46
4.3	Pool 1 Geological Model Results	51
4.3.1	Quality Control of the Pool 1 Geological Model Outputs	52
4.3.2	Updating the Pool 1 Geological Model	53
5	Hebron Field Baseline Velocity Model	57
5.1	Hebron Field Baseline Velocity Model Inputs	58
5.1.1	Sonic Log Preparation	59

5.2	Hebron Field Baseline Velocity Model - Attempt 1	61
5.3	Hebron Field Baseline Velocity Model - Attempt 2	63
5.3.1	Attempt 2 - Hebron Field Baseline Velocity Model Results . .	68
5.3.2	Quality Control of the Hebron Field Baseline Velocity Model .	69
6	Hebron Field Monitor Velocity Model	72
6.1	Log Based Fluid Substitution	72
6.1.1	Fluid Properties of the Pool 1 Reservoir	74
6.1.2	Mineral Properties of the Pool 1 Reservoir	76
6.1.3	Model Based Well Logs Generated for the Fluid Substitution .	76
6.1.4	Log Based Fluid Substitution Results	78
6.2	Fluid Substitution Based Monitor Model	81
7	Time-lapse Seismic Uncertainty Quantification	89
7.1	4D Multi-Parameter Metropolis-Hastings Seismic Uncertainty Quan- tification Algorithm	89
7.1.1	Algorithm Breakdown	90
7.1.2	Degrees of Freedom	95
7.2	4D Seismic Uncertainty Quantification Analysis of the Hebron Field Pool 1	100
7.2.1	Degree of Freedom Representations of the Pool 1 Anomaly . .	101
7.2.2	Time-Lapse Seismic Uncertainty Quantification Results for the Hebron Field	102
8	Discussion	111
8.1	Interpretation of the Time-Lapse Seismic Results	111
8.2	Implications of the Time-Lapse Seismic Uncertainty Quantification .	112
8.3	Limitations to the Time-Lapse Seismic Uncertainty Quantification Study	113

8.4	Additional Applications of the Time-Lapse Seismic Uncertainty Quantification Method	115
8.4.1	Forecast Ideal Timing for Monitor Seismic Survey(s)	116
8.4.2	De-risking Geological Targets	116
9	Conclusions and Future Work	118
9.1	Conclusions	118
9.2	Future Work	119

List of Tables

1.1	Table showing the acquisition parameters of the 2013 Hebron baseline survey. (from WesternGeco, 2013).	11
1.2	Table showing the wells and some of their important corresponding logs available for this study.	12
3.1	Table indicating the seismic character that was picked for each horizon. The color fill for each horizon corresponds to the color of the interpretation for that formation.	32
5.1	Velocity model desired cell sizes and their requisite number of layers. Layer thicknesses (distance measured) were measured on IL 9281 between the intersection with XLs 7201 and 7361.	66
6.1	Table indicating fluid parameters input into the RokDoc software to generate accurate fluid properties for the Pool 1 reservoir of the Hebron Field. This fluid information is from the Hebron Field development plan submitted to the CNLOPB for field development approval, thus represents the reservoir prior to production. (after ExxonMobil, 2011)	75
6.2	Table showing fluid parameters calculated using RokDoc, which represents the oil contained in the Pool 1 pore space from the inputted parameters shown in Table 6.1.	76

6.3 P-wave velocity fluid substitution scenarios used for each well for the perturbed monitor velocity model.	82
--	----

List of Figures

1.1	The convolution model for a seismic reflection trace showing the relationship between the geology of the subsurface to the outputted seismic trace. (after Kearey et al., 2002)	3
1.2	The seismic effect of reservoir hydrocarbon filled pore spaces being replaced with water during the production of a reservoir. (after Wright, 2004)	4
1.3	Base map for the 2013 ExxonMobil 3D seismic survey for the Hebron area. The magenta polygon is the production licence for the Hebron field and the green arrow points northward.	10
2.1	A reconstruction of the continental plates at the Late Jurassic time. Marked in stipple pattern are the locations of Mesozoic rift basins. Note that not all the Mesozoic rift basins located in this area are shown. (from Sinclair et al., 1994, with the permission of John Wiley and Sons License Number: 5239341110752)	14
2.2	a) Map showing the sedimentary basins and structure of the Grand Banks; b) map of the Jeanne d’Arc Basin showing structural features of the basin. (from Tankard et al., 1989 AAPG©1997, reprinted by the permission of the AAPG whose permission is required for further use.)	16

2.3	Structural framework map of the Jeanne d’Arc Basin indicating major faults mapped within the basin. (from Tankard et al., 1989 AAPG©1997, reprinted by the permission of the AAPG whose permission is required for further use.)	17
2.4	Jeanne d’Arc Basin lithostratigraphy chart. (from https://www.cnlopb.ca)	19
2.5	Location of the Hebron field with respect to St. John’s.	21
2.6	Hebron Field map highlighting the position of Figure 2.7. The black lines represent bounding faults for the three main fault blocks in the field. The green arrow points northward. (after Cornaglia & McNeill, 2018)	22
2.7	Schematic cross-section showing the structure of the Hebron field. (after Cornaglia & McNeill, 2018)	22
2.8	Ben Nevis depth structure map for the Hebron field showing the locations of the current development wells. The Ben Nevis surface is displayed in mTVDss which is true vertical depth below mean sea level in meters. (from https://www.cnlopb.ca)	24
3.1	Workflow for interpretation of the seismic data set.	26
3.2	Modified version of Figure 2.3, with the location of the Hebron field circled in red. (after Tankard et al., 1989 AAPG©1997, reprinted by the permission of the AAPG whose permission is required for further use.)	27
3.3	Example of a depth slice from the seismic survey at -2200 m depth with shown discontinuities in the seismic data related to the faulting of the subsurface. The red arrows highlight some of the fault induced seismic discontinuities and the green arrow points northward.	28

3.4	IL 8481 a) uninterpreted seismic section b) fault interpreted seismic section.	29
3.5	Comparison of fault interpretations to seismic data in 3D; Depth Slice -2200m (Figure 3.3) with a sample subset of fault interpretations from Pool 1 projected. The green arrow points northward.	30
3.6	3D view of IL 9121 overlain by interpretations of the faults bounding Pool 1 within the Hebron Field. The green arrow points northward.	31
3.7	Workflow followed for the horizon interpretations.	32
3.8	IL 6721 highlighting the North Trinity H-71 well. a) seismic section with only the fault interpretation b) horizon interpreted seismic section.	34
3.9	XL 4961 highlighting the Brent's Cove I-30 well. a) seismic section with only the fault interpretation b) horizon interpreted seismic section.	35
3.10	XL 8321 highlighting the use of XLs for horizon interpretation QC. a) seismic section with only the fault interpretation b) horizon interpreted seismic section; where the cyan crosses represent the A Marker horizon interpretation completed on IL seismic lines.	36
3.11	Example of a completed horizon interpretation shown in a 2D map view; shown here is the A marker horizon. The green arrow points northward.	37
3.12	An example 3D surface generated from an interpreted seismic horizon throughout the survey area; shown here is the A marker surface generated from the A marker horizon. The green arrow points northward.	38
4.1	Workflow followed to build the geological model of the Pool 1 reservoir within the Hebron Field.	39

4.2	Example well log digitization using the Didger 5 software highlighting the log by log; where the red curve is the density (RHOB) log for a section of the Hebron L-93 3 well and the overlain yellow line is the drawn polyline used to extract the digitized log values. This process is completed for each curve one at a time. Hence why only the polyline for the density log is shown.	41
4.3	Example well log digitization master LAS file created using the Didger 5 software.	42
4.4	Enlarged view of digitized well logs for the Hebron L-93 5 well, showcasing the quality of the logs created through the digitization process. GR is the gamma ray log, DRHO is the density correction log, TNPH is the neutron log, DTSH is the shear wave travel time, and DTCO is the compressional wave travel time.	43
4.5	Pool 1 and Pool 2 combined geological model; where Pool 2 is the eastern fault block and Pool 1 is everything west of Pool 2 (from Exxon-Mobil, 2011).	45
4.6	Pool 1 boundary (red polygon) for the geological model shown in this thesis overlain on top of the interpreted Top Ben Nevis surface; the magenta polygon is the production licence polygon for the Hebron Field and the green arrow points northward.	46
4.7	Geological Model Workflow Step 1: Define 3D grid; the XY boundary is the Pool 1 polygon in Figure 4.6 and the Z boundary comprise the four surfaces explained in Section 4.1.1.	47
4.8	Geological Model Workflow Step 2: Define layering; the number of layers is calculated using Equation 4.2, where the desired cell size for the model is 2 m.	48

4.9	Geological Model Workflow Step 3: Geometrical modeling to create zones in the geological model; the Nautilus zone is grey, Ben Nevis zone is beige, and the Avalon zone is blue-grey.	49
4.10	Geological Model Workflow Step 4: well log up-scaling; up-scales the high resolution (0.1 m) log values to the 2 m geological model cell size; shown here is the up-scaled density well log values for the Hebron I-13, Hebron M-04, Hebron D-94, and Hebron L-93 5 wells. The green arrow points northward.	50
4.11	Geological Model Workflow Step 5: petrophysical modeling tool; shown here is the 3D density model created by propagating the up-scaled well log values for the Hebron I-13, Hebron M-04, Hebron D-94, and Hebron L-93 5 wells. The green arrow points northward.	51
4.12	Cross-section through the 3D density model showing projections of 3 well penetrations that are inputs into the model.	52
4.13	Hebron I-13 well log section with caliper (CALI), density (RHOB), and porosity shown; the porosity color fill cutoff is set at 14%. The black box indicates the region of borehole breakout.	53
4.14	Updated cross-section through the 3D density model showing projections of 8 well penetrations that are inputs into the model. Note the continuous high density for the Nautilus shale zone compared to Figure 4.12.	54
4.15	Cross-section through the 3D porosity model showing projections of 8 well penetrations that are inputs into the model.	55

4.16	Updated petrophysical modeling step of the geological modeling process. This is an updated version of Figure 4.11 with the addition of five production wells: Hebron L-93 2, Hebron L-93 3, Hebron L-93 7, Hebron L-93 9, and Hebron L-93 12. The green arrow points northward.	56
5.1	Benchmark velocity model. This is a section from the velocity model that was used to depth convert the seismic data used in this thesis from time and was built using an extensive FWI process. (from CGG, 2015b)	58
5.2	Sonic calibration settings within the Petrel software showing how the sonic well log was calibrated with itself.	59
5.3	Sonic calibration outputs showing the vertical uncontaminated drift curve (2nd track). The input sonic data are in red on the 3rd track, and the velocity data used for this well are in red on the 4th track. .	60
5.4	Settings for Petrel’s Advanced velocity model tool used to construct the first attempt of the Hebron Field Baseline Model.	62
5.5	IL 9121 displaying the first attempt at a velocity model for the Hebron Field; shown on the figure are Pool 1 faults for a frame of reference and the color bar was selected to resemble the benchmark model color bar.	63
5.6	Workflow used to build the second attempt of the Hebron Field baseline velocity model.	64
5.7	Velocity Model Workflow - Define 3D grid; The X, Y, and Z boundaries are defined by the twelve input surfaces.	64
5.8	Zones defined by the twelve input surfaces within the velocity model.	67
5.9	Survey setup for the 3D velocity seismic cube created using the 3D-gridded velocity property.	68

5.10	Velocity model using the 3D-grid based approach outlined in Figure 5.6. Line location is approximately IL 9089, and the color bar is set to match the benchmark model.	69
5.11	Brent’s Cove I-30 (Left) and West Bonne Bay C-23 (Right) velocity logs highlighting the need to trim select velocity logs and keep others intact.	70
5.12	Velocity model using the 3D-grid based approach outlined in Figure 5.6 after QCing of select velocity logs. Line location is approximately IL 9089, and the color bar is set to match the benchmark model. . . .	71
6.1	Illustration of the general fluid substitution problem for a rock originally saturated with Fluid A that is being replaced by Fluid B. (after Johnston, 2013)	74
6.2	Gassman predictions for the P-wave velocity change for a heavy oil, oil, and gas initial fluid scenario where the replacement fluid is water. (from Johnston, 2013)	75
6.3	Example model well log set showing the density, porosity, P-wave, and S-wave model logs for the Hebron M-04 well used within the log based fluid substitution within the RokDoc software. The well data is displayed in true vertical depth (TVD), with Top BNEV indicating the top of the Ben Nevis sandstone and OWC is the oil-water contact. . .	78
6.4	Hebron L-93 7 well log showcasing the fluid substitution process updating the P-wave model log from 100% oil (black) to 50-50 oil-water (blue) to 100% water (red). The well log is shown in measured depth along the wellbore.	80
6.5	Monitor velocity model created using the fluid substituted log data along IL 9281.	83

6.6	Residual between the baseline velocity model and monitor velocity model created using the fluid substituted log data along IL 9281. . . .	84
6.7	Residual between the baseline velocity model and monitor velocity model shown in a 3D map view, the red polygon represents the Pool 1 geological model boundary and the green arrow points northward. . .	85
6.8	Anchor Well locations (red circles) surrounding the Hebron fault block of the Pool 1 reservoir (red polygon) and along the IL 9281 (yellow line) overlain on the top Ben Nevis reservoir 3D seismic surface, the green arrow points northward.	86
6.9	Residual between the baseline velocity model and monitor velocity model created using the fluid substituted log data along IL 9281; additional anchor wells shown as the vertical red lines.	87
6.10	Residual between the baseline velocity model and monitor velocity model shown in a 3D map view. Compared to Figure 6.7, the residual velocity change stays within the Pool 1 polygon. Anchor Well locations (grey squares) surrounding the Hebron fault block of the Pool 1 reservoir (red polygon) and the green arrow points northward.	88
7.1	Illustration of the Markov Chain Monte Carlo method. (from Kotsi, 2020)	90
7.2	The pseudocode showing the steps of the Adaptive Metropolis Hastings algorithm used for the 4D seismic inversion. (modified from Kotsi, 2020)	92
7.3	a) Example Φ matrix b) Singular values of the example Φ matrix which decay after the first 300 values. c) $\vec{\alpha}$ coefficients (From Kotsi et al., 2020)	98
7.4	a) Example true smoothed time-lapse change b) reconstruction of the example time-lapse change using 300 $\vec{\alpha}$ coefficients c) $\vec{\alpha}$ coefficients (From Kotsi, 2020)	99

7.5	Smoothed Hebron Field Pool 1 anomaly with the local domain (white box) highlighted showing the area used in the uncertainty quantification algorithm.	100
7.6	a) Pool 1 Φ matrix b) Singular values of the Pool 1 Φ matrix which decay after the first 1400 values. c) $\vec{\alpha}$ coefficients.	101
7.7	a) Reconstruction of the Pool 1 anomaly (Figure 7.5) using the entire alpha matrix (6255 DoF) b) 16 DoF representation c) 25 DoF representation d) 36 DoF representation. The plot area is the local domain which represents a 2D cross-section view of the Hebron fault block.	102
7.8	Histograms of the recovered $\vec{\alpha}$ coefficients for the four Markov chains computed for 100,000 iterations on the 36 DoF representation of the Pool 1 time-lapse anomaly. Each colored line represents a different chain, with a random chain selected to be the displayed histogram. The green line highlights the true value for the given coefficient.	104
7.9	Histograms of the recovered $\vec{\alpha}$ coefficients for the four Markov chains computed for 100,000 iterations on the 25 DoF representation of the Pool 1 time-lapse anomaly. Each colored line represents a different chain, with a random chain selected to be the displayed histogram. The green line highlights the true value for the given coefficient.	105
7.10	Histograms of the recovered $\vec{\alpha}$ coefficients for the four Markov chains computed for 250,000 iterations on the 36 DoF representation of the Pool 1 time-lapse anomaly. Each colored line represents a different chain, with a random chain selected to be the displayed histogram. The green line highlights the true value for the given coefficient.	107

7.11	a) True Pool 1 time-lapse change with the white dashed line showing the portion of the local domain over which the area calculation was completed. b) Recovered histograms for the fault block/time-lapse change area calculation for the four Markov chains. Each colored line represents a different chain, with a random chain selected to be the displayed histogram. The green line highlights the true value for the given coefficient.	108
7.12	\hat{R} criteria for the average velocity and area QoIs for the four Markov chains computed at 250,000 iterations each. The dashed line is plotted at 1.1 to show the value at which the QoIs converge.	109
7.13	a) 36 DoF representation of the true Pool 1 time-lapse anomaly. b) Mean recovered model, c) maximum likelihood model, and d) standard deviation for an arbitrary Markov chain computed for 250,000 iterations. The plot area is the local domain which represents a 2D cross-section view of the Hebron fault block.	110
8.1	a) The true time-lapse anomaly within the Hebron fault block, with the approximate location of the local domain highlighted by the dashed white box. Note, the well locations on this seismic IL are being displayed out of plane (i.e locations of the wells are only approximate within the fault block). b) Smoothed true time-lapse anomaly within the Hebron fault block. c) 36 DoF representation of the time-lapse anomaly. d) Maximum likelihood velocity estimate for the time-lapse anomaly.	112

Chapter 1

Introduction and Overview

1.1 Motivation

The time-lapse or four-dimensional (4D) seismic method is a geophysical exploration tool which is used to detect fluid movements within the subsurface. The seismic reflection method is a technique traditionally used to map the structure of the subsurface; through this method, potential reservoir targets are imaged and identified. When acquiring two three-dimensional (3D) seismic reflection surveys over a common location some time apart, changes in the subsurface seismic response can be attributed to fluid saturation, pressure, and temperature changes within the subsurface (i.e. a reservoir), provided there are no acquisition, processing, or noise discrepancies between the two surveys (Lumley, 2001). Applying this technology to a producing hydrocarbon field allows for the movement of the hydrocarbons in the subsurface to be imaged throughout the life cycle of the field, providing useful information about the remaining reserves. Much uncertainty exists within the processes of seismic imaging. Understanding this uncertainty is important when dealing with 4D seismic data as it requires comparing two separate seismic images to each other. Without understanding this uncertainty,

making decisions based on 4D seismic changes can be a difficult process.

The focus of this thesis is on quantifying the 4D seismic uncertainty associated with the Hebron field located within the Jeanne d’Arc Basin, offshore Newfoundland, Canada. We do this through the interpretation of seismic data acquired over the field, in conjunction with available well data, to build an accurate velocity model for the Hebron field. We then complete a percentage-based fluid substitution on the wells drilled within the Pool 1 reservoir to generate a synthetic post-production velocity model. These two velocity models are treated as the two surveys needed for the synthetic time-lapse study of the field. Using a 4D multi-parameter Metropolis-Hastings seismic uncertainty algorithm presented by Kotsi (2020), the uncertainty in the time-lapse change between the two velocity models is examined.

1.2 Seismic Reflection Method

The seismic reflection method is a geophysical exploration technique used to image the structure of the subsurface. This method depends on the layers of the subsurface having different acoustic impedances,

$$Z = \rho V, \tag{1.1}$$

to distinguish them; where ρ is the density and V is the velocity of the subsurface layer. The subsurface is imaged by propagating waves of energy through the subsurface and these waves interact with the subsurface layers with differing impedances. From this interaction, some of the energy will be reflected off the boundary while the rest will be transmitted. The reflected energy is measured on the surface by receivers and this data can then be used to create a seismic image or section of the subsurface. The

zero-offset reflection

$$RC = \frac{Z_2 - Z_1}{Z_2 + Z_1} \quad (1.2)$$

where Z_2 is the acoustic impedance of the second layer and Z_1 is the acoustic impedance of the first layer and the zero-offset transmission

$$TC = 1 - RC \quad (1.3)$$

coefficients determine the energy that is either reflected or transmitted from a given layer; the zero-offset approximation is acceptable for short-offset surveys for the reflection and transmission coefficients. Figure 1.1, shows how the input seismic energy (input pulse) creates the seismic trace that can then be processed appropriately into a seismic section.

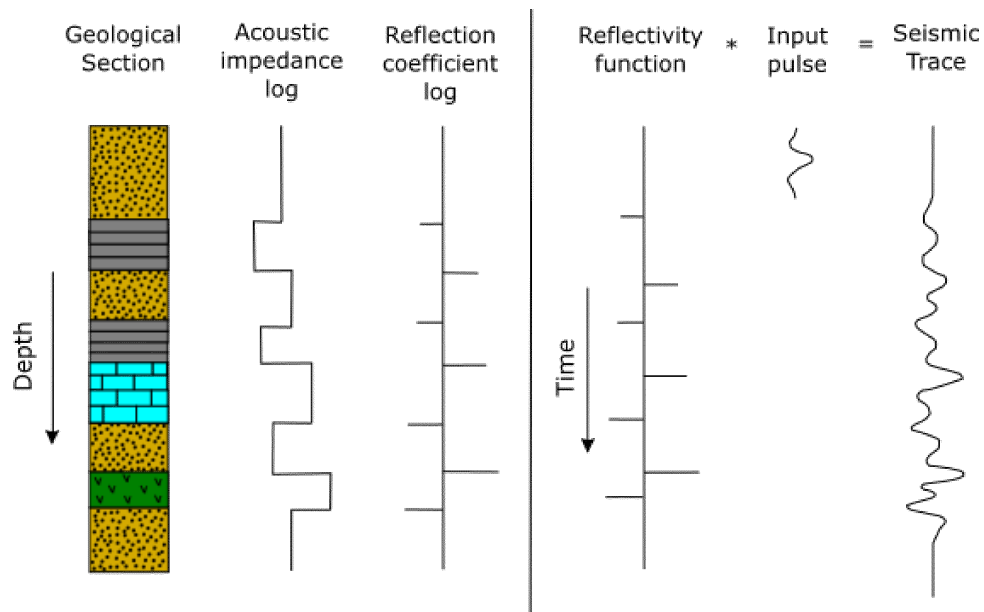


Figure 1.1: The convolution model for a seismic reflection trace showing the relationship between the geology of the subsurface to the outputted seismic trace. (after Kearey et al., 2002)

1.2.1 Time-Lapse Seismic Studies

The 4D seismic approach is a variation of the seismic reflection method, in which two or more 3D seismic surveys are acquired over the same area over some time interval. The method is aimed at imaging fluids within the subsurface, specifically during the production of a reservoir. The first seismic survey is the baseline survey and is traditionally acquired pre-production with subsequent monitor survey(s) acquired throughout the field's lifetime. 4D seismic surveys are inferred to image fluid changes within a reservoir through fluid saturation and pressure effects on both density and seismic velocity of the reservoir (Figure 1.2), since these properties directly impact the amplitude of the seismic signal (Lumley, 2001).

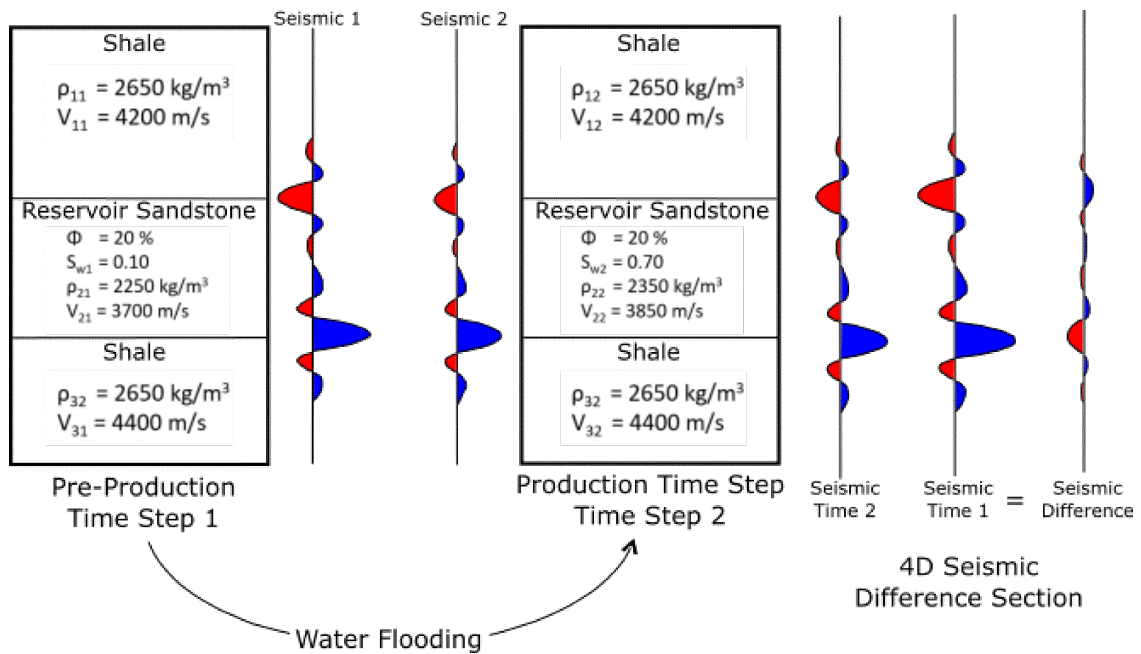


Figure 1.2: The seismic effect of reservoir hydrocarbon filled pore spaces being replaced with water during the production of a reservoir. (after Wright, 2004)

An example of a 4D seismic response is shown in Figure 1.2. Removing the baseline survey seismic response (Seismic Time 1) from the monitor survey response (Seismic Time 2) creates the time-lapse change (Seismic Difference) between the two surveys.

The quality and interpretability of the 4D changes between two seismic surveys are dependent on the quality and repeatability of the surveys. Since the surveys need to be as comparable as possible, much care must be put into the acquisition of the monitor survey. The most important navigational aspect of the monitor survey is recreating the same source-receiver locations as the baseline survey (Naess, 2006). This is easiest for baseline surveys designed with 4D seismic studies in mind, but older vintage pre-development seismic surveys that were not designed for 4D surveys are still useable as baseline surveys. Generating a similar monitor survey is dependent on navigation data to recreate the source and receiver locations, on approximately the same signal to noise ratios, and on applying similar amplitude recovery processing steps. When using older vintage surveys, cross-equalization processing steps are needed to correct for non-repeatability issues (Lumley et al., 2003).

The cost of acquiring and replicating a monitor survey(s) is very expensive. Consequently, 4D seismic feasibility analyses are essential prior to undertaking time-lapse studies. Lumley et al. (1997) created a quantitative score analysis technique that assesses the risk of 4D seismic projects. If a field passes the feasibility analysis, seismic modeling is completed to determine the possible responses for a given field. This modeling involves using known rock and fluid properties from well data for reservoir intervals to build a pre-production baseline field model. With this model, synthetic seismic data can be generated. The synthetic monitor data are created using expected reservoir conditions such as fluid saturation and pressure to predict possible effects on both the density and seismic velocity of the reservoir (Lumley, 2001). If this modeling predicts a sufficient time-lapse change (i.e. detectable change above noise levels) in seismic character, then the field passes the feasibility criterion for 4D seismic studies.

1.3 Full Waveform Inversion

Full waveform inversion (FWI) is a sophisticated seismic imaging technique used to build high resolution velocity models by solving the wave equation (Virieux & Operto, 2009). FWI is an iterative process that minimizes the misfit between synthetic data generated in a starting model and a set of recorded data. This process first involves generating a starting velocity model for the subsurface. This starting model is then input into a wave equation solver and the output data are then compared with the recorded data. If the residuals between the models are larger than a set cutoff, this residual is back-propagated to calculate the gradient, from which we compute a model perturbation. This perturbation is added to the initial velocity model. This process is iterated until there is an acceptable misfit between the synthetic data and the recorded data. FWI fits lower frequencies first before fitting higher frequencies.

1.3.1 Full Waveform Inversion Applied to the Time-Lapse Case

Due to the high resolution of the FWI technique for imaging the subsurface, it is a useful tool to apply to the time-lapse seismic case where the objective is to recover small details of the subsurface with a high degree of certainty (Asnaashari et al., 2015). FWI has an advantage over other time-lapse analysis techniques as it does not require the identification of the seismic phase, as FWI fits all the phases of the seismic data at once (Asnaashari et al., 2015). FWI is robust when it comes to recovering amplitude changes within the subsurface but is poorer at determining the kinematics of the wave equation properly due to cycle-skipping and inaccurate starting models (Kotsi et al., 2019a; Pratt, 1999). FWI for the 4D case typically involves first computing FWI for the velocity model of the baseline survey, starting with a smooth initial model, and

then using this baseline velocity model as the starting initial model for the subsequent monitor survey(s). The time-lapse seismic change is then computed by subtracting the output monitor velocity model from the baseline output velocity model; this 4D FWI process is referred to as a sequential FWI approach (Kotsi, 2020; Asnaashari et al., 2015). There are other approaches such as parallel FWI, which completes the FWI for both the baseline and monitor models independently and double-difference FWI, which is similar to the sequential approach but adds an additional step of computing synthetic data from the FWI completed on the baseline data; these synthetic data are then added to the data difference (monitor - base) with the FWI being completed on this new composite data set (Kotsi, 2020; Plessix et al., 2010; Zhang & Huang, 2013).

1.4 Uncertainty Quantification in Seismic Imaging

Seismic imaging has a long list of uncertainties associated with the process, ranging from acquisition to processing to interpretation of the data. Being able to quantify this uncertainty is important as it allows one to understand which portions of the data can be trusted and which portions of the data may be misleading. Any representation of the subsurface using seismic imaging relies on a velocity model to accurately depict the structures. A more complex structure relies on having a better velocity model than what is required for a subsurface containing flat horizons. Therefore if one can quantify the uncertainty of the velocity model for a given data set, then the corresponding output image of the subsurface can have a measure of certainty associated with it.

1.4.1 Uncertainty Quantification Applied to the Time-Lapse Case

Being able to quantify the uncertainty of the baseline survey and monitor survey(s) in time-lapse seismic studies is imperative for making decisions based on the change in the seismic response. In using FWI for recovering the velocity models for the baseline survey and monitor survey(s), it is important to remember that FWI outputs a single model from a range of possible models that could equally fit the data (Kotsi, 2020). Bayesian statistics can be used to quantify the likelihood that a given velocity model will fit a set of data; the posterior probability, in this case, is set up as,

$$p(m|d) = \frac{p(d|m)p(m)}{p(d)}, \quad (1.4)$$

where $p(m|d)$ is the probability that a given velocity model, m , is the answer for some data, d , and where $p(d|m)$ is the likelihood function (Kotsi et al., 2018).

This thesis uses a 4D multi-parameter adaptive Metropolis Hastings uncertainty quantification algorithm proposed by Kotsi (2020). This method uses Discrete Cosine Transform (DCT) coefficients to lower the number of parameters or degrees of freedom (DOFs) needed to be recovered to show the 4D change between two velocity models (Kotsi et al., 2019b). This is the method of choice for this thesis as it allows for the use of multiple shots and multiple frequencies, and it recovers a smoother variation compared to that of a grid parameterization approach (Kotsi, 2020).

1.5 Data

The data used in this thesis were obtained from the Canada-Newfoundland Offshore Petroleum Board (CNLOPB) and/or donated to the Memorial University of

Newfoundland by IHS Energy. The data used here are described below in detail. Briefly, they include a seismic survey over the Hebron field offshore Newfoundland within the Jeanne d'Arc Basin as well as wells within and surrounding the survey location.

1.5.1 Seismic Data Set

The seismic survey used in this thesis is the 2013 ExxonMobil Canada Properties 3D seismic survey of the Hebron field (CA-3000960-GOA) (Figure 1.3). Processed images of the survey were obtained from the CNLOPB and comprise 111 2D seismic lines, with a spacing of 0.5 km between each line and depth slices every 200 m. The seismic line images were converted to SEG-Y format, using Tif2segy, a script which converts images of seismic sections into segy files utilizing Seismic Unix and Netpm tools (McIlroy, 2014; MacRae, 2001). One disadvantage to obtaining the data this way is that all of the true amplitude information from the seismic data is lost when using this specific software.

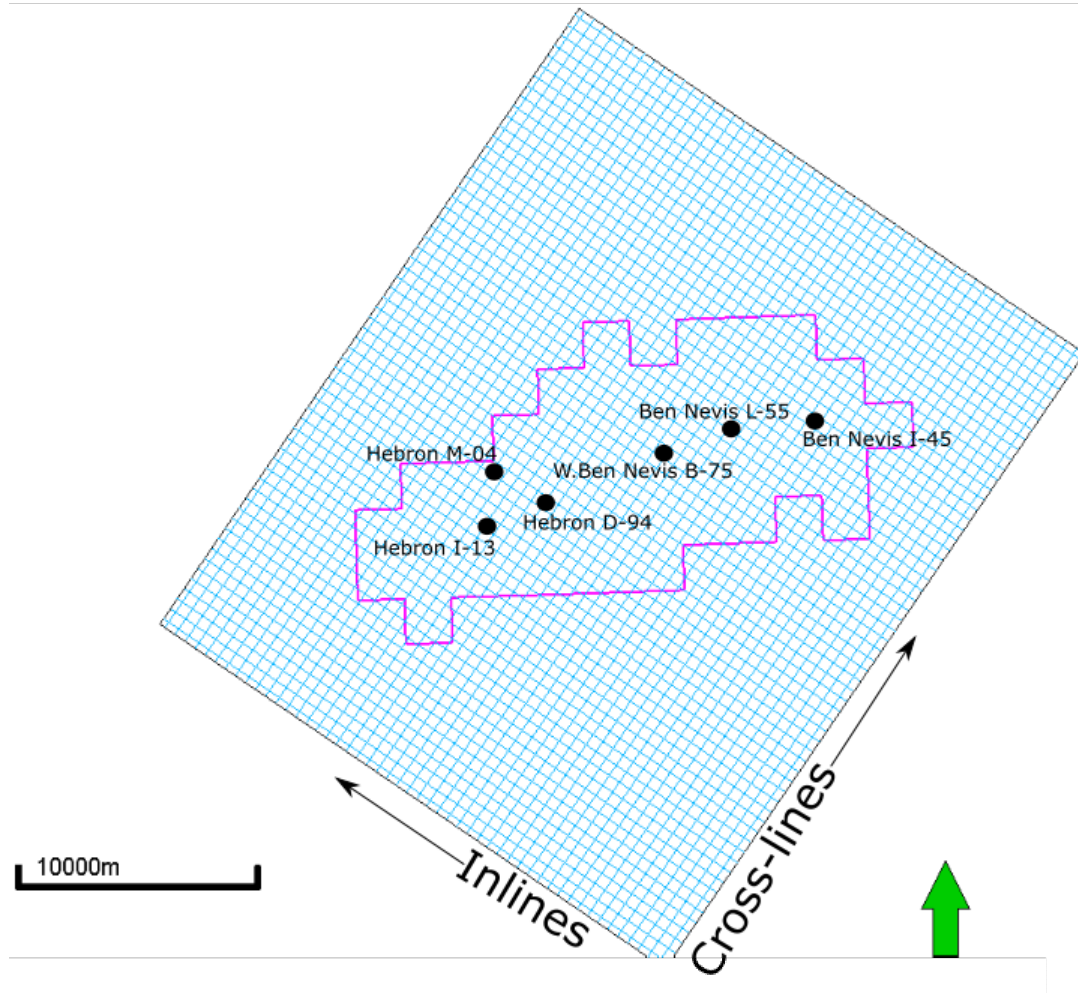


Figure 1.3: Base map for the 2013 ExxonMobil 3D seismic survey for the Hebron area. The magenta polygon is the production licence for the Hebron field and the green arrow points northward.

The survey was acquired in 2013 by WesternGeco with the M/V Vespucci, from June 17, 2013 to September 11, 2013 (CGG, 2015a). The survey was designed to be the baseline survey for future time-lapse studies of the field. It covers an area of approximately 475 km² and the acquisition parameters are listed in Table 1.1 (CGG, 2015a; WesternGeco, 2013). The processing of the seismic survey was completed by CGG, and the focus of the processing was to preserve amplitude information, to better image the reservoir units, and to minimize fault sag (CGG, 2015a).

Parameters	Remarks
Cable Type	Nessie-6
Number of streamers	12
Hydrophone interval (m)	3.125
Streamer length (m)	6000
Streamer depth (m)	18
Streamer separation (m)	50
Recording format	SegD 8058
Recording format revision	Rev 3 (One Sequence per tape delivered to the client) 8s – Note the actual record length required was 0-8 however an additional 1s was acquired either side to allow for filter edge effects therefore Vespucci recorded -1 to 9 seconds
Recording length (sec)	
Sample rate (ms)	2
Filter(s)	Lo-cut recording filter (Hydrophone) (Hz- dB/Oct) 1.5-18 Hi-cut recording filter (Hz - dB/Oct) 80% Nyquist 200-477
Gain Control	IFP Gain Control
Polarity Test	Untested
Source type	Bolt Gun array
Number of source arrays	2
Source array separation (m)	25
Shotpoint interval (m)	25
Array volume per source (In ³)	3558
Operating pressure (psi)	2000
Source depth (m)	6
Source type	Bolt Gun array
Fold	60

Table 1.1: Table showing the acquisition parameters of the 2013 Hebron baseline survey. (from WesternGeco, 2013).

1.5.2 Well Data

Table 1.2 shows the catalog of well information used for this thesis. The majority of these wells are TIFF files of well log information available through the CNLOPB, with the ones labeled as “Digitized” having been donated to Memorial University of Newfoundland by IHS Energy. The important information for the wells obtained from the CNLOPB were digitized and converted to LAS format to be used by Petrel using the Didger 5 software. The well information contribute to building an accurate interpretation and velocity model for the Hebron field.

Well	Directional Survey	Gamma Ray	Denisty	Netutron Density	Sonic	Resistivity	Porosity	Digitized
Avondale A-46	✓	✓	✓	✓	✓	✓	✗	✗
Ben Nevis I-45	✓	✓	✓	✓	✓	✓	✗	✓
Ben Nevis L-55	✓	✓	✓	✓	✓	✓	✓	✓
Brents Cove I-30	✓	✓	✓	✓	✓	✓	✗	✗
Cape Race N-68	✓	✓	✓	✓	✓	✓	✗	✗
Hebron D-94	✓	✓	✓	✓	✓	✓	✗	✓
Hebron I-13	✓	✓	✓	✓	✓	✓	✗	✓
Hebron L-93-1	✓	✓	✓	✓	✓	✓	✗	✗
Hebron L-93-2	✓	✓	✓	✓	✗	✓	✗	✗
Hebron L-93-3	✓	✓	✓	✓	✗	✓	✗	✗
Hebron L-93-4	✓	✓	✓	✓	✓	✓	✓	✗
Hebron L-93-4Z	✓	✓	✓	✓	✗	✓	✗	✗
Hebron L-93-5	✓	✓	✓	✓	✓	✓	✗	✗
Hebron L-93-6	✓	✓	✓	✓	✓	✓	✗	✗
Hebron L-93-7	✓	✓	✓	✓	✗	✓	✗	✗
Hebron L-93-8	✓	✓	✓	✓	✗	✓	✗	✗
Hebron L-93-9	✓	✓	✓	✓	✗	✓	✗	✗
Hebron L-93-10	✓	✓	✓	✓	✗	✓	✗	✗
Hebron L-93-11	✓	✓	✓	✓	✗	✓	✗	✗
Hebron L-93-12	✓	✓	✓	✓	✗	✓	✗	✗
Hebron L-93-13	✓	✓	✓	✓	✗	✓	✗	✗
Hebron M-04	✓	✓	✓	✓	✓	✓	✓	✗
North Trinity H-71	✓	✓	✓	✗	✓	✓	✗	✗
West Ben Nevis B-75	✓	✓	✓	✓	✓	✓	✗	✓
West Bonne Bay C-23	✓	✓	✓	✓	✓	✓	✓	✗
West Bonne Bay F-12	✓	✓	✓	✓	✓	✓	✗	✗
West Bonne Bay F-12Z	✓	✓	✓	✓	✓	✓	✗	✗

Table 1.2: Table showing the wells and some of their important corresponding logs available for this study.

Chapter 2

Geologic Overview

Offshore Newfoundland (Figure 2.1) formed during the break-up of the supercontinent Pangaea. This break-up occurred through 3 major global rifting events: the initial Late Triassic Tethys rift, the Iberia-northern Europe rift, and the final Labrador Sea rift in the Late Cretaceous (Enachescu, 1987).

The first rifting phase occurred when Pangaea began breaking-up between Nova Scotia and Africa and was orientated NW - SE (Enachescu, 1987). This phase of rifting eventually led to separation and seafloor spreading between Nova Scotia and Africa during the Early Jurassic (DeSilva, 1999). The first phase of rifting is also associated with the formation of rift basins across the Grand Banks-Iberia platform such as the Jeanne d'Arc, Whale, Carson, and Flemish Pass basins on the Newfoundland margin and the Lusitanian, possibly the Porto, and the Galicia Interior basins on the Iberian margin (Figure 2.1) (Sinclair et al., 1994; Tucholke & Sibuet, 2007). These basins formed without significant thinning of the continental crust (Srivastava et al., 1988; Tucholke & Sibuet, 2007).

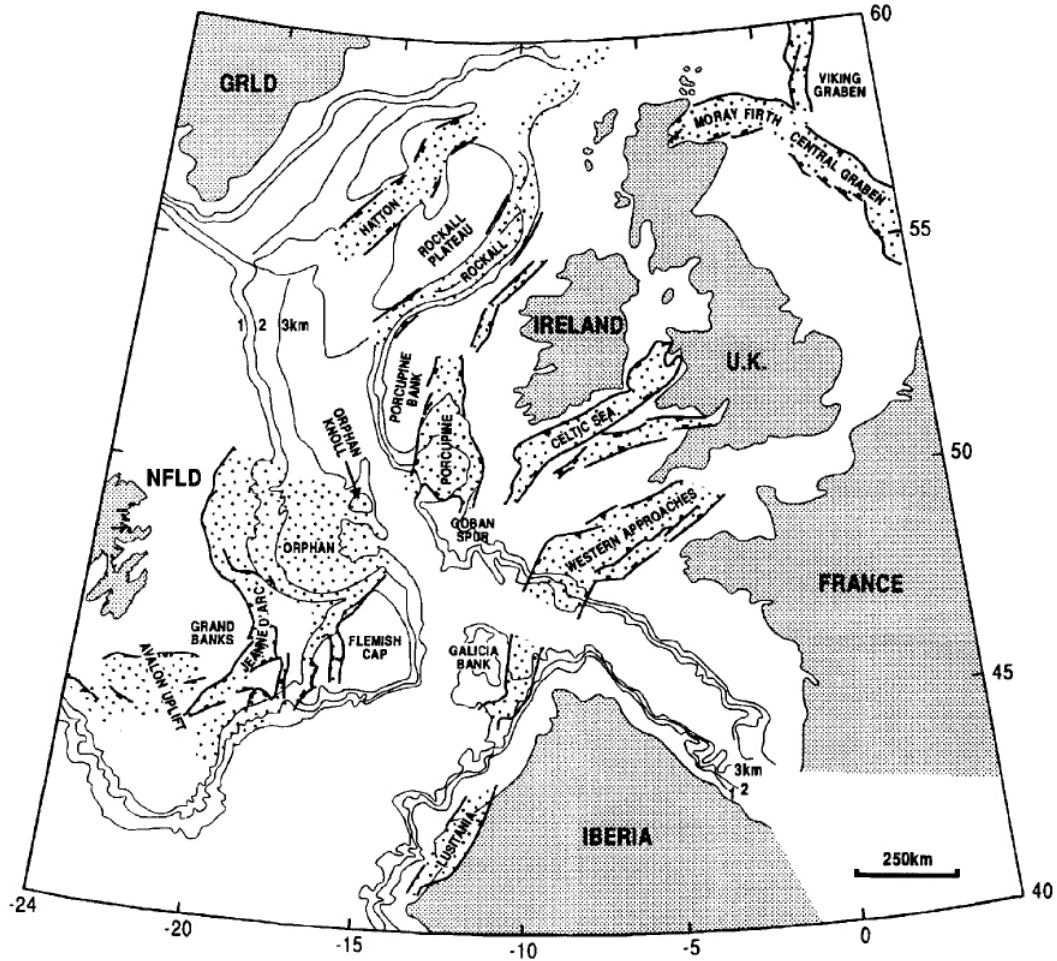


Figure 2.1: A reconstruction of the continental plates at the Late Jurassic time. Marked in stipple pattern are the locations of Mesozoic rift basins. Note that not all the Mesozoic rift basins located in this area are shown. (from Sinclair et al., 1994, with the permission of John Wiley and Sons License Number: 5239341110752)

The second phase of rifting was oriented approximately W - E and it occurred in the Late Jurassic to Early Cretaceous. This phase of rifting led to continental break-up between Newfoundland and Iberia. As this spreading moved northward, a triple junction formed between the Flemish Cap, the Galicia Bank, and the Bay of Biscay spreading center (McIlroy, 2014; Srivastava et al., 1988).

The final rifting phase took place during the Aptian - Albian to Late Cretaceous with an orientation of NE - SW (Tucholke & Sibuet, 2007; Welford et al., 2012). This

rifting event began at this Bay of Biscay triple junction, separating the NE portion of the Flemish Cap from the Goban Spur, and eventually leading to seafloor spreading between Labrador and Greenland (Welford et al., 2012; Dickie et al., 2011; McIlroy, 2014).

2.1 The Jeanne d’Arc Basin

The Jeanne d’Arc Basin (Figure 2.2) is a 10,000 km² extensional Mesozoic rift basin located within the Grand Banks, offshore Newfoundland (Tankard et al., 1989). This basin was formed during the three rifting phases discussed above, and contains extensional features related to the tectonic rifting events and post-Paleozoic sedimentary fill. The Jeanne d’Arc Basin is the primary basin for petroleum exploration offshore Newfoundland, and it currently hosts the four producing fields in operation offshore Newfoundland.

2.1.1 Structure of the Jeanne d’Arc Basin

The overall structure of the Jeanne d’Arc Basin is related to the reactivation of inherited planes of weakness within the underlying Avalon terrane during the three rifting phases that occurred during the break-up of Pangaea (Tankard et al., 1989). Most structural analysis of the Jeanne d’Arc Basin has occurred through seismic studies at the regional, basin, and field scales. These numerous seismic studies have provided a general understanding of the effects of the tectonic break-up of Pangaea on the basin as a whole. Figure 2.3 shows the major bounding faults of the Jeanne d’Arc Basin (Murre, Mercury, and Voyager). The basin is a half-graben, resulting from extension along the listric basin bounding faults; the Jeanne d’Arc Basin is bounded to the south by the Avalon Uplift, the east by the Voyager fault/Central

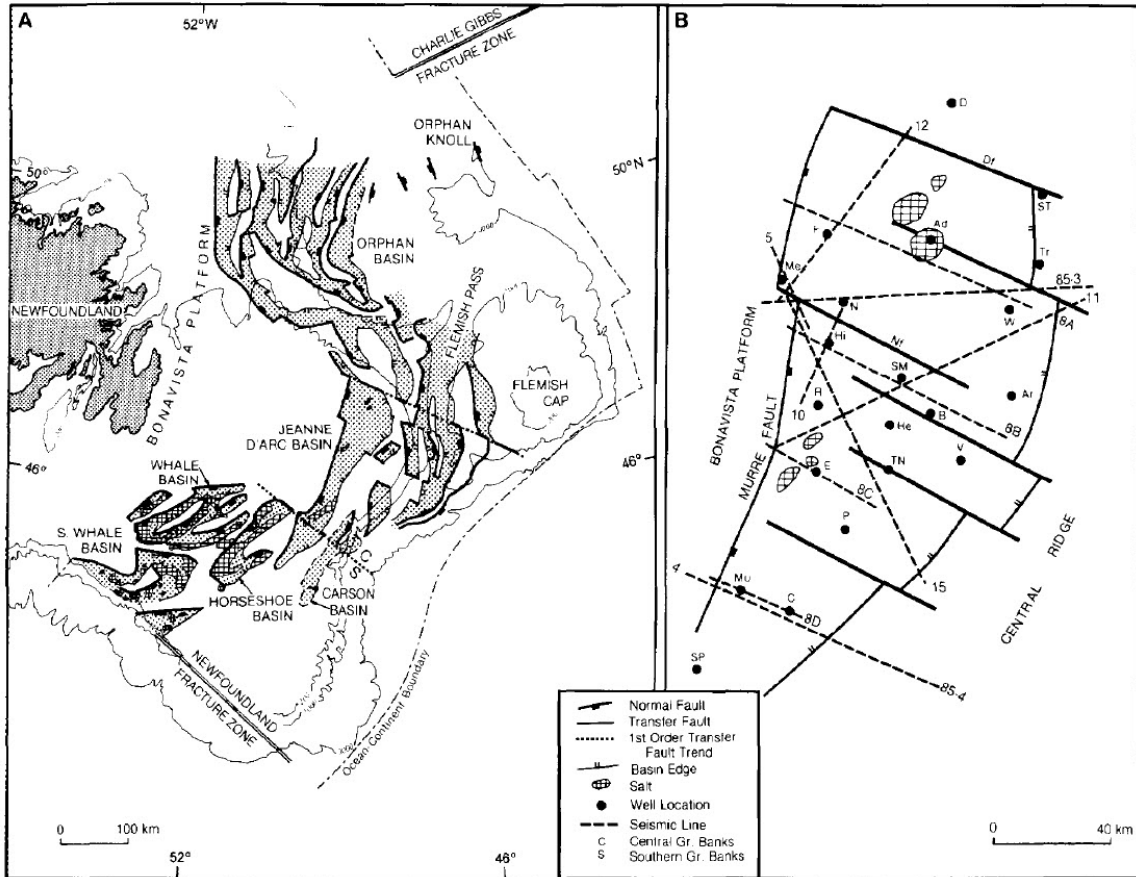


Figure 2.2: a) Map showing the sedimentary basins and structure of the Grand Banks; b) map of the Jeanne d'Arc Basin showing structural features of the basin. (from Tankard et al., 1989 AAPG©1997, reprinted by the permission of the AAPG whose permission is required for further use.)

Ridge, and the west by the Murre and Mercury faults/Bonavista Platform (Tankard et al., 1989; ExxonMobil, 2011). Throughout the basin, many minor faults related to rifting are observed (Figure 2.3) and each fault's orientation and depth are related to their original causative rifting event. Due to the multiple rifting events, reactivation of older faults during subsequent rifting created complex fault patterns within the basin.

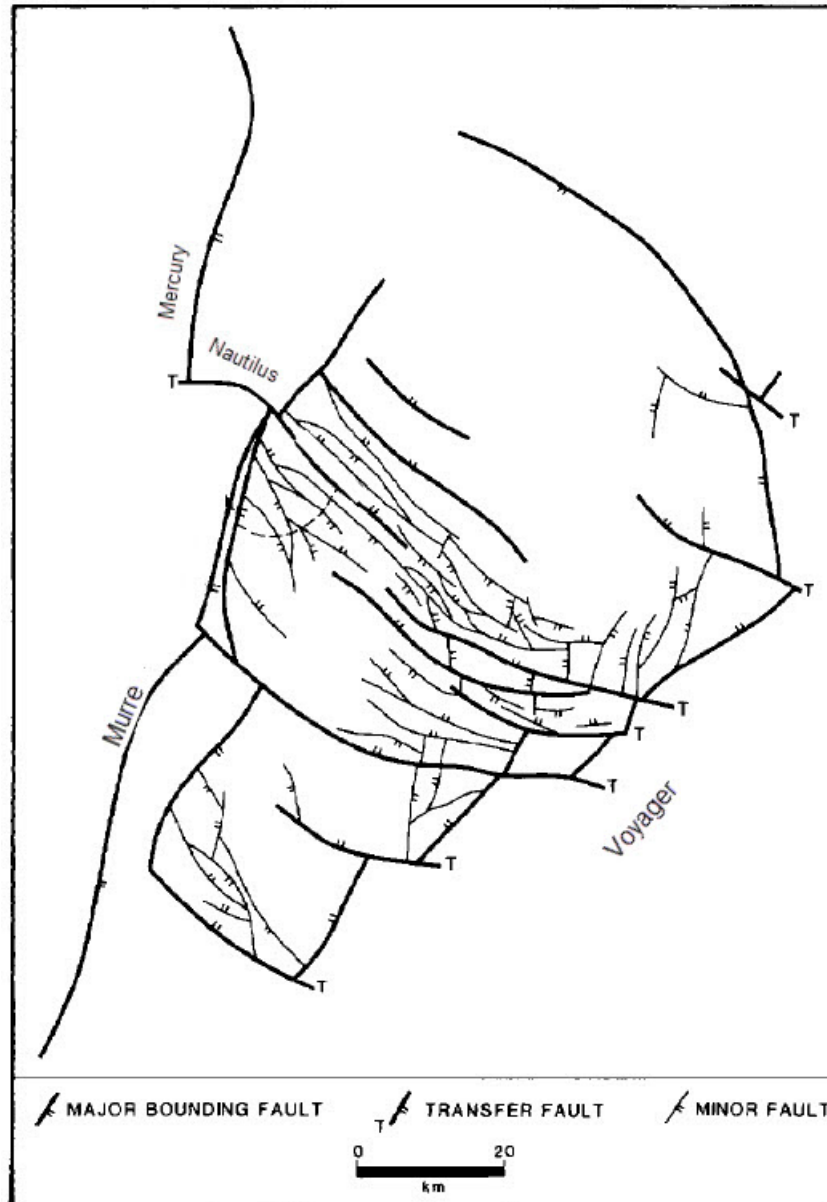


Figure 2.3: Structural framework map of the Jeanne d'Arc Basin indicating major faults mapped within the basin. (from Tankard et al., 1989 AAPG©1997, reprinted by the permission of the AAPG whose permission is required for further use.)

2.1.2 Lithostratigraphy of the Jeanne d'Arc Basin

The Jeanne d'Arc Basin contains 17 km of post-Paleozoic sediment fill. This sedimentary fill is related to the formation of the basin through the rifting stages. The

basement consists of the Avalon terrane from the Appalachian Orogeny, which is composed of Precambrian to Early Paleozoic metasedimentary and crystalline rocks (Tankard et al., 1989; Miller & Singh, 1995). During the Late Triassic to Early Jurassic rifting phase, continental red beds (Eurydice Formation; Figure 2.4), marine evaporites (Argo Formations; Figure 2.4), and carbonates (Iroquois Formation; Figure 2.4) were deposited within the basin (McAlpine, 1990). During the Early Jurassic to the Late Jurassic, an epeiric basin formed, allowing for the deposition of marine shales (Downing Formation, Voyager Formation, and the Rankin Formation; Figure 2.4) and carbonates (Whale Member) (McAlpine, 1990). During the second rift phase, from the Late Jurassic to Early Cretaceous, deltaic and estuarine clastics (Jeanne d'Arc Formation, Fortune Bay Formation, Hibernia Formation, Catalina Formation, and the Eastern Shoals Formation; Figure 2.4) were deposited (McAlpine, 1990). During the Aptian - Albian to Late Cretaceous, the third rifting phase resulted in the deposition of shallow to deep estuarine sandstones (Ben Nevis Formation; Figure 2.4) and shales (Nautilus Formation; Figure 2.4) (McAlpine, 1990). During the post rift, from the Late Cretaceous to the Tertiary, marine shales (Dawson Canyon Formation and the Banquereau Formation; Figure 2.4) were deposited (McAlpine, 1990).

2.1.3 Petroleum System of the Jeanne d'Arc Basin

A successful petroleum system requires certain key elements to be present within the system; these include a hydrocarbon source, migration pathways, accumulation of hydrocarbons, reservoir, seal, and trap. Within the Jeanne d'Arc Basin and other worldwide sedimentary basins with hydrocarbon potential, the source rock is a Kimmeridgian shale (Fowler & McAlpine, 1995). Within the Jeanne d'Arc Basin, this shale is called the Egret member and is part of the Rankin Formation. Analysis of the Egret member reveals total organic carbon (TOC) measurements up to 8%, with

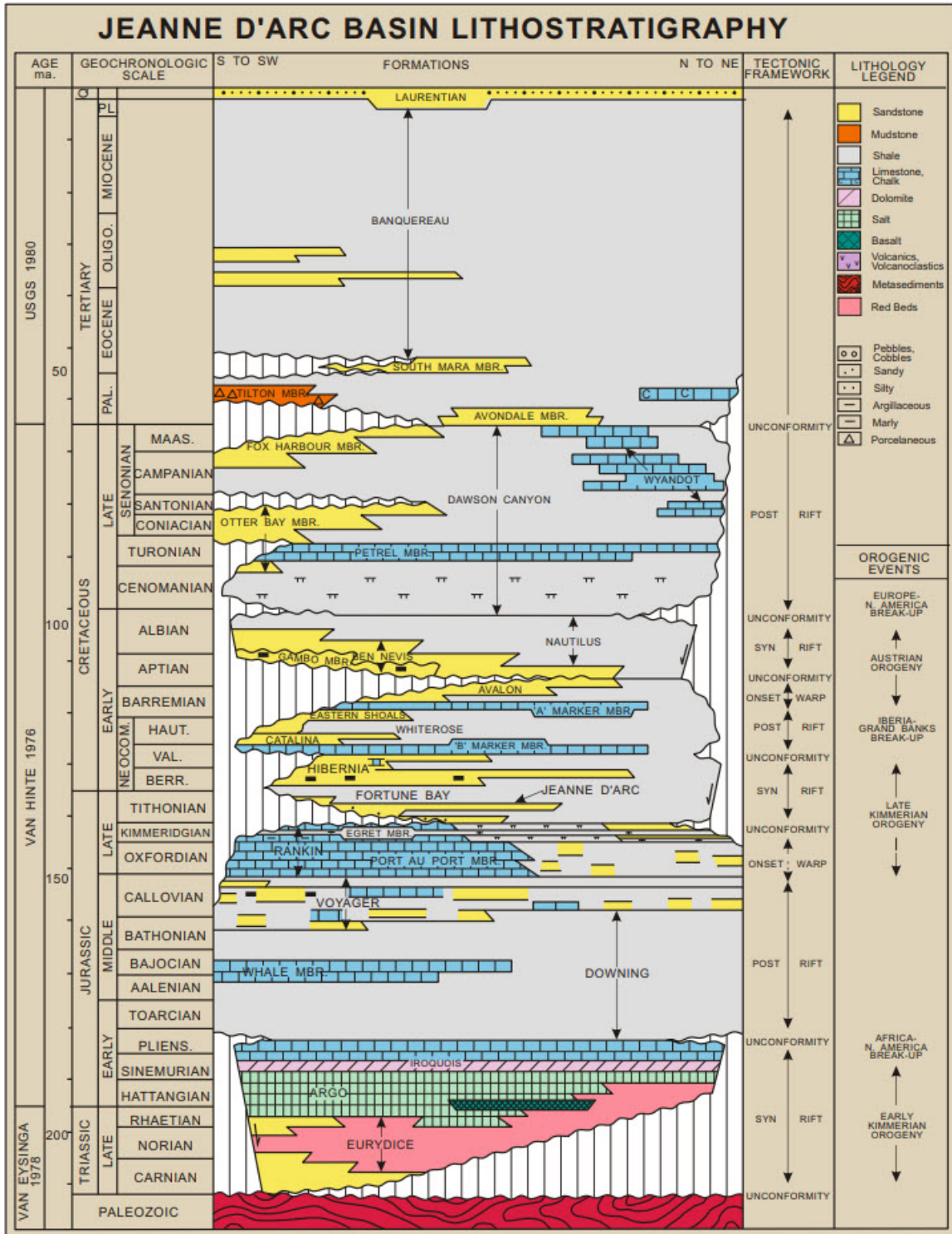


Figure 2.4: Jeanne d'Arc Basin lithostratigraphy chart. (from <https://www.cnlopb.ca>)

an average TOC value between 2 - 5% (DeSilva, 1999). Further studies of the Egret member have shown that it contains type I and II kerogen and indicate that oil generation started approximately 100 Ma and peaked during the Tertiary (\sim 50 Ma) (McAlpine, 1990; Magoon et al., 2005; DeSilva, 1999; Sinclair, 1992).

All oil seen within the Jeanne d'Arc Basin is thought to have come from the Egret member, despite differing degrees of maturity of oil seen throughout the basin, even within the same well (Sinclair, 1992). Due to this varying degree of maturity, the migration of hydrocarbons within the Jeanne d'Arc Basin is thought to be from periodic seepage along faults within the basin (Sinclair, 1992). Within the basin, there are four main reservoir rocks: (1) Jeanne d'Arc Formation, (2) Hibernia Formation, (3) Avalon Formation, and (4) Ben Nevis Formation. These reservoir rocks contain differing properties throughout the basin and will be discussed specifically for the Hebron field in subsequent sections.

The trapping mechanisms within the Jeanne d'Arc Basin are mostly structural, but there are also some stratigraphic and salt traps present. Since the basin experienced many rift phases, the overall structure of the basin is complex, creating many grabens, half-grabens, and horst blocks to collect hydrocarbons (DeSilva, 1999). Towards the northern Jeanne d'Arc Basin, salt becomes more prevalent (Adolphus and Conquest salts), leading to salt-based traps. For the aforementioned reservoirs there is an accompanying seal rock: (1) Fortune Bay Formation, (2) Whiterose Formation, and (3-4) Nautilus Formation (seal for both Avalon and Ben Nevis).

2.2 Hebron Field Overview

The Hebron field is located within the Jeanne d'Arc Basin, approximately 350 km SE of St. John's (Figure 2.5), with an estimated 700 million barrels of recoverable oil (ExxonMobil, 2011; Cornaglia & McNeill, 2018). The field discovery occurred in 1980 with the Ben Nevis I-45 well (Figure 2.6), where the well encountered multiple oil shows within several reservoir intervals (Figure 2.7) (Cornaglia & McNeill, 2018). Over the next 19 years, 5 more delineation wells were drilled: Hebron I-13, West Ben Nevis B-75, Hebron D-94, Ben Nevis L-55, and Hebron M-04 (Cornaglia & McNeill, 2018). These wells targeted surrounding fault blocks (Figure 2.6) and encountered oil shows at multiple reservoir intervals (Figure 2.7) (Cornaglia & McNeill, 2018).

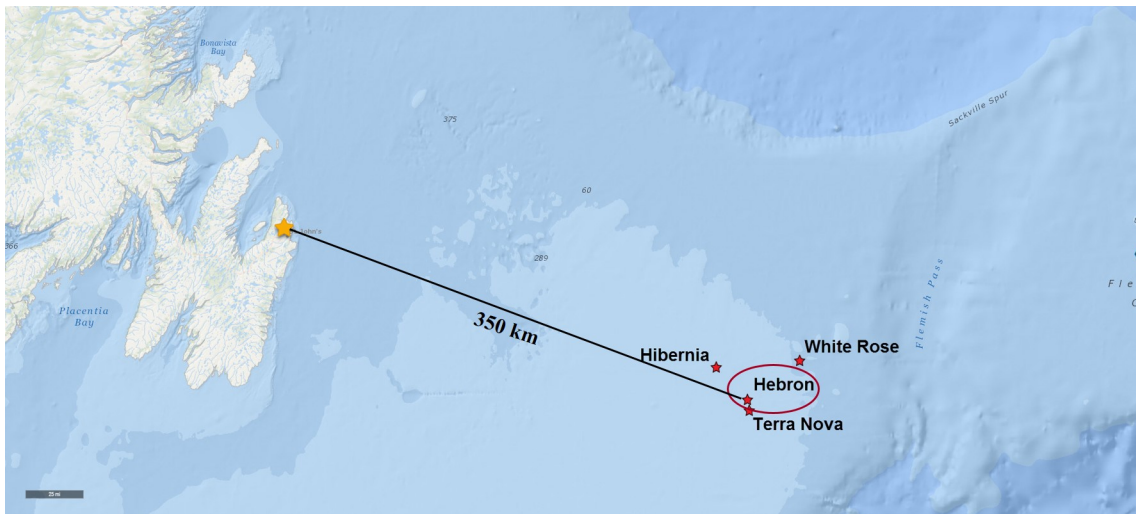


Figure 2.5: Location of the Hebron field with respect to St. John's.

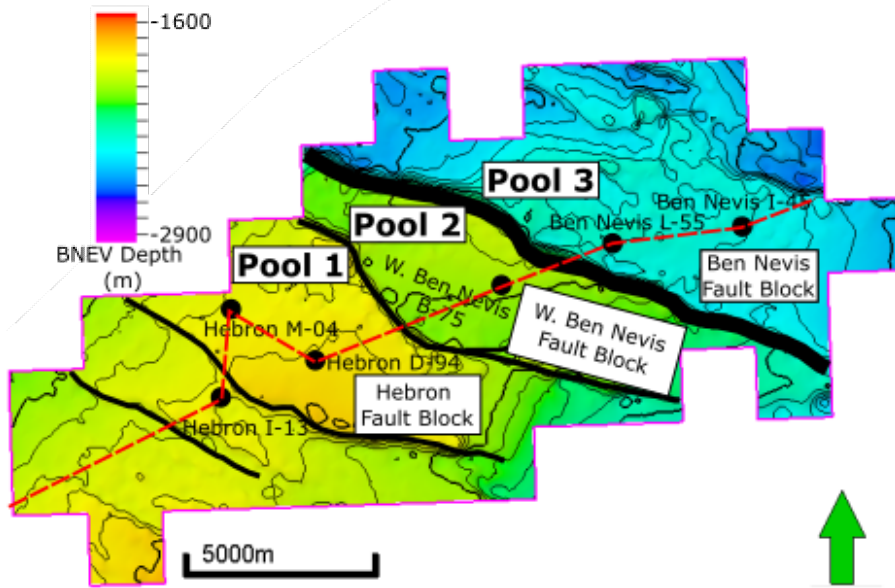


Figure 2.6: Hebron Field map highlighting the position of Figure 2.7. The black lines represent bounding faults for the three main fault blocks in the field. The green arrow points northward. (after Cornaglia & McNeill, 2018)

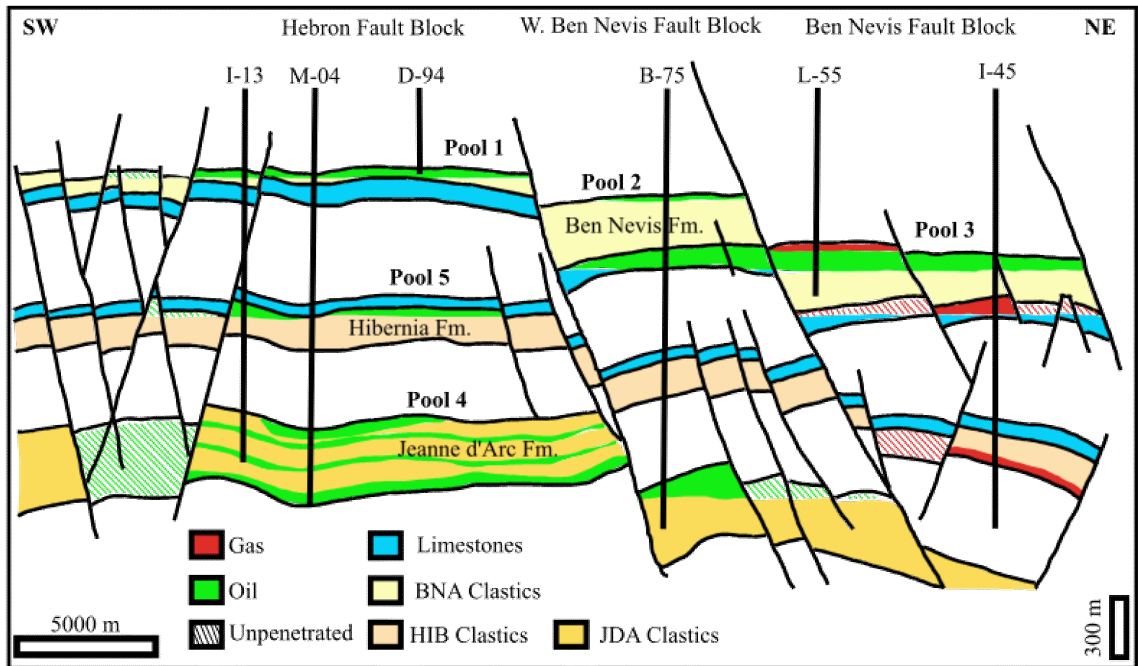


Figure 2.7: Schematic cross-section showing the structure of the Hebron field. (after Cornaglia & McNeill, 2018)

From the initial delineation wells, there was a general understanding of the field structure with hydrocarbon shows seen across three fault blocks (Hebron, West Ben Nevis, and Ben Nevis fault blocks) contained in three different reservoir intervals (Jeanne d’Arc, Hibernia, Ben Nevis - Avalon) (Figure 2.6 and Figure 2.7) (ExxonMobil, 2011; Cornaglia & McNeill, 2018). These discoveries were labeled as pools, in a clockwise manner (Figure 2.7), with the initial field development focused on the Ben Nevis interval within the Hebron fault block (Pool 1).

2.2.1 Structure of the Hebron Field

The Hebron field is atop a horst block with accompanying grabens located to the NE and SW (ExxonMobil, 2011). The field is dissected by two main fault patterns that are directly related to the rifting that has occurred in the area: N-S trending normal faults related to the second rifting phase, and the NW-SE trending normal faults related to the third rifting phase (ExxonMobil, 2011). The first set of faults was active during the deposition of the Jeanne d’Arc and Hibernia reservoir intervals; the second set was active during the deposition of the Ben Nevis reservoir interval (Figure 2.8) (ExxonMobil, 2011). These faults create structural traps for Pools 1-5 (Figure 2.7); these traps were in place before peak oil generation, creating optimal conditions for trapping hydrocarbons (ExxonMobil, 2011).

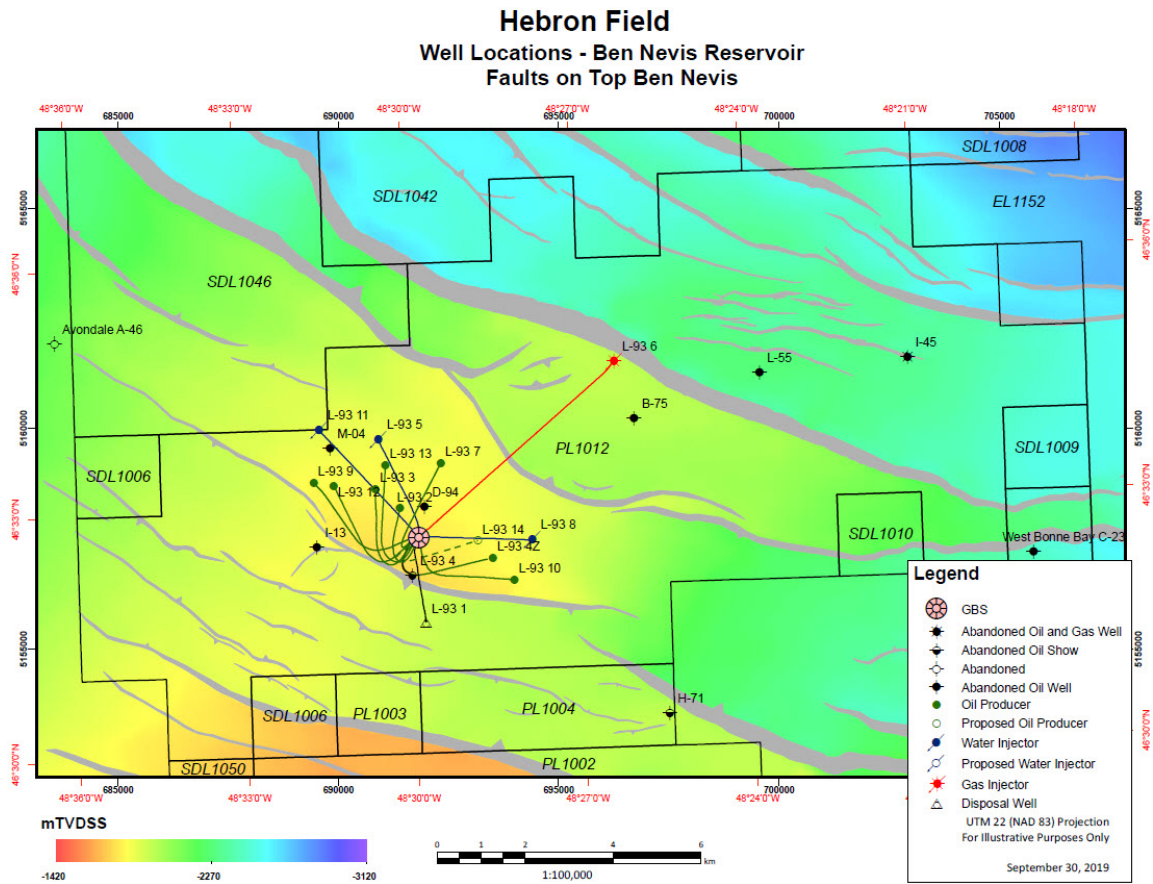


Figure 2.8: Ben Nevis depth structure map for the Hebron field showing the locations of the current development wells. The Ben Nevis surface is displayed in mTVDss which is true vertical depth below mean sea level in meters. (from <https://www.cnlopbc.ca>)

2.2.2 Reservoir Geology of the Hebron Field

The Hebron field has three main reservoir intervals: Ben Nevis - Avalon, Upper Hibernia, and Jeanne d’Arc formations. The focus of this thesis is on the Ben Nevis interval within the Hebron fault block (Pool 1). The Ben Nevis formation was deposited during the Aptian - Albian during the third rifting phase, generating syn-rift growth of sedimentary layers across faults associated with the third rifting phase. Within the Hebron field, the Ben Nevis Formation consists of fine grained sandstone, which fines upward with minor shales present, interpreted to be deposited in a marine shoreface environment (ExxonMobil, 2011). The Avalon sandstone interval in

the Hebron field is grouped with a regional limestone unit, the A marker Member, to form the Avalon Formation for modeling purposes (ExxonMobil, 2011). The Avalon sandstone is a coarsening upward sandstone, interpreted to be a marine shoreface (ExxonMobil, 2011). The Ben Nevis reservoir in the pool of interest of this thesis (Pool 1) is considered fair to good quality with average permeabilities from 50 - 400 mD and average porosity from 10 - 28% (ExxonMobil, 2011; Cornaglia & McNeill, 2018).

Chapter 3

Seismic Data Interpretation

The interpretation of the seismic data in the thesis follows the simple flow chart scheme shown in Figure 3.1. These interpretations are made using the Petrel software for all 111 seismic lines available from the 2013 ExxonMobil 3D Survey shown in Figure 1.3.

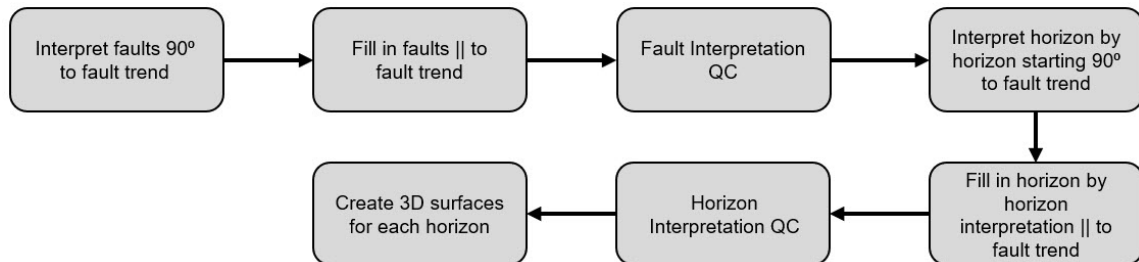


Figure 3.1: Workflow for interpretation of the seismic data set.

3.1 Fault Interpretation

The interpretation of the seismic data begins by interpreting the faults. This is first done by determining the strike orientation for the faults within the Hebron field. Figure 3.2 is a modified version of Figure 2.3, where the circled area is approximately the location of the Hebron field. This modified figure indicates that the general fault

trend is approximately NW - SE. The depth slices from the seismic survey (Figure 3.3) are examined to support this interpretation, identifying discontinuities trending in the same direction in the seismic data. This investigation determined that the inline (IL) seismic lines are perpendicular to the fault trend, thus optimally orientated for imaging the fault structure.

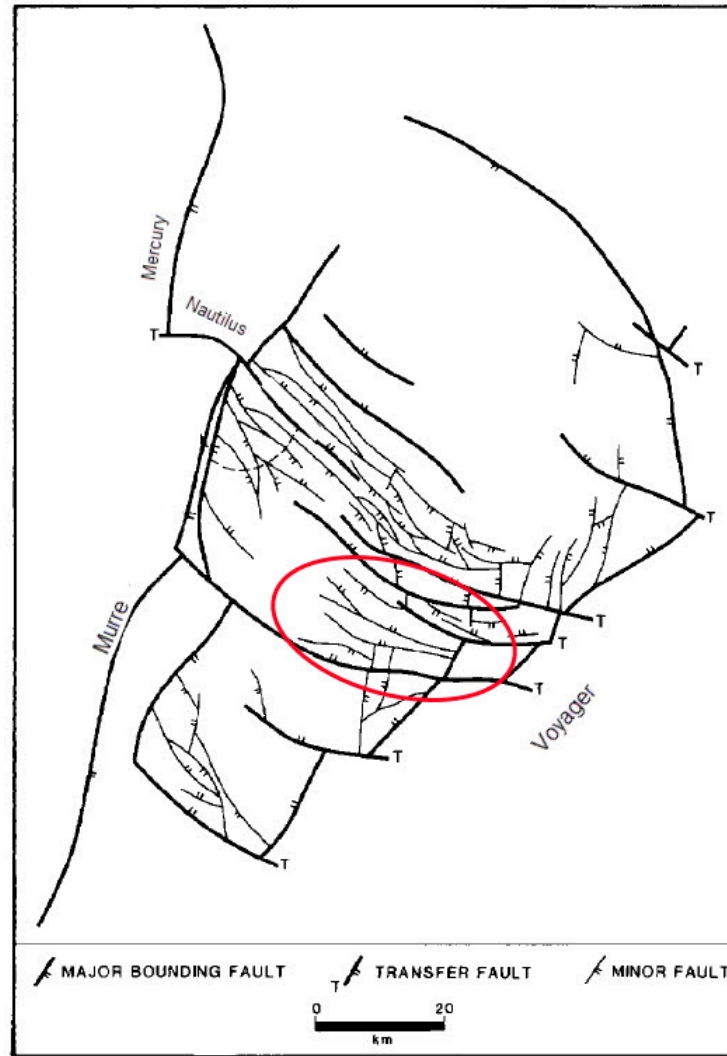


Figure 3.2: Modified version of Figure 2.3, with the location of the Hebron field circled in red. (after Tankard et al., 1989 AAPG©1997, reprinted by the permission of the AAPG whose permission is required for further use.)

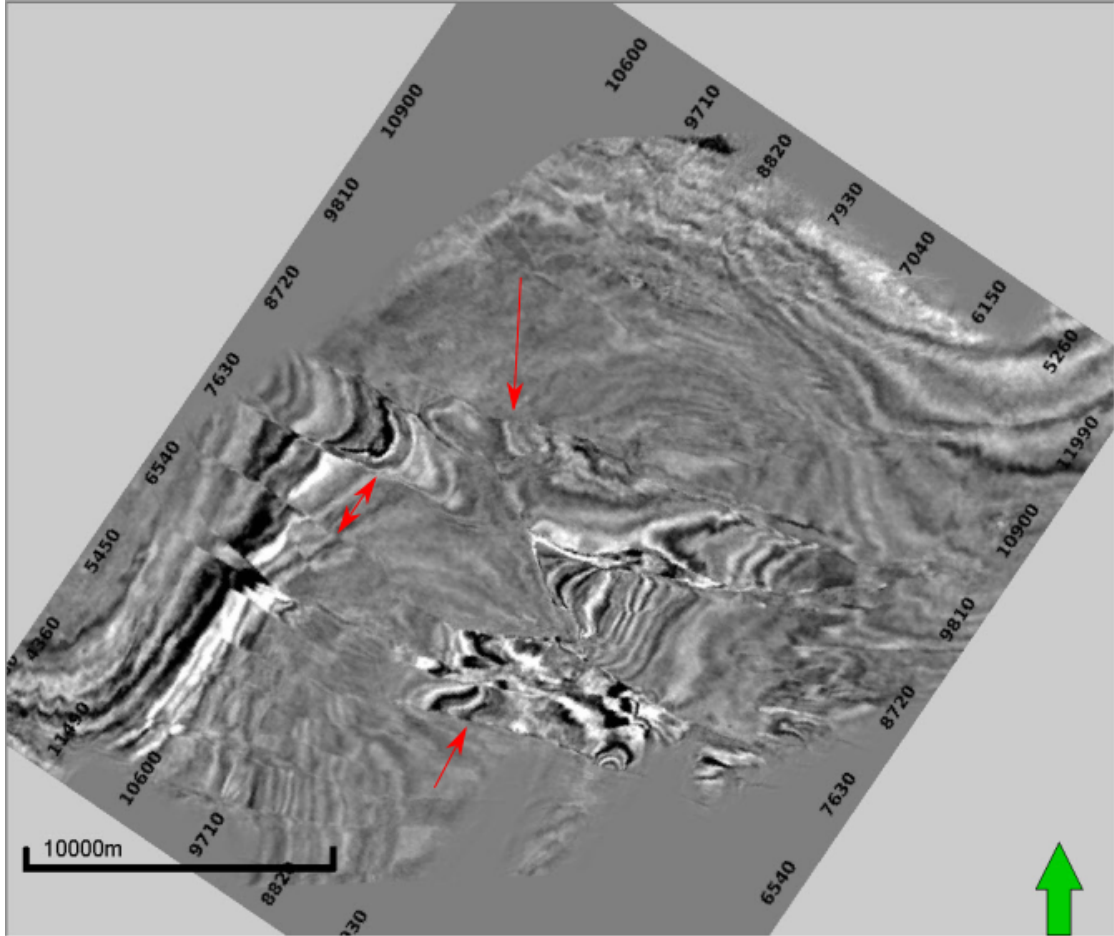
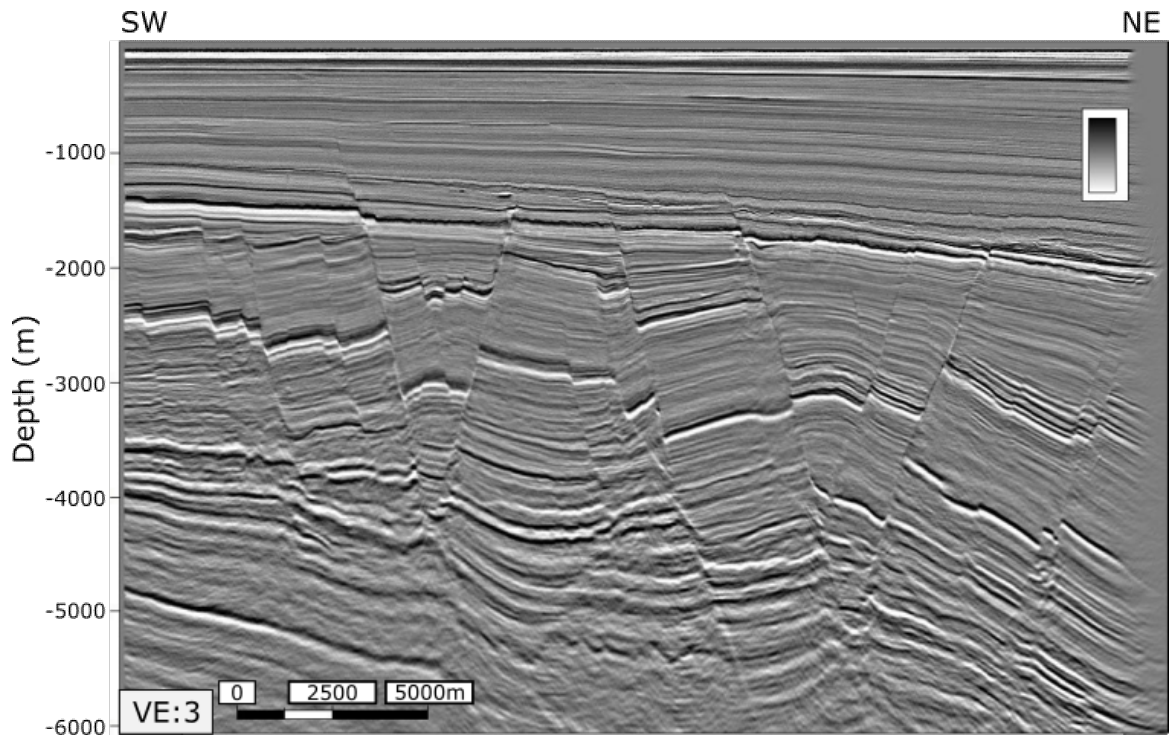
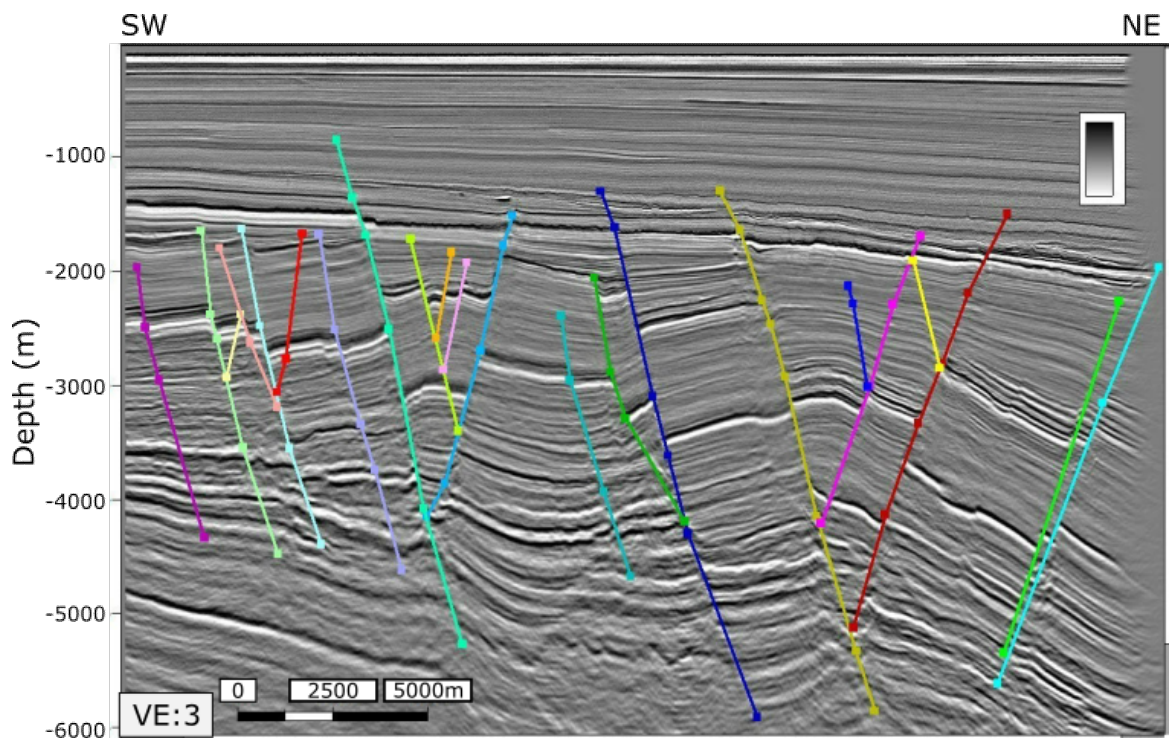


Figure 3.3: Example of a depth slice from the seismic survey at -2200 m depth with shown discontinuities in the seismic data related to the faulting of the subsurface. The red arrows highlight some of the fault induced seismic discontinuities and the green arrow points northward.

Beginning the fault interpretation on the ILs, the faults are picked on grayscale seismic sections to effectively show the fault-induced discontinuities in the seismic data (Figure 3.4). N-S striking faults (i.e. out of plane or parallel to the ILs) are left uninterpreted on the ILs as they are better imaged on the cross-line seismic lines (XL). After interpreting the faults on all of the ILs, the faults on all of the XLs are interpreted in the same manner, leaving the out-of-plane faults uninterpreted and only interpreting the faults striking approximately N - S.



(a)



(b)

Figure 3.4: IL 8481 a) uninterpreted seismic section b) fault interpreted seismic section.

3.1.1 Quality Control of Fault Interpretations

Quality Control (QC) of the fault interpretations is completed to ensure the consistency of the interpretations throughout the field. There are two main methods of QCing the fault interpretations, (1) overlaying the faults on top of depth slices (2) analyzing the faults in a 3D view.

Projecting fault interpretations on to depth slices allows the interpreter to compare discontinuities within the seismic data to fault interpretations; this method is similar to QCing fault interpretations with a coherence (variance) attribute computed on a 3D seismic volume. Looking at Figure 3.5, we see that by comparing fault interpretations from individual 2D seismic lines with depth slice discontinuities, the fault planes and structure of the field can be compared in a 3D view.

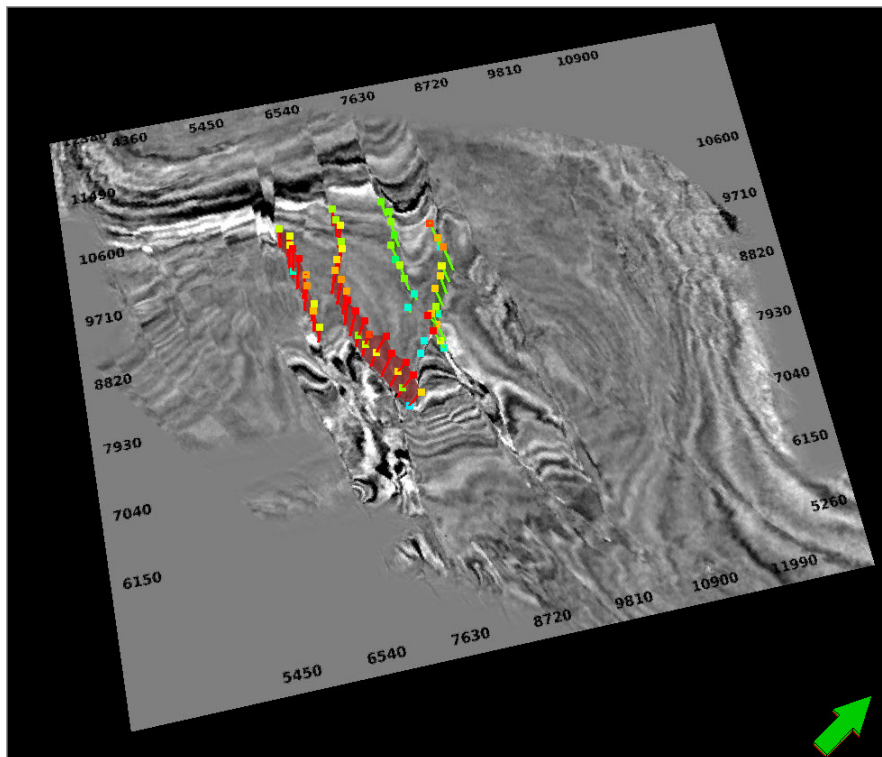


Figure 3.5: Comparison of fault interpretations to seismic data in 3D; Depth Slice -2200m (Figure 3.3) with a sample subset of fault interpretations from Pool 1 projected. The green arrow points northward.

The second QCing method (Figure 3.6) is done using a 3D view window within the Petrel software, comparing the interpretation of a given fault on a specific seismic section to adjacent ILs. This allows us to gain a better understanding of how the structure of the field is evolving between each interpreted section.

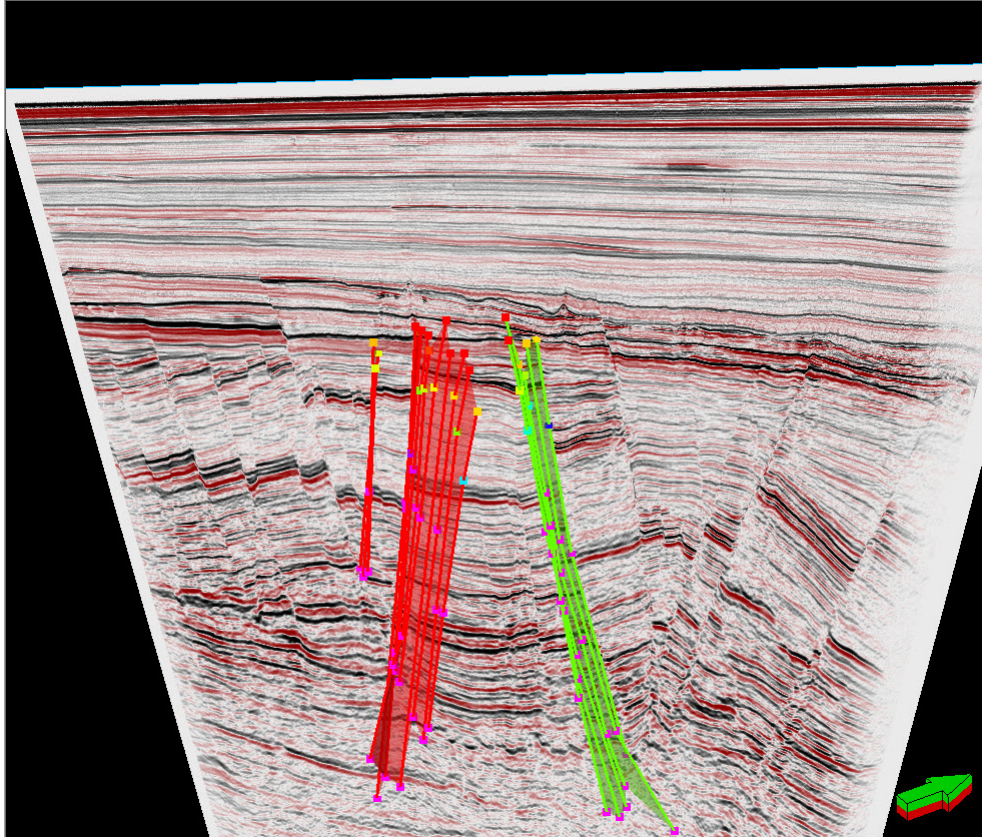


Figure 3.6: 3D view of IL 9121 overlain by interpretations of the faults bounding Pool 1 within the Hebron Field. The green arrow points northward.

3.2 Horizon Interpretation

Following the fault interpretation, multiple seismic events are interpreted across each seismic line following the workflow outlined in Figure 3.7.

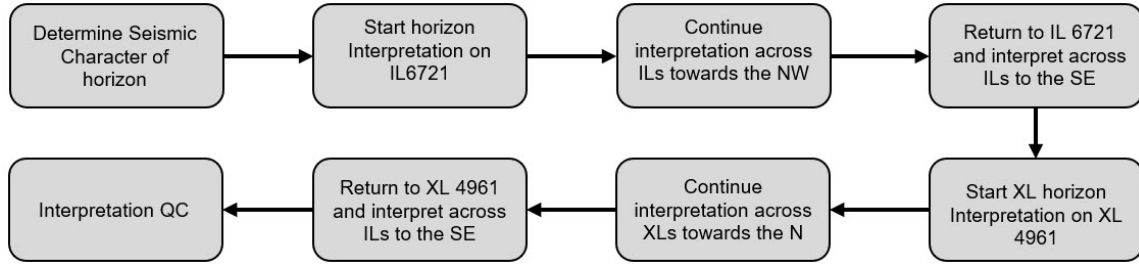


Figure 3.7: Workflow followed for the horizon interpretations.

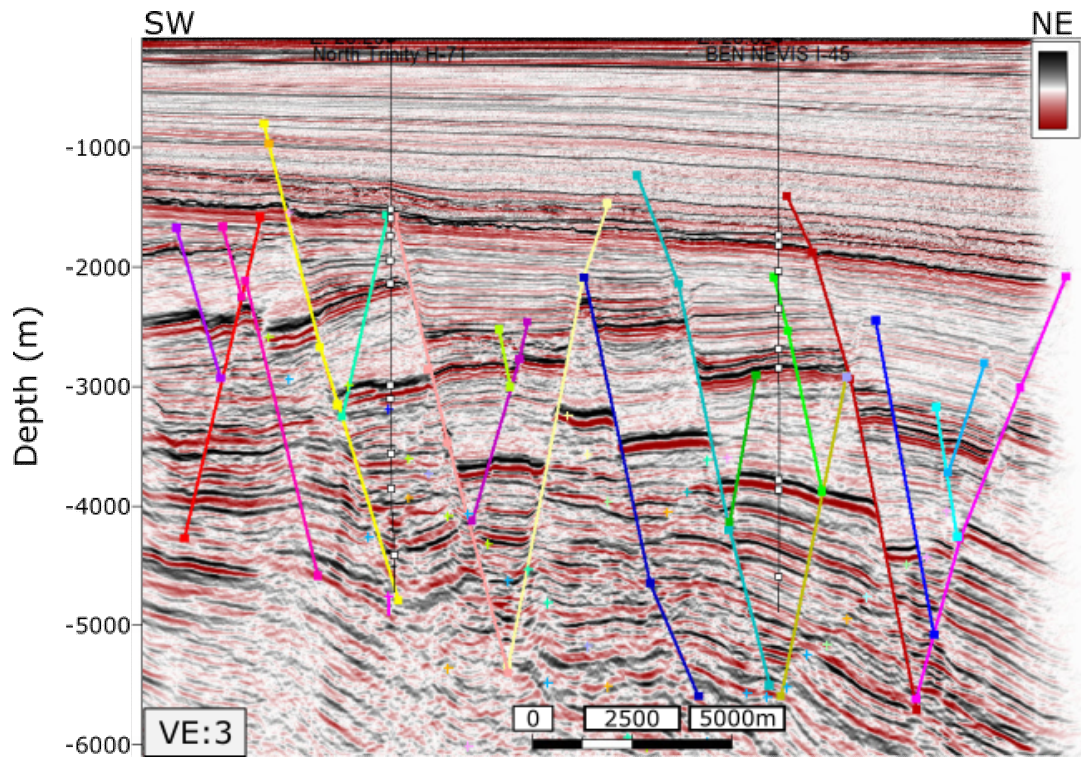
Table 3.1 indicates the seismic events/intervals interpreted across all 111 seismic lines; the color fill represents the horizon’s corresponding color in subsequent seismic sections. We took the seismic character information from the available seismic survey interpretation report (ExxonMobil, 2019) and well top information from the same report combined with additional well top information available through the CNLOPB.

Horizon	Seismic Character
Water Bottom	Peak
Base Tertiary Unc	Peak
Petrel	Peak
Nautilus	Trough
Top Ben Nevis Reservoir	Peak/Trough
Base Ben Nevis Reservoir	Trough
A Marker	Peak
B Marker	Peak
Top Upper Hibernia	Trough
Base Hibernia	Trough
Top Jeanne d’Arc	Peak
Jeanne d’Arc B Sand	Peak

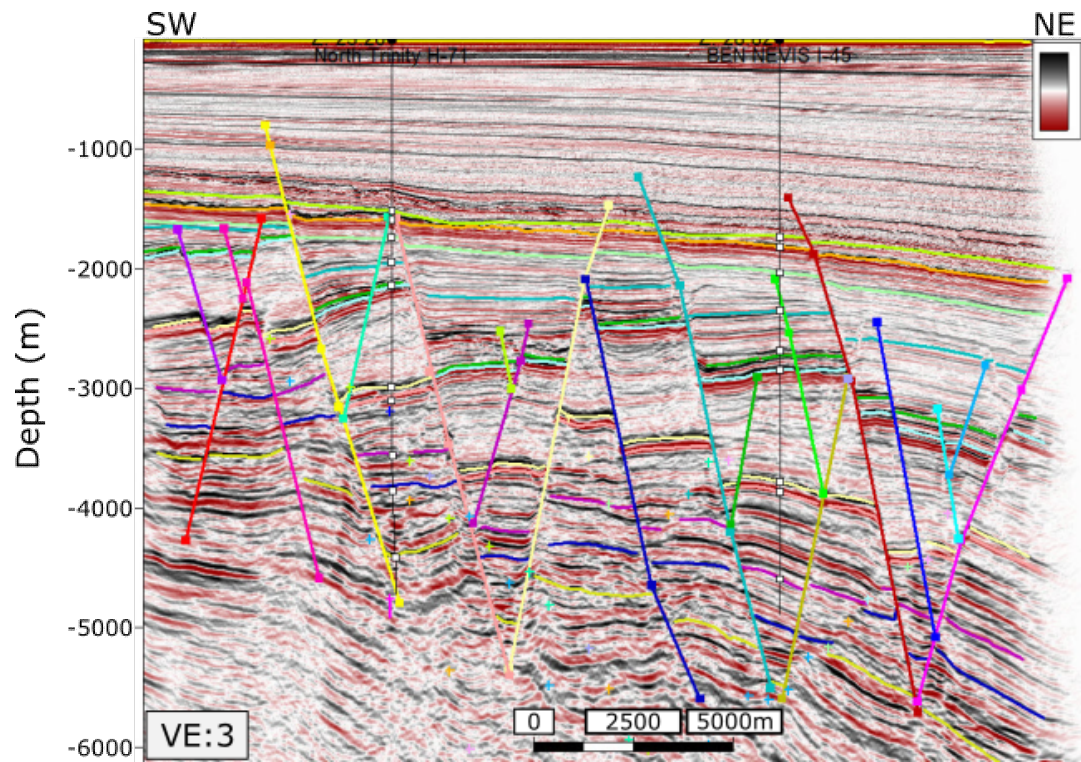
Table 3.1: Table indicating the seismic character that was picked for each horizon. The color fill for each horizon corresponds to the color of the interpretation for that formation.

Interpretation of the seismic horizons is completed on a horizon by horizon basis starting at IL 6721; this seismic line is chosen as the starting point because it is the closest IL to the North Trinity H-71 well. The North Trinity H-71 well intersects all of

the horizons of interest, which are unfaulted and towards the edge of the survey (Figure 3.8). This seismic line is a suitable starting point as it allows the interpretation to be easily continued across the rest of the survey. Upon completing the interpretation of a given seismic horizon across every IL, XL interpretations begin on XL 4961. This XL ties with the Brent's Cove I-30 well, which like North Trinity H-71, intersects all of the horizons of interest and is also located near the edge of the survey (Figure 3.9).



(a)



(b)

Figure 3.8: IL 6721 highlighting the North Trinity H-71 well. a) seismic section with only the fault interpretation b) horizon interpreted seismic section.

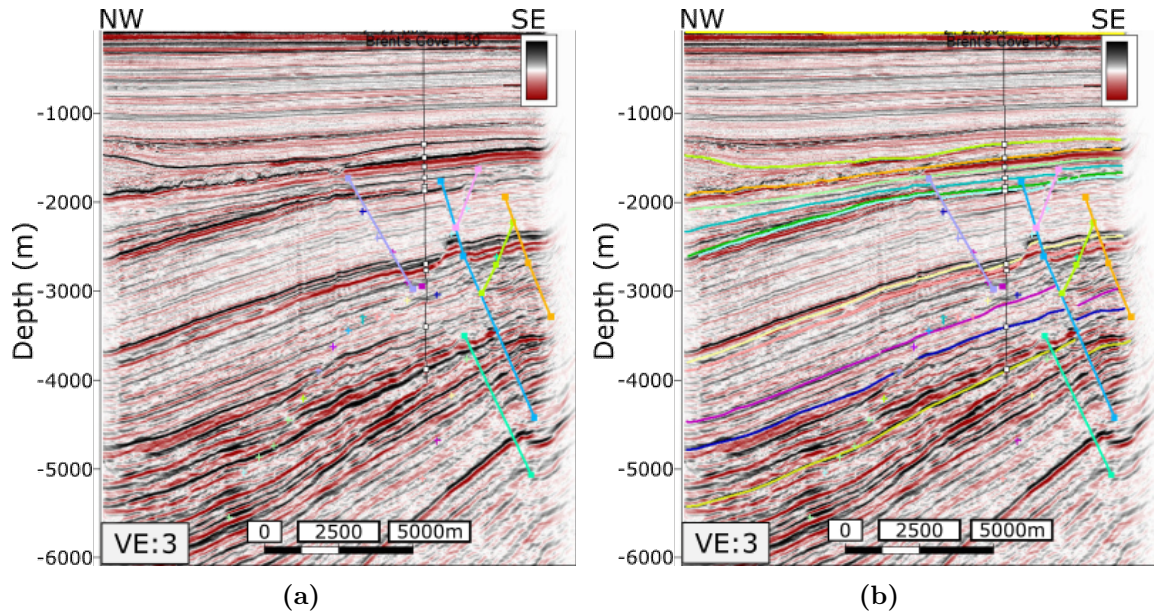
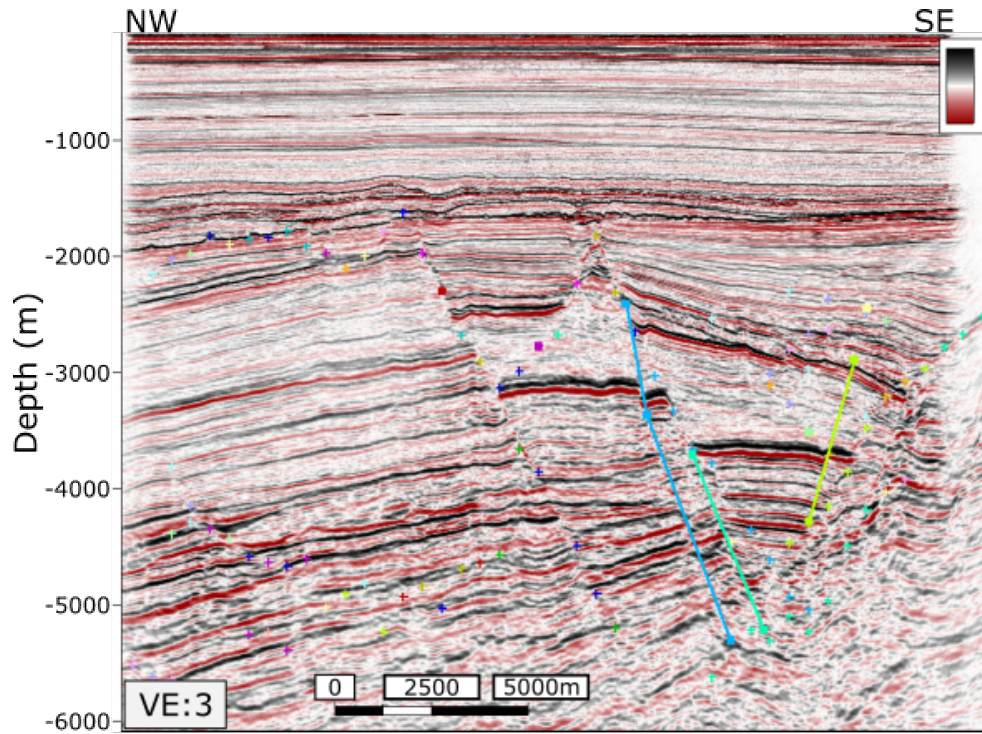


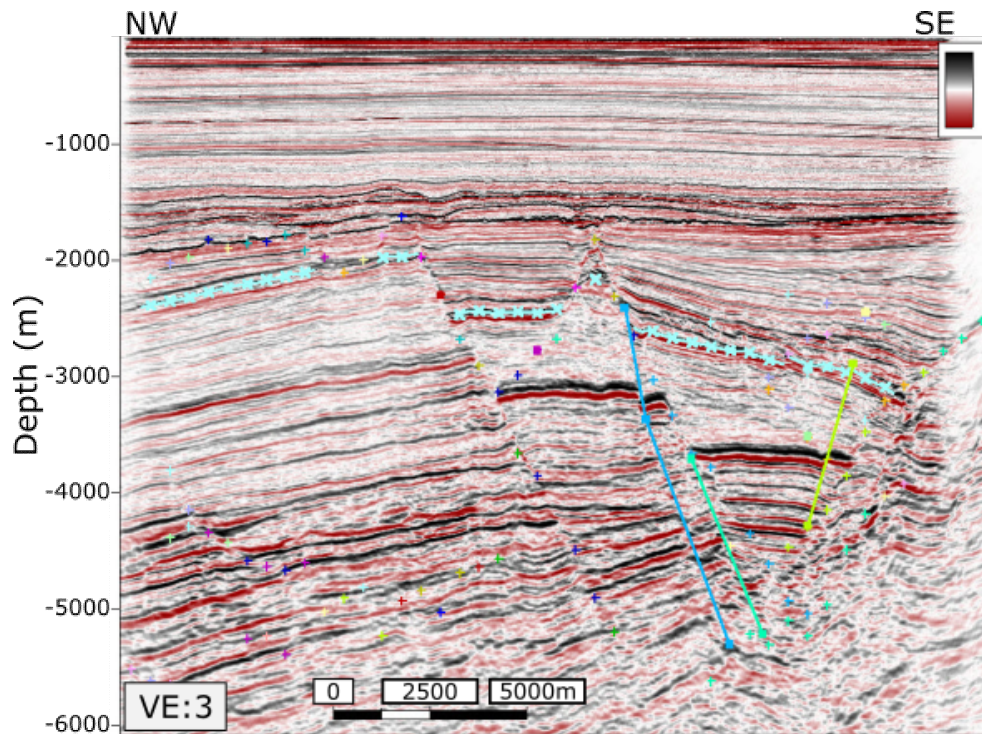
Figure 3.9: XL 4961 highlighting the Brent's Cove I-30 well. a) seismic section with only the fault interpretation b) horizon interpreted seismic section.

3.2.1 Quality Control of Horizon Interpretations

We complete QC of horizon interpretations to ensure that a horizon follows a consistent seismic event across a given data set(s). We use well data and XLs as the main QCing tools for the horizon interpretations. We utilize well log data and well log top information during the interpretation process as a tool to confirm that a horizon/seismic event is consistently representing the same rock type throughout the field/survey. XLs are used during the IL interpretation process to perform a consistency check as it allows the interpreter to compare previous IL horizon interpretations on a single XL seismic section (Figure 3.10).



(a)



(b)

Figure 3.10: XL 8321 highlighting the use of XLs for horizon interpretation QC. a) seismic section with only the fault interpretation b) horizon interpreted seismic section; where the cyan crosses represent the A Marker horizon interpretation completed on IL seismic lines.

3.2.2 Horizon Interpretation Outputs

Once a horizon/seismic event is interpreted throughout the entirety of the seismic survey (Figure 3.11), we use it to generate a 3D surface representing the subsurface structure; Figure 3.12 is an example 3D surface. These surfaces are essential inputs for the upcoming Chapters, with their roles being further discussed within each specific Chapter.

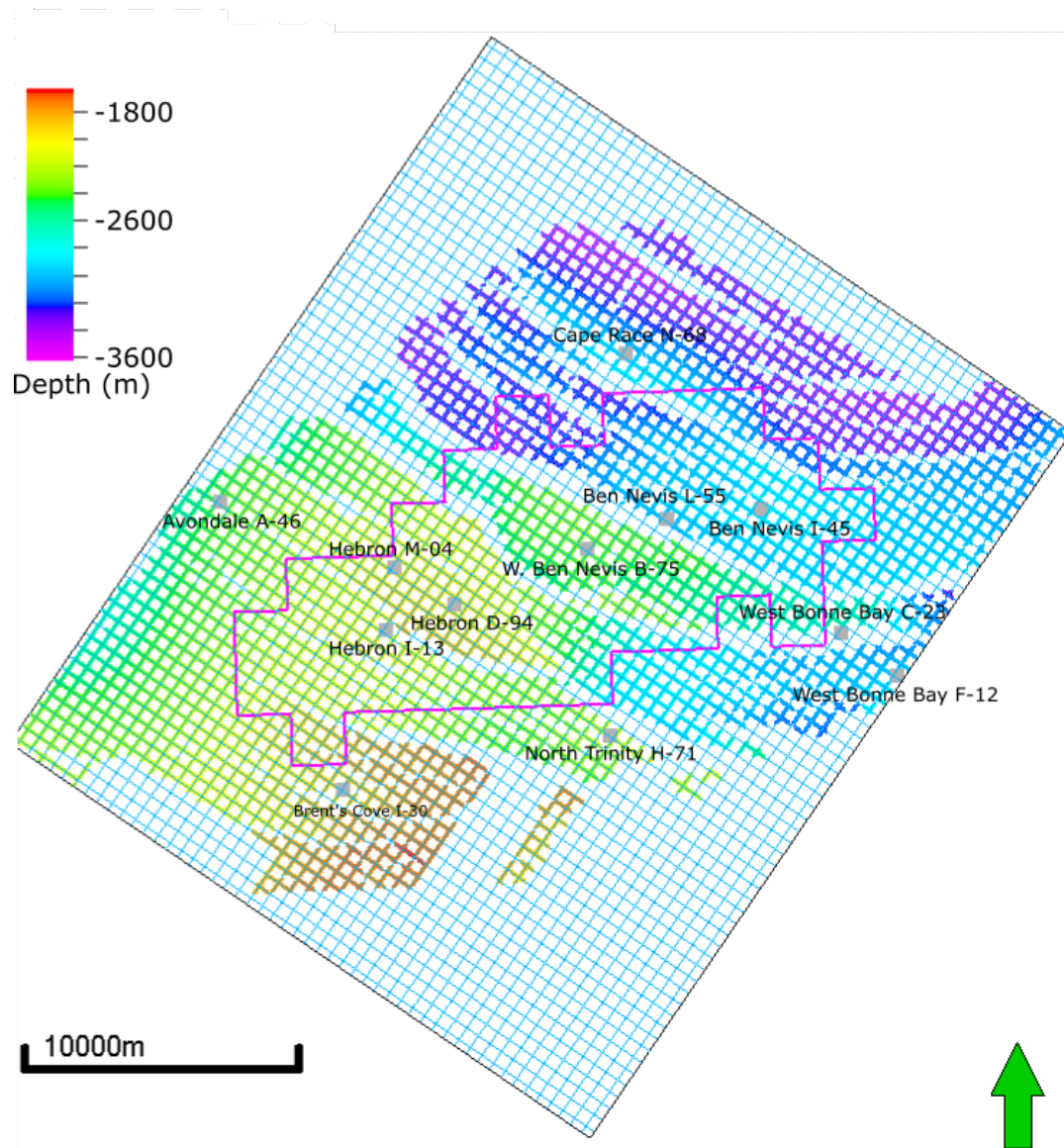


Figure 3.11: Example of a completed horizon interpretation shown in a 2D map view; shown here is the A marker horizon. The green arrow points northward.

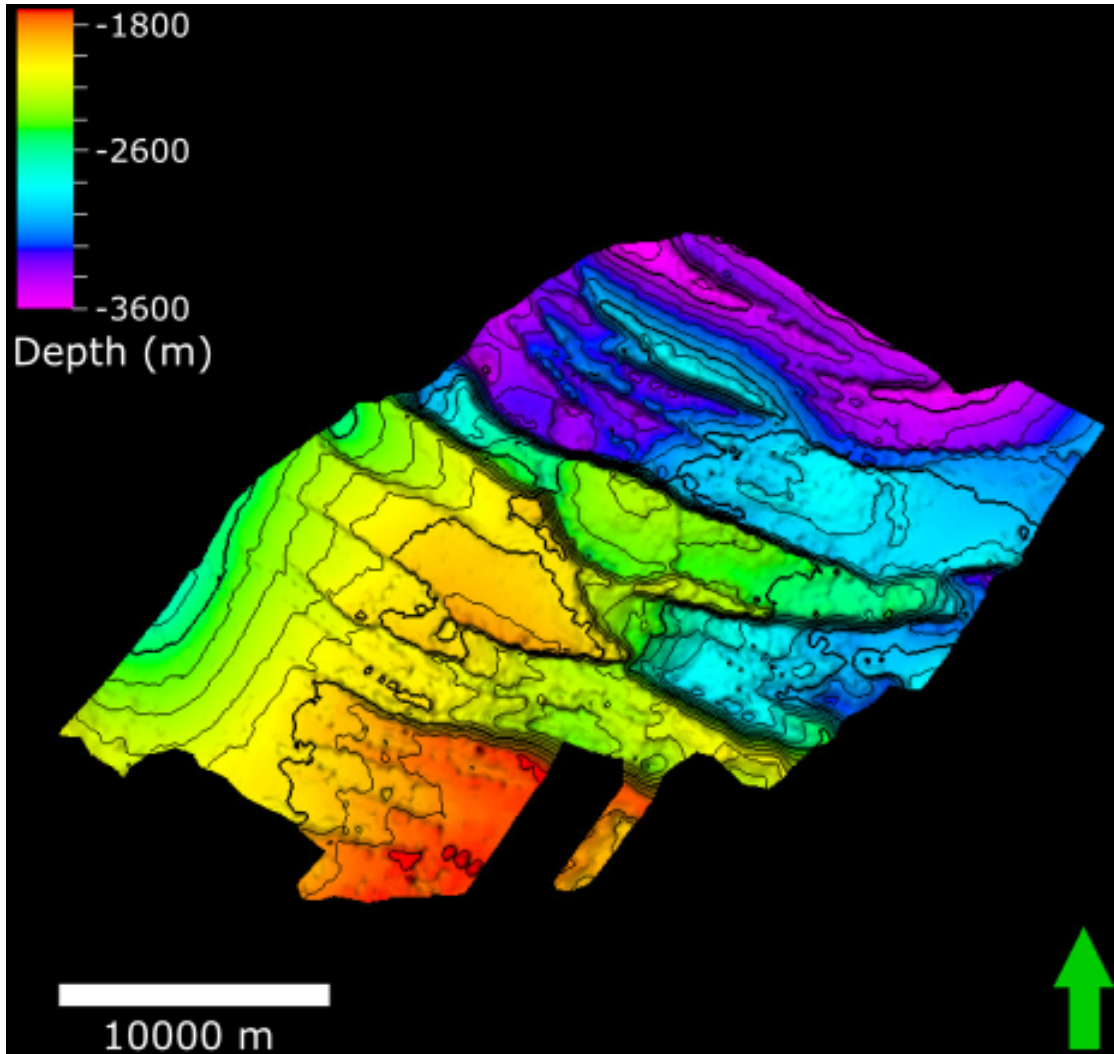


Figure 3.12: An example 3D surface generated from an interpreted seismic horizon throughout the survey area; shown here is the A marker surface generated from the A marker horizon. The green arrow points northward.

Chapter 4

Hebron Field Pool 1 Geological Model

The geological model presented in this thesis is built to represent Pool 1 of the Hebron Field (Figure 2.7), as this is the reservoir of interest for this 4D seismic study. We built the geological model in the Petrel software following the workflow shown in Figure 4.1; this workflow was created with Joel Shank, a geoscientist at ExxonMobil (Shank, 2020).

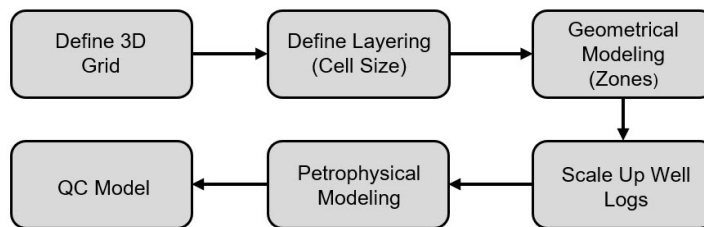


Figure 4.1: Workflow followed to build the geological model of the Pool 1 reservoir within the Hebron Field.

4.1 Pool 1 Geological Model Inputs

The geological model inputs are four 3D surfaces interpolated from the horizon interpretations explained in the previous Chapter (Chapter 3), density and porosity well logs for wells penetrating the Ben Nevis interval within the Pool 1 area, and a boundary polygon for the Pool 1 area.

4.1.1 Pool 1 Geological Model 3D Surfaces

The Pool 1 geological model shown in this thesis utilizes the Nautilus, Top Ben Nevis Reservoir, Base Ben Nevis Reservoir, and A Marker surfaces from the previous Chapter (Table 3.1). These four surfaces cover the main components of the Pool 1 reservoir system, where the Nautilus - Top Ben Nevis Reservoir interval comprises the Nautilus shale (seal rock), the Top Ben Nevis Reservoir - Base Ben Nevis Reservoir interval represents the Ben Nevis (reservoir rock) zone, and the base Ben Nevis Reservoir - A Marker interval consists of the Avalon zone (reservoir rock for Pool 2). In terms of the model, these surfaces define the structure, zones, and depths of the geological model.

4.1.2 Pool 1 Geological Model Well Log Preparation

Pool 1 contains multiple well penetrations (Figure 2.8). When building the geological model, we select the Hebron I-13, Hebron M-04, Hebron D-94 delineation wells, and the Hebron L-93 5 production well as input wells for the model. Hebron L-93 5 is included in the model as it contains a full log suite (density, gamma ray, sonic, and resistivity data) within a vertical section of the well covering the modeled interval within Pool 1; the Hebron L-93 5 logs are digitized using the Didger 5 software.

The well log digitization process is done by taking a screen capture of each well log page, importing the picture into Digger 5, and assigning coordinates to the corners of the log. A polyline is drawn along the well reading (Figure 4.2) and this polyline is then exported to the correct well log LAS format to import into Petrel. Once each log page is digitized, the individual page LAS files are combined into a master LAS file for the well (Figure 4.3); the well log data are then examined in Petrel to ensure data quality (Figure 4.4).

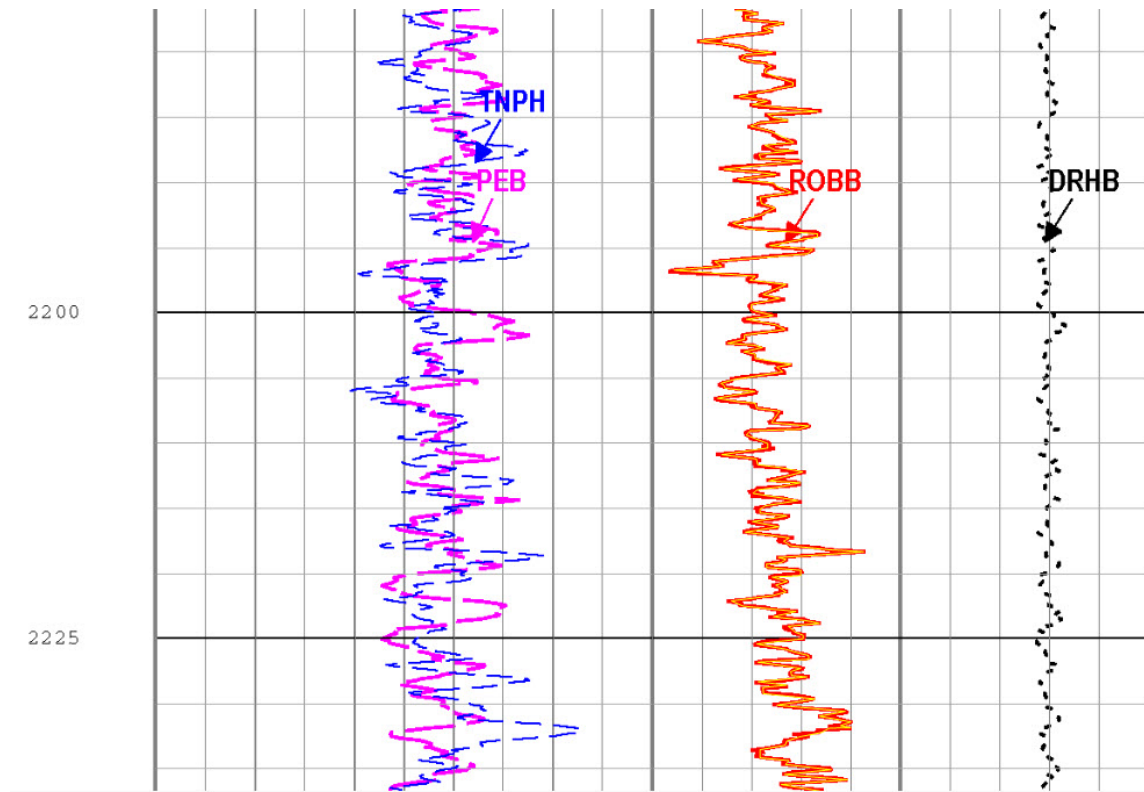


Figure 4.2: Example well log digitization using the Digger 5 software highlighting the log by log; where the red curve is the density (RHOB) log for a section of the Hebron L-93 3 well and the overlain yellow line is the drawn polyline used to extract the digitized log values. This process is completed for each curve one at a time. Hence why only the polyline for the density log is shown.

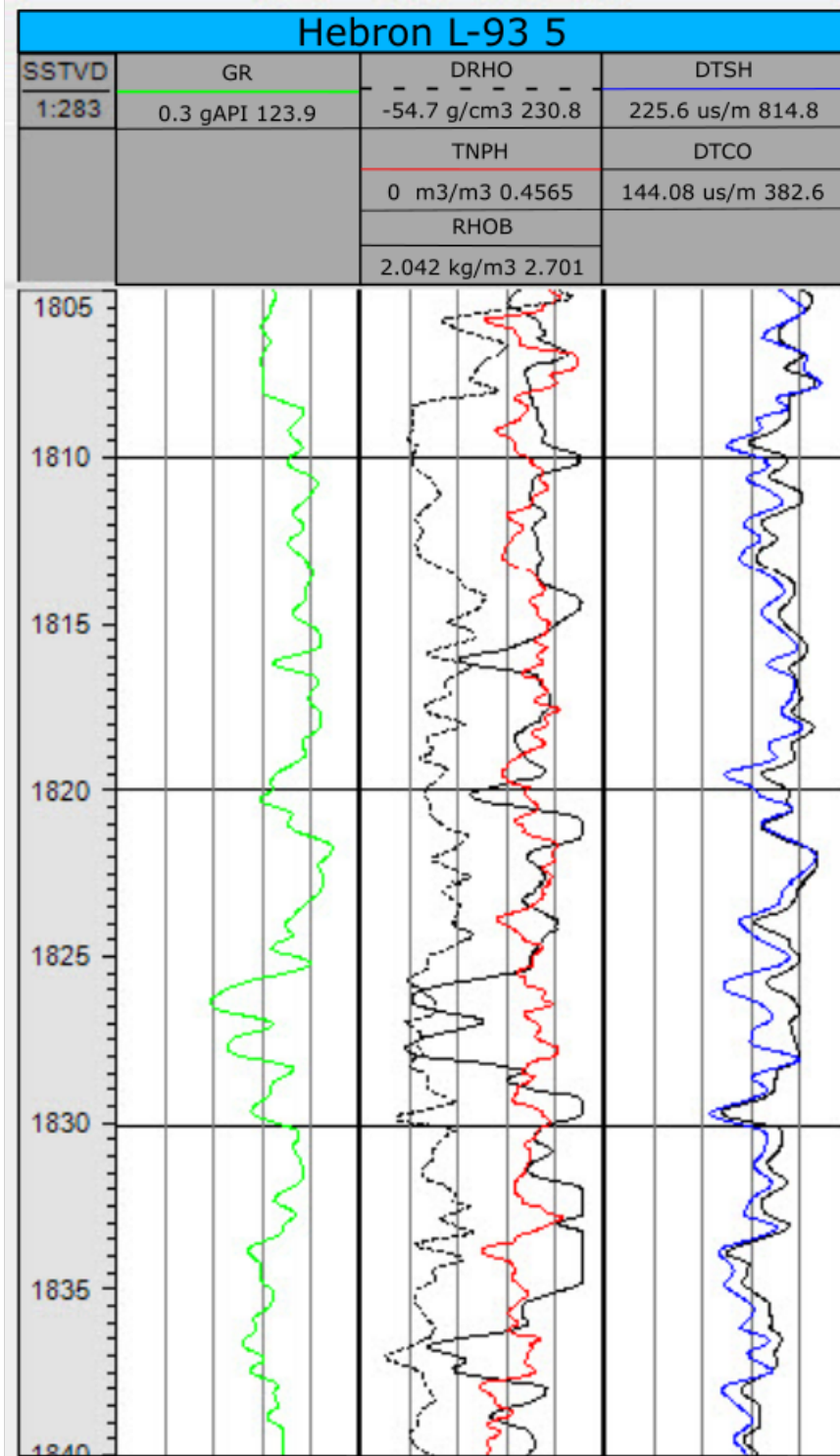


Figure 4.4: Enlarged view of digitized well logs for the Hebron L-93 5 well, showcasing the quality of the logs created through the digitization process. GR is the gamma ray log, DRHO is the density correction log, TNPH is the neutron log, DTSH is the shear wave travel time, and DTCO is the compressional wave travel time.

Once the density logs are available in Petrel, a porosity log is calculated using,

$$\phi = \frac{\rho_{ma} - \rho_{log}}{\rho_{ma} - \rho_{fluid}} \quad (4.1)$$

outlined in Vernik (2016); where ρ_{ma} is assumed to be $2650 \frac{kg}{m^3}$ for a clastic rock density and ρ_{fluid} is assumed to be $1000 \frac{kg}{m^3}$. The main zone of interest for the porosity log is the Ben Nevis reservoir zone, we use it in chapter 6 of this thesis for fluid substitution to generate the monitor velocity model.

4.1.3 Pool 1 Geological Model Boundary Polygon

The Pool 1 geological model boundary polygon is created based on the Pool 1 and Pool 2 geological model presented in the Hebron development plan (ExxonMobil, 2011) shown in Figure 4.5. Following a similar shape along contours and faults for the interpreted Top Ben Nevis surface and the Hebron production licence boundary (magenta polygon), the red polygon shown in Figure 4.6 is used as the boundary polygon for the Pool 1 geological model in this thesis.

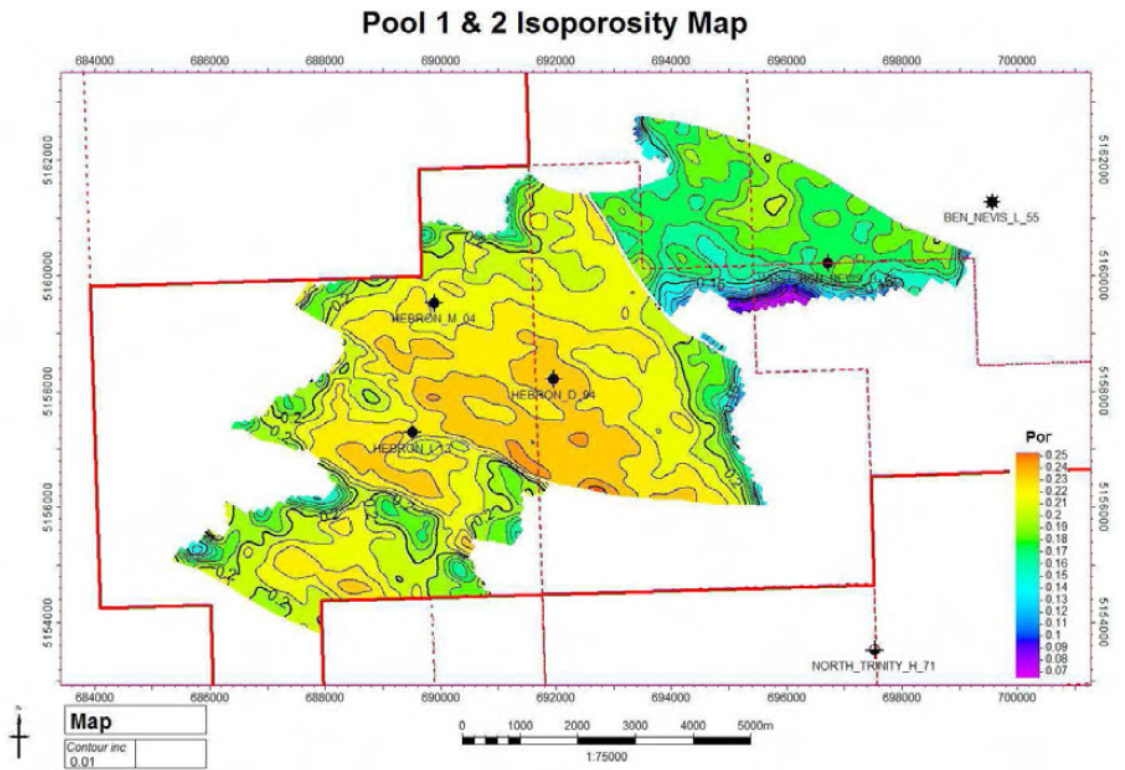


Figure 4.5: Pool 1 and Pool 2 combined geological model; where Pool 2 is the eastern fault block and Pool 1 is everything west of Pool 2 (from ExxonMobil, 2011).

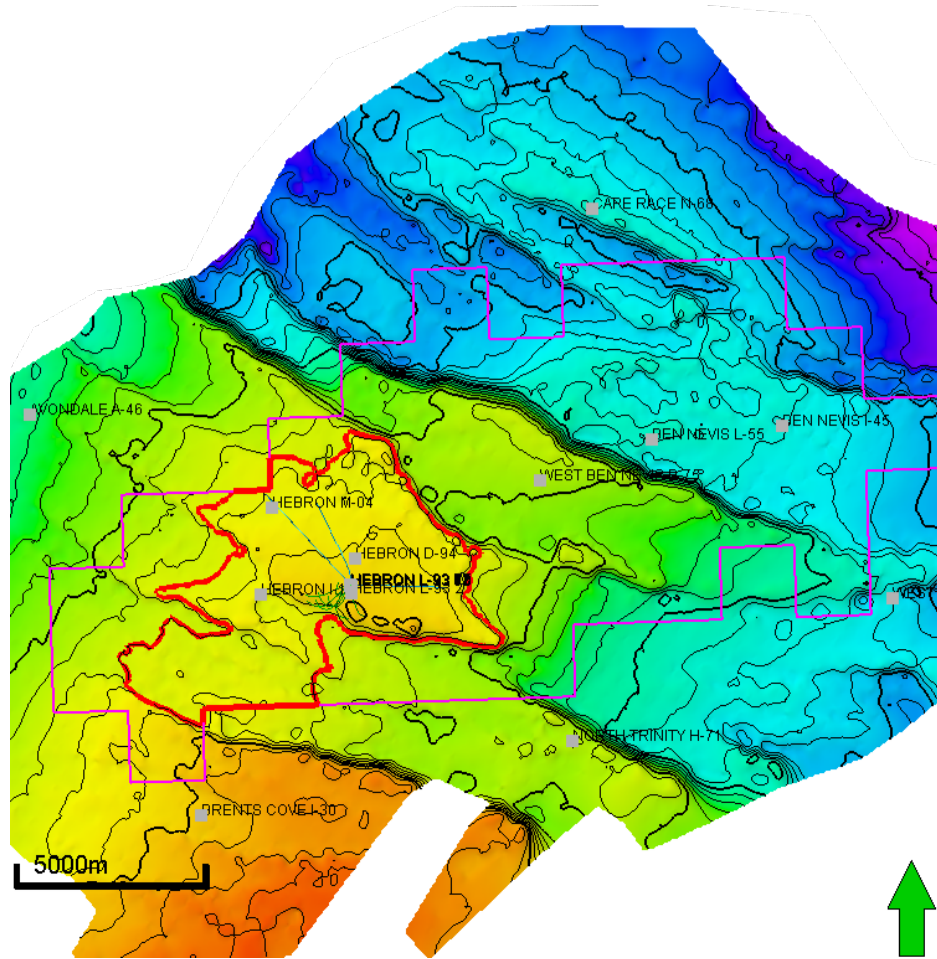


Figure 4.6: Pool 1 boundary (red polygon) for the geological model shown in this thesis overlain on top of the interpreted Top Ben Nevis surface; the magenta polygon is the production licence polygon for the Hebron Field and the green arrow points northward.

4.2 Building the Geological Model in Petrel

The Pool 1 geological model is constructed in the Petrel software following the workflow in Figure 4.1, using the inputs outlined in Section 4.1. The first step is to define the 3D grid of the model; this requires the Pool 1 boundary polygon (X & Y) and the surfaces of interest (Z) to define the geometry of the model (Figure 4.7).

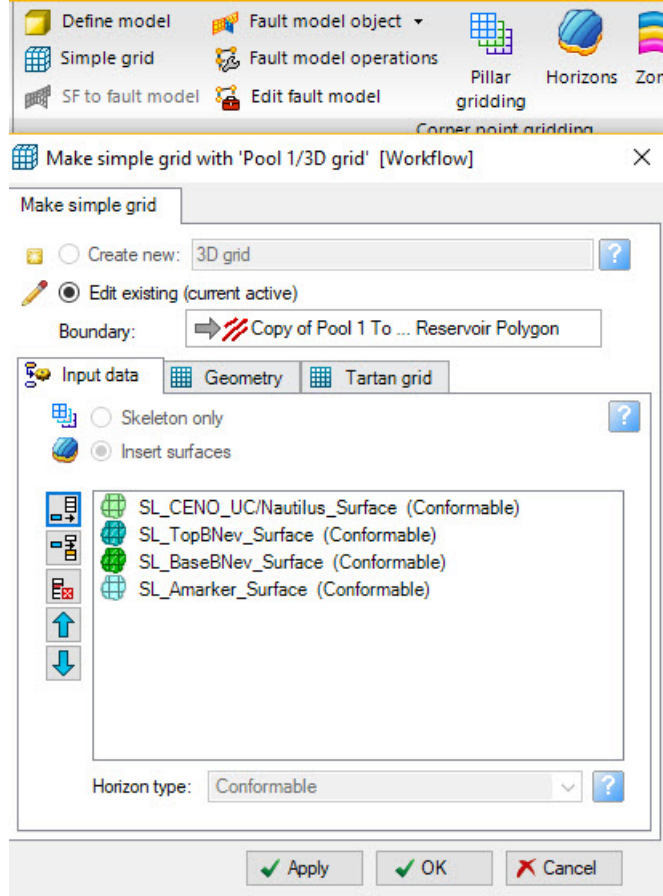


Figure 4.7: Geological Model Workflow Step 1: Define 3D grid; the XY boundary is the Pool 1 polygon in Figure 4.6 and the Z boundary comprise the four surfaces explained in Section 4.1.1.

Once the 3D grid is set up, the size of the cells within the 3D grid is set by defining layering (Figure 4.8). In this step, the desired size of the cells of the 3D grid is used to determine the number of layers,

$$\# \text{ of Layers} = \frac{\text{Layer Thickness}}{\text{Desired Cell Size}} \quad (4.2)$$

where layer thickness is measured within Petrel as the distance from one surface to the next. For the geological model shown in this thesis, the desired cell size was 2 m. 2 m is selected to be the cell size for these geological models to create a high resolution geological model while still keeping the number of cells within the model

low enough to prevent any computation issues while creating the model.

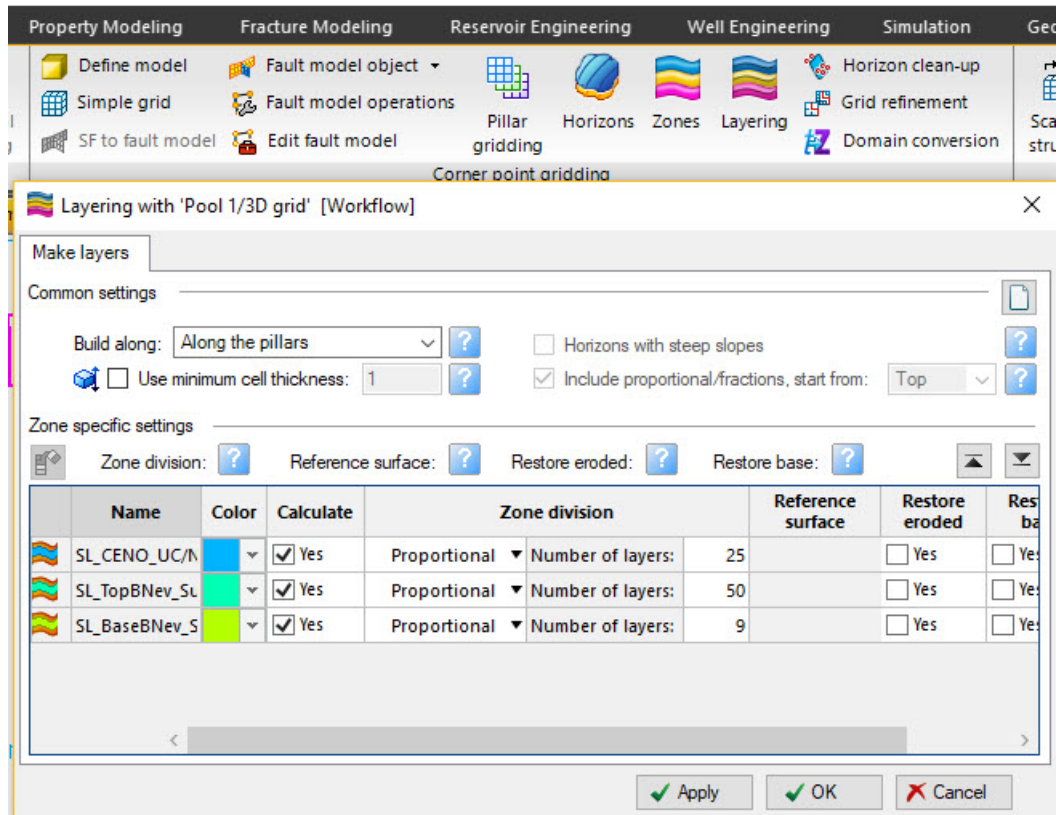


Figure 4.8: Geological Model Workflow Step 2: Define layering; the number of layers is calculated using Equation 4.2, where the desired cell size for the model is 2 m.

The next step in constructing the geological model is to create zones within the model. This is done to create units within the model that can have assigned properties. In the geological model for this thesis, there are three zones, the Nautilus zone (Top Nautilus - Top Ben Nevis Reservoir), the Ben Nevis zone (Top Ben Nevis Reservoir - Base Ben Nevis Reservoir), and the Avalon zone (Base Ben Nevis - Top A Marker) (Figure 4.9).

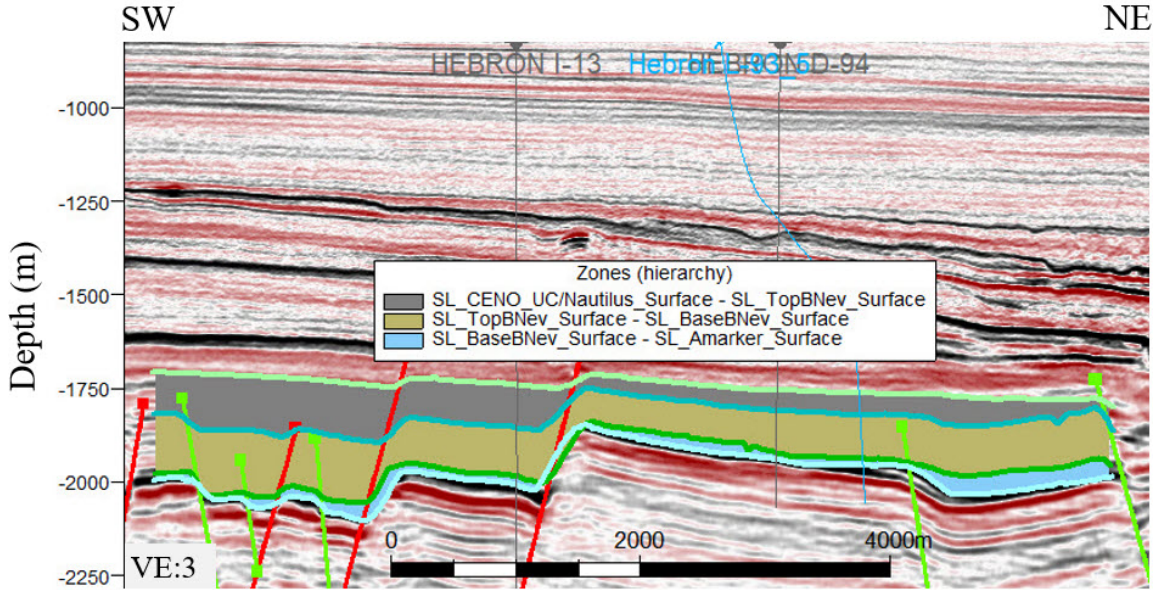


Figure 4.9: Geological Model Workflow Step 3: Geometrical modeling to create zones in the geological model; the Nautilus zone is grey, Ben Nevis zone is beige, and the Avalon zone is blue-grey.

Once zones are defined in the model, well data can be included within the 3D grid. For the wells in this thesis, logs are measured at a 0.1 m sample interval, but since the cell size within the model is 2 m, the log values must be averaged across each cell interval penetrated by the well (i.e. scaled-up). In the geological model, the density and the porosity logs for the Hebron I-13, Hebron M-04, Hebron D-94, and Hebron L-93 5 wells are up-scaled and are only assigned to the cells which contain these well penetrations highlighted in Figure 4.10.

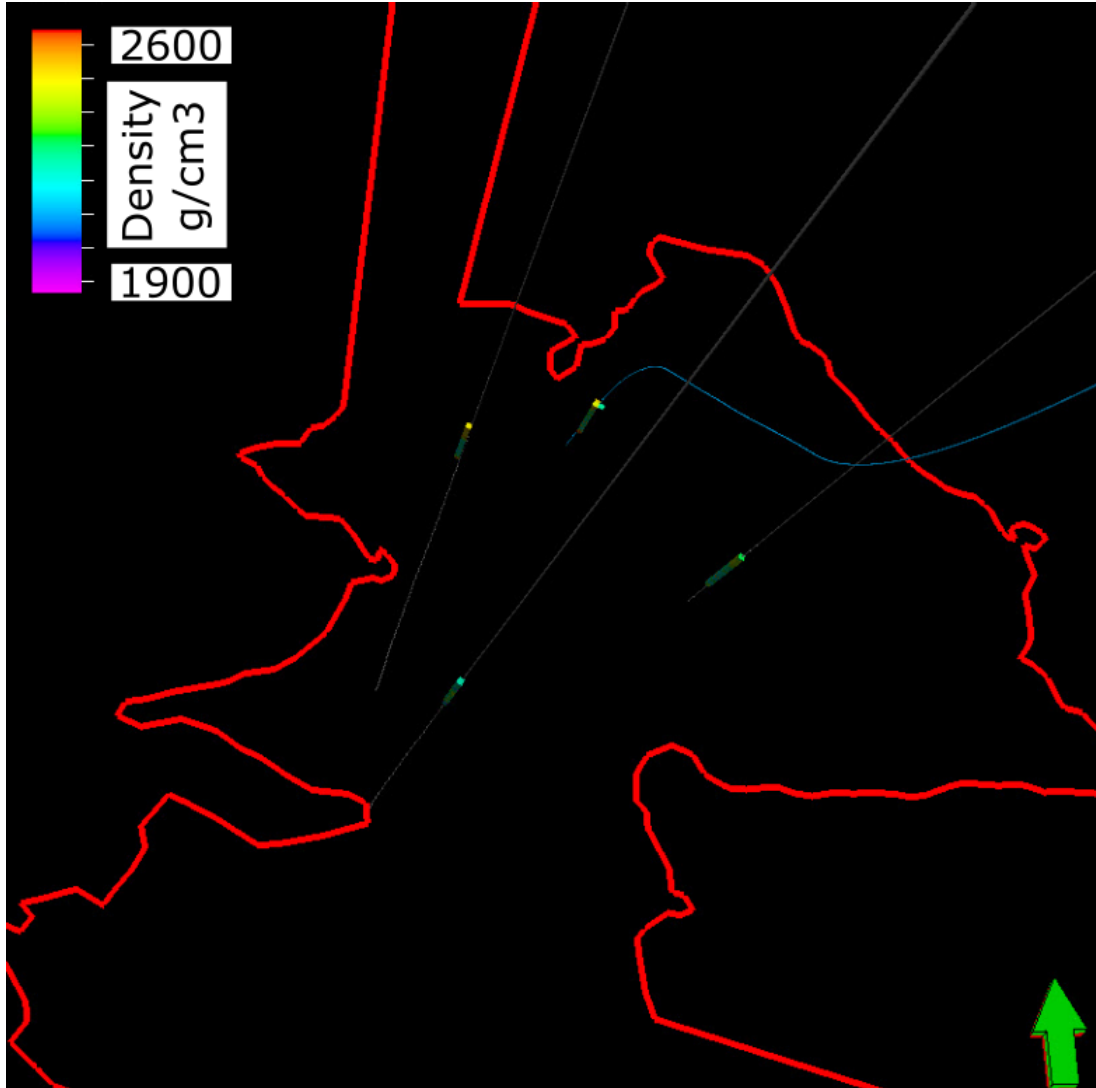


Figure 4.10: Geological Model Workflow Step 4: well log up-scaling; up-scales the high resolution (0.1 m) log values to the 2 m geological model cell size; shown here is the up-scaled density well log values for the Hebron I-13, Hebron M-04, Hebron D-94, and Hebron L-93 5 wells. The green arrow points northward.

The petrophysical modeling tool in Petrel allows for up-scaled log data within a 3D grid/model to be interpolated between, and extrapolated from, input wells. This creates a 3D model of a given property within the boundaries defined in Step 1. Shown in Figure 4.11 is the 3D model of the density property within Pool 1. We use the moving average method to fill in the 3D model; the moving average method is selected

as it produces a 3D model which looks geologically correct.

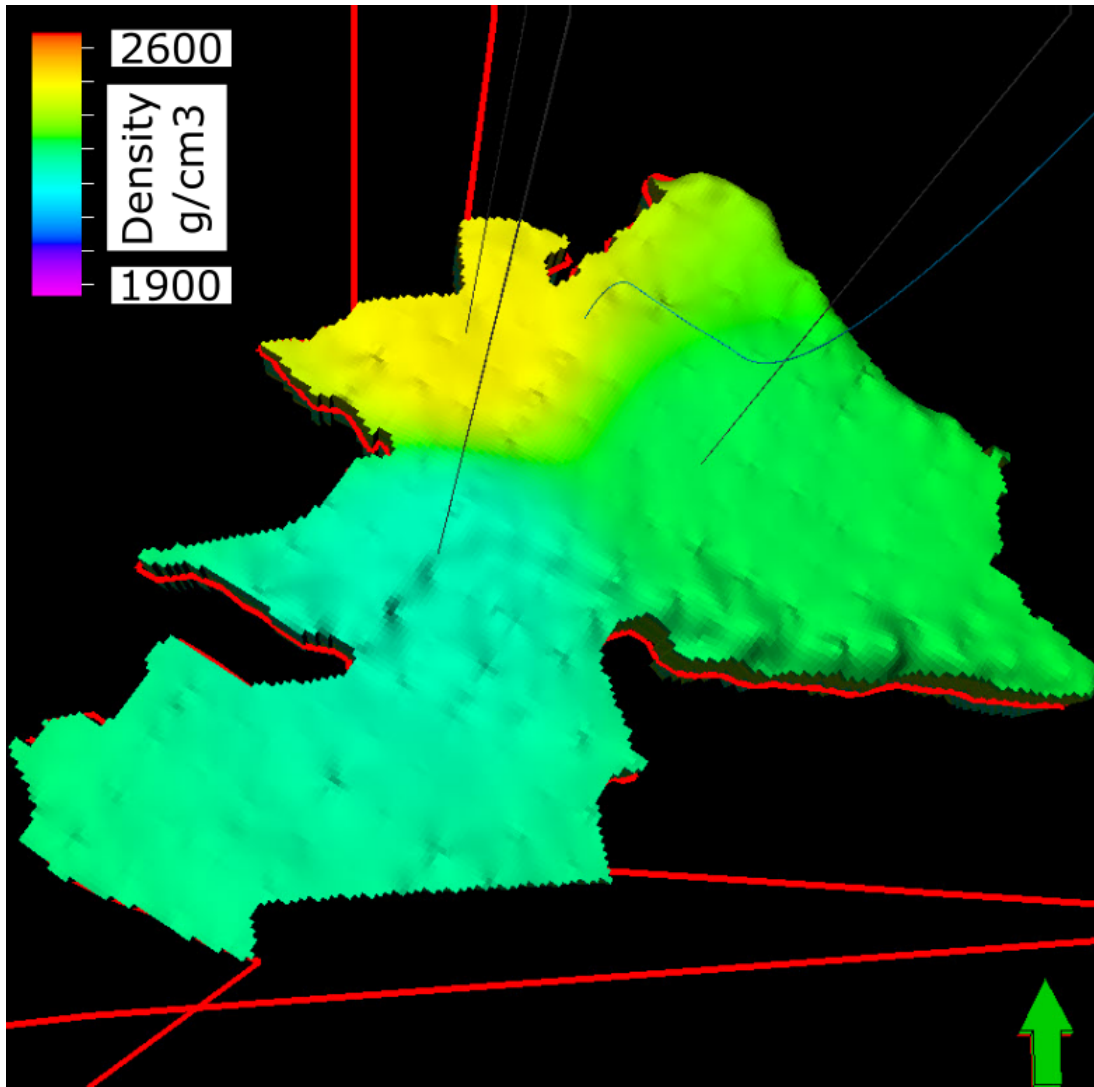


Figure 4.11: Geological Model Workflow Step 5: petrophysical modeling tool; shown here is the 3D density model created by propagating the up-scaled well log values for the Hebron I-13, Hebron M-04, Hebron D-94, and Hebron L-93 5 wells. The green arrow points northward.

4.3 Pool 1 Geological Model Results

The geological model building process creates two 3D property models (density and porosity) within the Pool 1 area. These models predict the rock properties within Pool 1 between drilled wells. These models will help in Chapter 6 of this thesis during the

fluid substitution work to create a post-production velocity model (monitor model).

4.3.1 Quality Control of the Pool 1 Geological Model Outputs

To ensure the quality of the geological property models, cross-sections of these models are displayed on seismic lines to examine the outputs. Figure 4.12 is an IL seismic section displaying the density model. This figure shows that the Nautilus zone is lowering in density considerably towards the SW. There was no considerable difference between the seismic response in the areas of higher density compared to the lower density areas in the model, indicating that the model is incorrectly representing the density of the Nautilus shale unit.

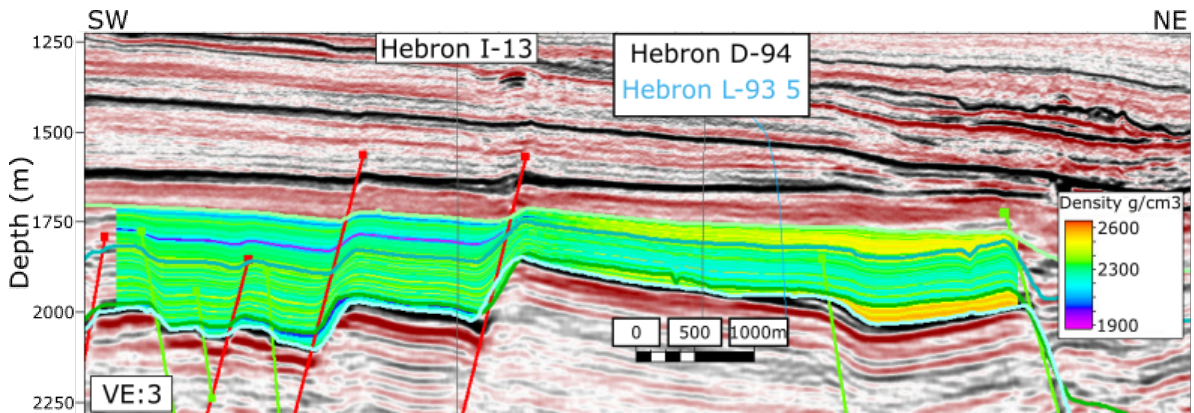


Figure 4.12: Cross-section through the 3D density model showing projections of 3 well penetrations that are inputs into the model.

The Hebron I-13 well log (Figure 4.13) shows the density log alongside the caliper log. Examining the blocked-off section of the Nautilus zone that we include in the model (~ 1750 - 1830 m), the caliper reading is larger than the drilled hole size of 311 mm, indicating a zone of borehole breakout. Within this zone, the density reading is contaminated by the drilling mud used to keep the borehole stable, likely leading to the anomalous Nautilus shale density seen in the southwestern portion of the geological

model. The rest of the Hebron I-13 well has a reasonable caliper reading indicating that the only problematic zone is the Nautilus shale.

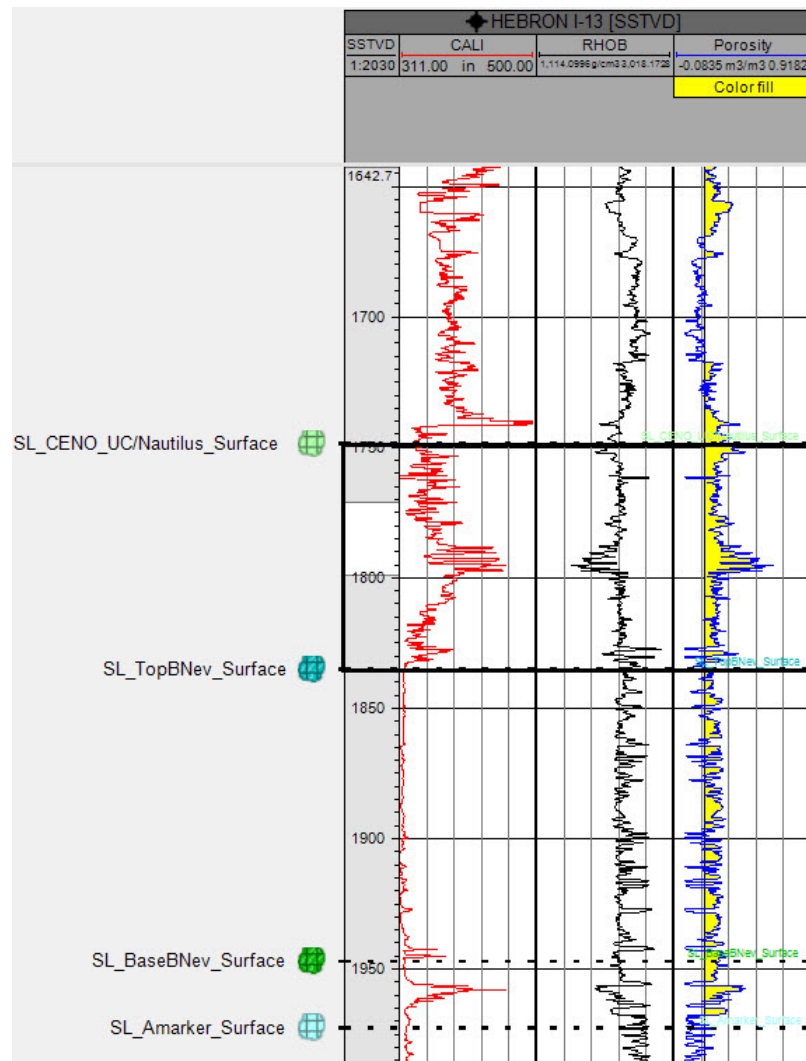


Figure 4.13: Hebron I-13 well log section with caliper (CALI), density (RHOB), and porosity shown; the porosity color fill cutoff is set at 14%. The black box indicates the region of borehole breakout.

4.3.2 Updating the Pool 1 Geological Model

After examining the density model, the Nautilus zone to the southwest is a problematic issue within the model. To fix this issue, the density logs for five additional production wells Hebron L-93 2, Hebron L-93 3, Hebron L-93 7, Hebron L-93 9, and

Hebron L-93 12 were all digitized following the methodology explained in 4.1.2. Figure 4.14 is the same cross-section as Figure 4.12 but updated with the additional production wells. From the addition of these production wells, the density of the Nautilus shale zone is updated to a more reasonable representation across the model. It is important to note that the digitization and inclusion of the well logs was stopped when the wellbore went horizontal to prevent anisotropic density ratios to lower uncertainty within the density and porosity models.

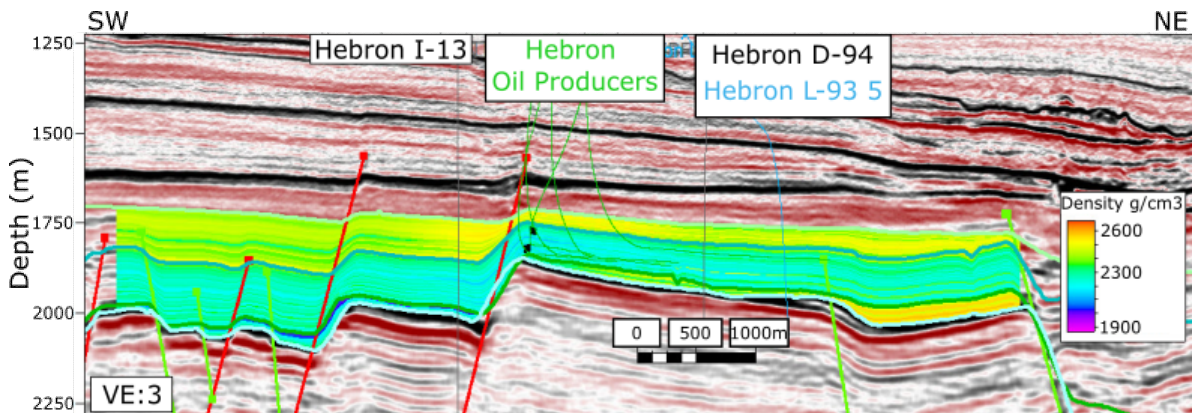


Figure 4.14: Updated cross-section through the 3D density model showing projections of 8 well penetrations that are inputs into the model. Note the continuous high density for the Nautilus shale zone compared to Figure 4.12.

The corresponding porosity model cross-section shown in Figure 4.15 shows porosity values ranging from 15% to 30% for the Ben Nevis formation in Pool 1. Comparing these numbers to average porosity numbers discussed in 2.2.2, these are reasonable numbers for the Ben Nevis Reservoir within Pool 1 of the Hebron Field. An additional comparison is made using core analysis studies for the core from the Hebron I-13, Hebron D-94 and Hebron M-04 wells (Core Laboratories, 1981; Core Laboratories, 1999; Core Laboratories, 2000). The model porosity is in agreement with the measured porosity values for each of these wells in the porosity model; thus, the model is considered to be accurate for Pool 1.

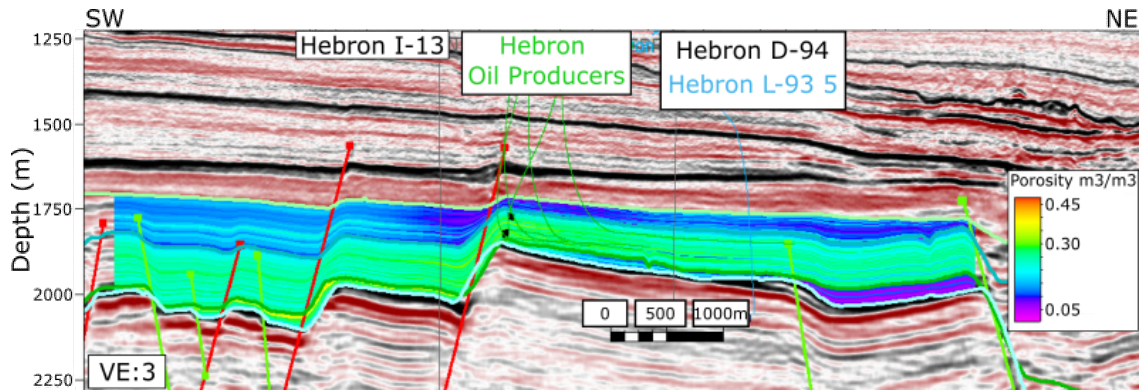


Figure 4.15: Cross-section through the 3D porosity model showing projections of 8 well penetrations that are inputs into the model.

The addition of extra wells is deemed more appropriate than removing Hebron I-13 since it is the only well drilled in the secondary fault block of Pool 1. Since only the Nautilus shale zone was affected by borehole breakout and the Ben Nevis reservoir rock properties are still accurate, the important information is not contaminated. Since we use an arithmetic average of the properties in the petrophysical modelling step, the Hebron I-13 Nautilus shale values return to the background trend from the surrounding wells after a short distance (Figure 4.16).

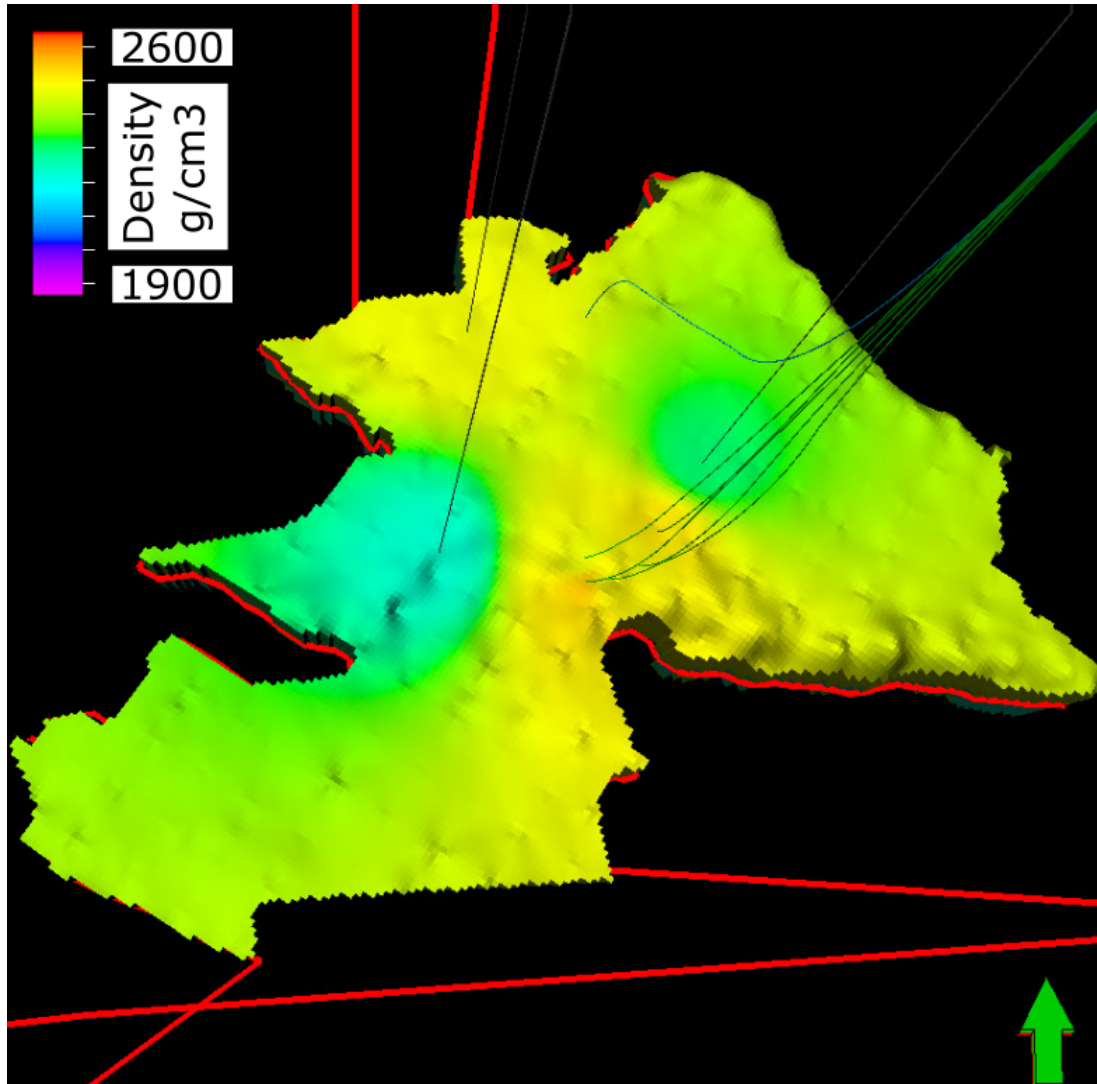


Figure 4.16: Updated petrophysical modeling step of the geological modeling process. This is an updated version of Figure 4.11 with the addition of five production wells: Hebron L-93 2, Hebron L-93 3, Hebron L-93 7, Hebron L-93 9, and Hebron L-93 12. The green arrow points northward.

Chapter 5

Hebron Field Baseline Velocity

Model

In a 4D seismic study, there are two necessary velocity models. A baseline velocity model represents the subsurface before producing a reservoir/field, and a monitor model represents the subsurface after some amount of production of a reservoir/field. In this chapter, we discuss the building of the baseline velocity model. The seismic images used to create the seismic data in this thesis are plotted in depth. With the survey documentation received from the CNLOPB, there is documentation on the velocity model building process (CGG, 2015b). This documentation includes Figure 5.1, which acts as a benchmark for the baseline velocity model we build in this chapter. The model in Figure 5.1 was built using FWI, high-definition tomography, fault-constrained tomography, geological horizons, fault horizons, extra near and far offsets, and sonic logs from the following wells: Avondale A-46, Ben Nevis I-45, Ben Nevis L-55, Brent's Cove I-30, Cape Race N-68, Hebron D-94, Hebron I-13, Hebron M-04, North Trinity H-71, West Ben Nevis B-75, West Bonne Bay C-23, and West Bonne Bay F-12/F-12Z (CGG, 2015a). The benchmark model underwent a significant

velocity model building process, which cannot be replicated here due to the relatively limited data available for this thesis project.

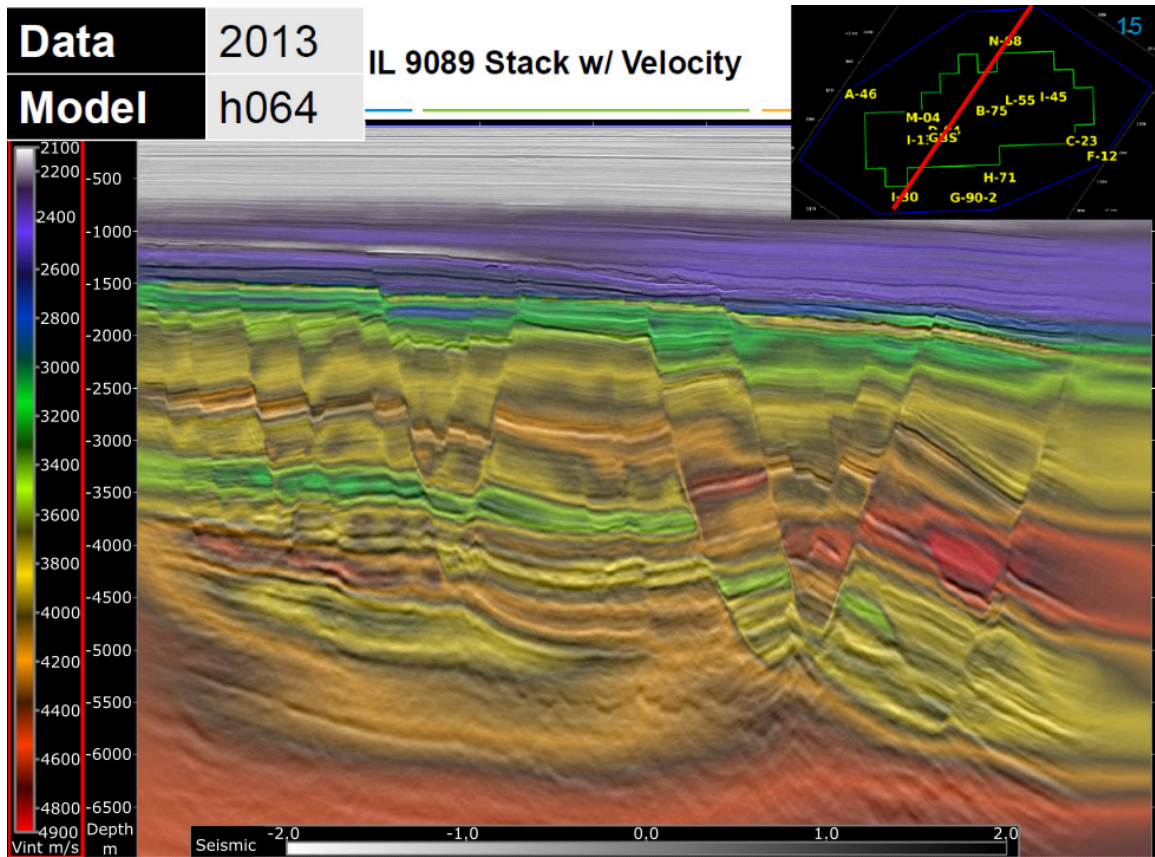


Figure 5.1: Benchmark velocity model. This is a section from the velocity model that was used to depth convert the seismic data used in this thesis from time and was built using an extensive FWI process. (from CGG, 2015b)

5.1 Hebron Field Baseline Velocity Model Inputs

The inputs for the baseline Hebron Field velocity model overlap with some of the benchmark model inputs but are not as extensive. Inputs include the digitized versions of the sonic logs for the same list of wells as the benchmark model (wells donated by IHS Energy were not re-digitized) plus the sonic log from Hebron L-93 5, and all twelve 3D surfaces created using the horizon interpretations explained in Chapter 3.

5.1.1 Sonic Log Preparation

Sonic logs are a measure of slowness or inverse velocity of the subsurface at a well location. There are two sonic logs that can be measured within a well, the compressional and shear (P & S) sonic logs, representing the P & S velocities of the subsurface; albeit that sonic logs are acquired at a much higher frequency compared to seismic data. Generally, a sonic log is calibrated with another velocity measuring tool such as a vertical seismic profile (VSP) or a checkshot survey to account for any data errors occurring during the logging process (i.e. borehole breakout zones) (Liner, 1999). The checkshot data received from the CNLOPB were not readily usable, so the sonic logs were used uncalibrated. To convert the sonic logs into a velocity log within Petrel, each sonic log was calibrated with itself (Figure 5.2).

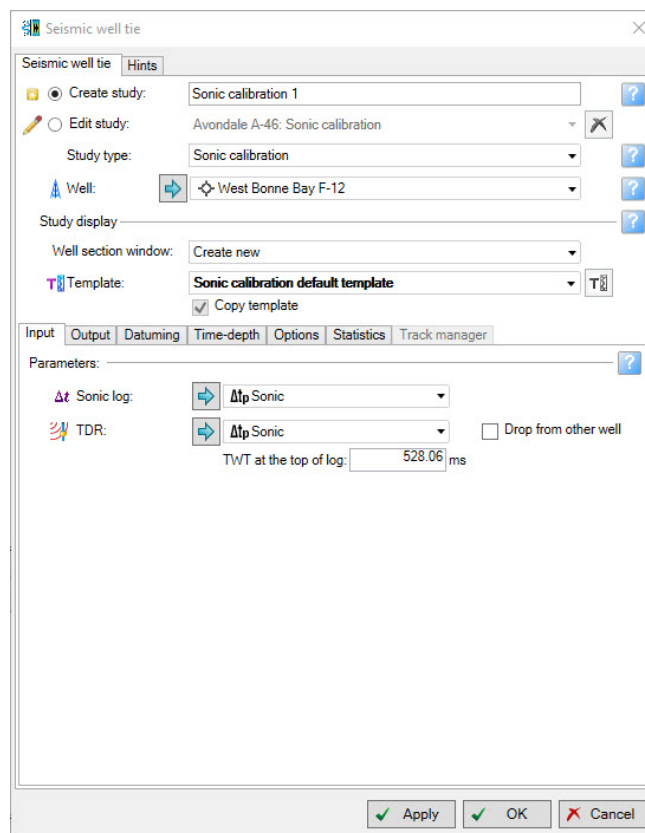


Figure 5.2: Sonic calibration settings within the Petrel software showing how the sonic well log was calibrated with itself.

This step was completed to convert from slowness to velocity. The drift curve indicates how the sonic log has changed with depth during the calibration process; therefore, a vertical drift curve line is desired for each well. The drift curve for each well is inspected to ensure that no contamination of the data occurred during this process (Figure 5.3). The input interval velocity curve generated from the sonic calibration was chosen over the output interval velocity curve to further limit data contamination.

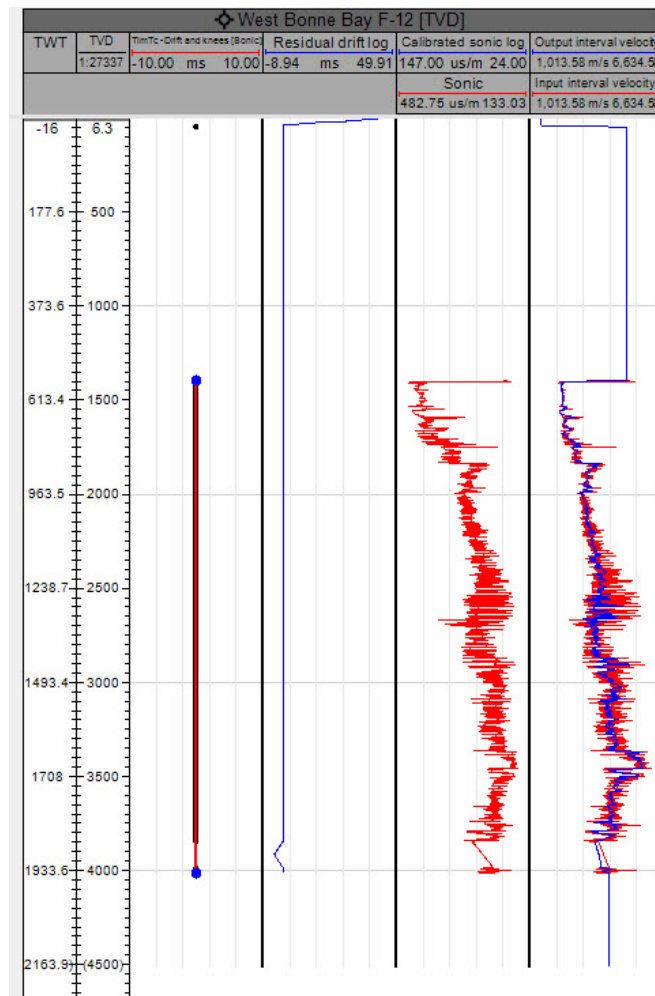


Figure 5.3: Sonic calibration outputs showing the vertical uncontaminated drift curve (2nd track). The input sonic data are in red on the 3rd track, and the velocity data used for this well are in red on the 4th track.

5.2 Hebron Field Baseline Velocity Model - Attempt 1

The first attempt at building the baseline velocity model is made using the Petrel software's advanced modeling tool. This tool is generally used for depth conversion of well log data and seismic constraints. Figure 5.4 shows the setup of this tool for the first attempt at building the velocity model; here, the twelve input surfaces are used to define velocity zones with well top information correcting their locations at each well with the sonic information set to be the time-depth relation (TDR) from the well. This velocity modeling tool uses a linear velocity function,

$$V = V_0 + KZ \tag{5.1}$$

where V_0 is defined by the sonic log corrected to the surface location, and K is calculated using the sonic log and is adjusted by a constant value determined by Petrel.

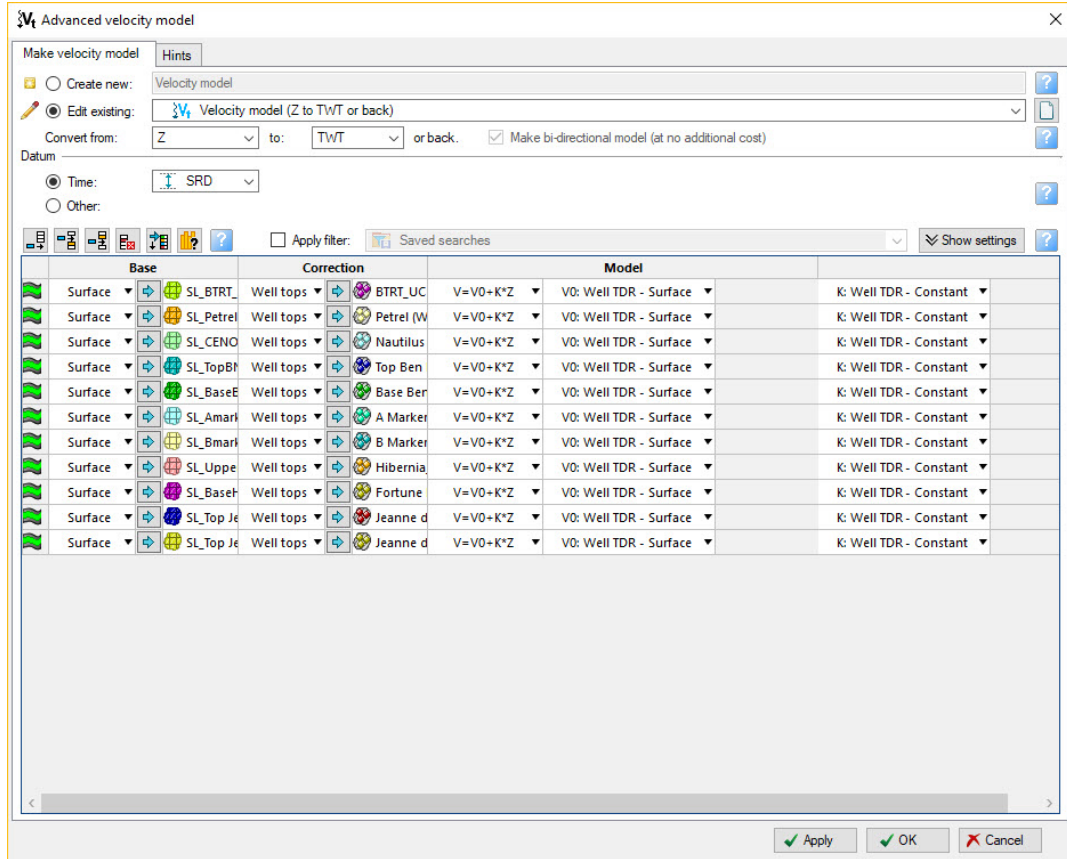


Figure 5.4: Settings for Petrel’s Advanced velocity model tool used to construct the first attempt of the Hebron Field Baseline Model.

Figure 5.5 is the result from the first baseline velocity model attempt; overall, this is an inadequate solution and has no resemblance to the benchmark model. The ambiguity of the advanced velocity model tool inspired the workflow used for the second attempt at building the baseline velocity model.

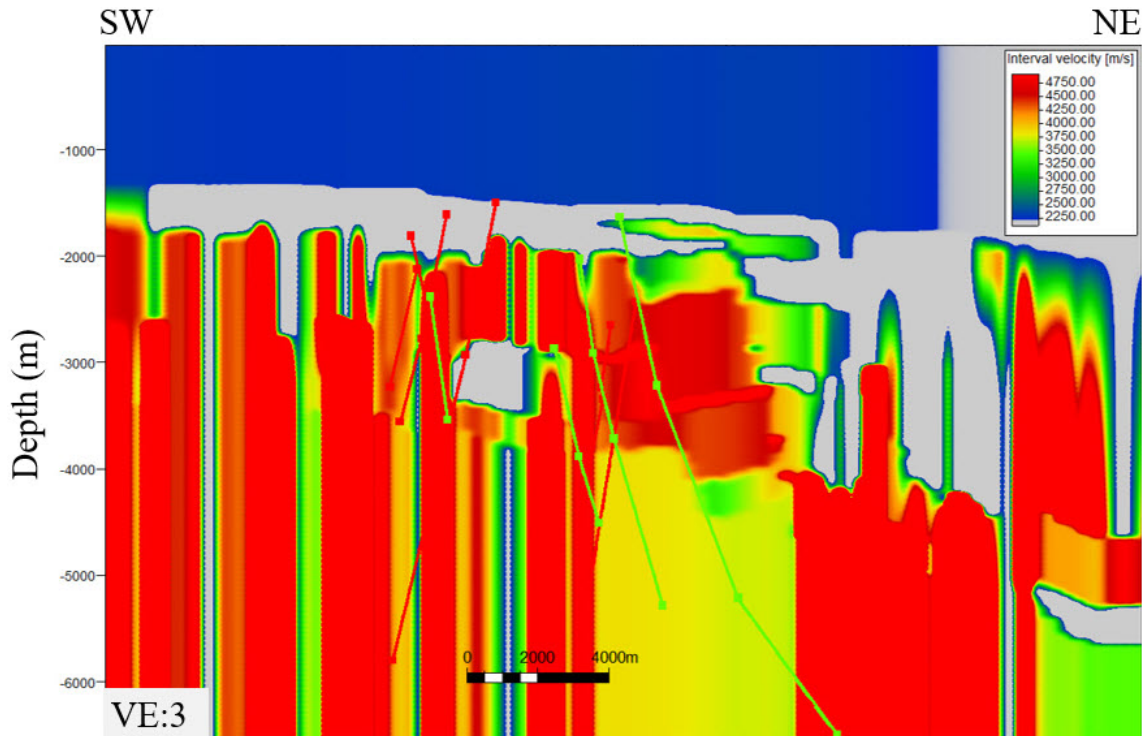


Figure 5.5: IL 9121 displaying the first attempt at a velocity model for the Hebron Field; shown on the figure are Pool 1 faults for a frame of reference and the color bar was selected to resemble the benchmark model color bar.

5.3 Hebron Field Baseline Velocity Model - Attempt 2

After the poor result of the first attempt using the Petrel velocity modeling tool, a workflow (Figure 5.6) using a 3D grid-based approach similar to the geological model workflow in Chapter 4 (Figure 4.1) is designed to build a velocity model in a similar fashion.

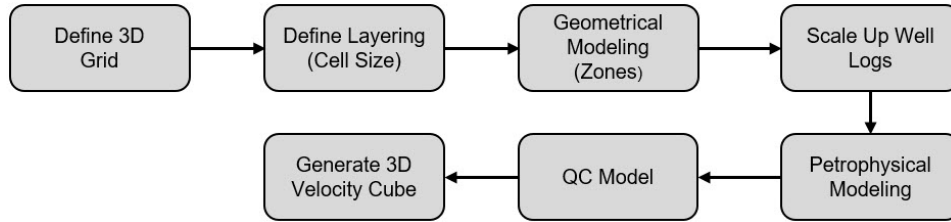


Figure 5.6: Workflow used to build the second attempt of the Hebron Field baseline velocity model.

The construction of this model follows a very similar fashion as the one explained in section 4.2. The first step in this process is to define a model/3D grid; this time, the only inputs are the twelve surfaces for the X, Y, and Z constraints of the model (Figure 5.7).

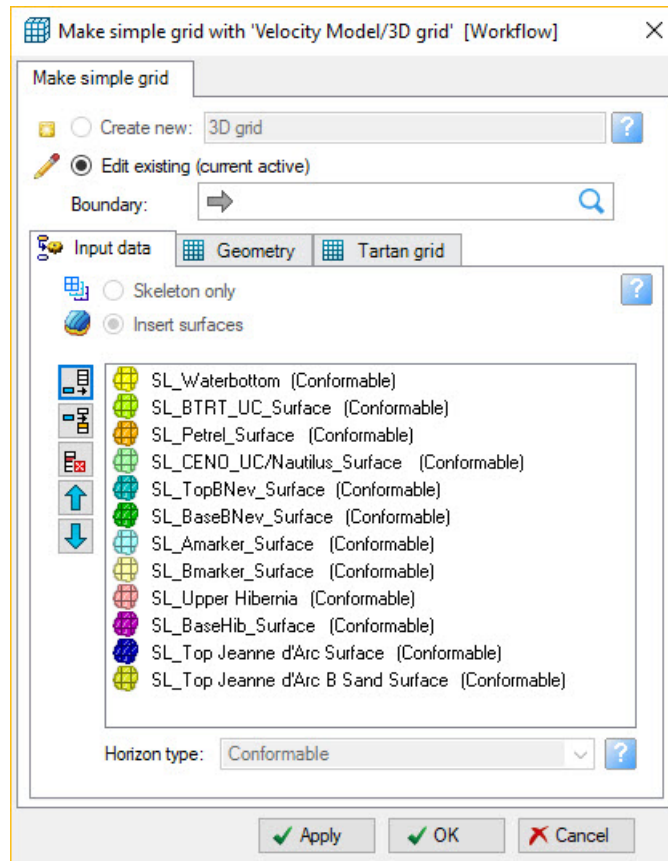


Figure 5.7: Velocity Model Workflow - Define 3D grid; The X, Y, and Z boundaries are defined by the twelve input surfaces.

Setting up the cell sizes with the 3D grid for the velocity model is similar to that of the geological model, using Equation 4.2. Since the velocity model is much larger (i.e. full Hebron Field vs. Pool 1), a varying cell size approach is used. This is done by measuring the distance between each surface at a fixed location to determine each layer thickness. From here, the geology and size of each layer are examined to determine their importance in the velocity model. In general, limestones were given a smaller cell size due to their higher velocity compared to clastic sedimentary rocks (shales and sands). Sands and shales are given a larger cell size as their velocity will not vary much across an interval. Finally, reservoir units/associated seal rocks are given a small cell size to represent their importance in the model (Table 5.1).

Layer	Units	Distance Measured	Rounded	Rounded Distance	Desired Cell Size	Number of Layers
Water Bottom - Base Tertiary Unc.	Variable (majority shale & sandstone)	1425	Yes	1500	50	30
Base - Tertiary Unc. - Petrel	Shale	140	Yes	150	10	15
Petrel - Cenomanian Unc.	Limestone with interbedded shales	590	Yes	600	25	24
Cenomanian Unc. - Top BNEV	Shale	50	No	N/A	5	10
Top BNEV - Base BNEV	Reservoir sandstone	100	No	N/A	5	20
Base BNEV - Top A Marker	Secondary reservoir sandstone	30 - 160	No	N/A	5	15
Top A Marker - Top B Marker	Limestone units with shale and sands	950	No	N/A	25	38
Top B Marker - Top Upper Hibernia	Limestone unit	50	No	N/A	10	5
Top Upper Hibernia - Top Fortune Bay	Sandstone	615	Yes	600	20	30
Top Fortune Bay - Top Jeanne d'Arc A Sand	Shale	275	No	N/A	25	11
Top Jeanne d'Arc A Sand - Top Jeanne d'Arc B Sand	Sand	590	Yes	600	20	30

Table 5.1: Velocity model desired cell sizes and their requisite number of layers. Layer thicknesses (distance measured) were measured on IL 9281 between the intersection with XLs 7201 and 7361.

After setting up the 3D grid, zones are created between the input surfaces. These zones are used to assign properties to the cells created in the previous step. Shown in Figure 5.8 are all of the zones within the velocity model.

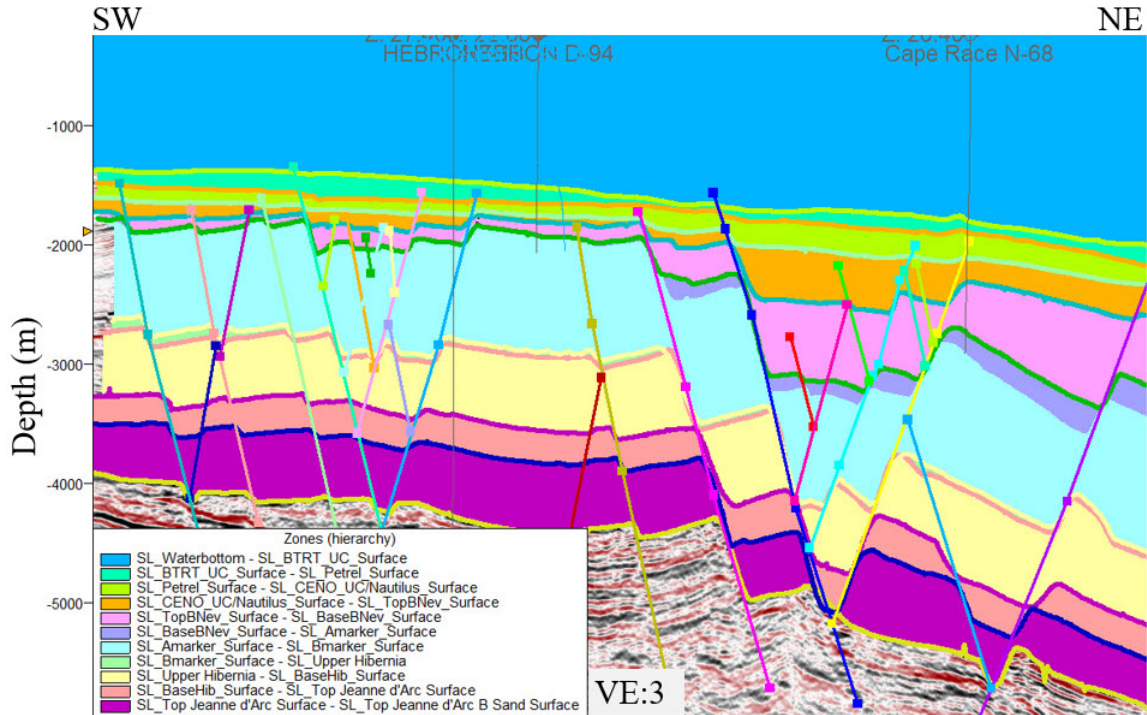


Figure 5.8: Zones defined by the twelve input surfaces within the velocity model.

Using the well log up-scaling tool, the input interval velocity (calibrated sonic) log is re-sampled to fit the defined cell size for each layer. Finally, these up-scaled well logs are extrapolated throughout each zone to create a 3D-grid based velocity model. Once the model is complete, the output property can be easily turned into a 3D seismic cube; for this velocity model, the survey setup is an IL and XL every 25 m and a depth slice every 5 m (Figure 5.9).

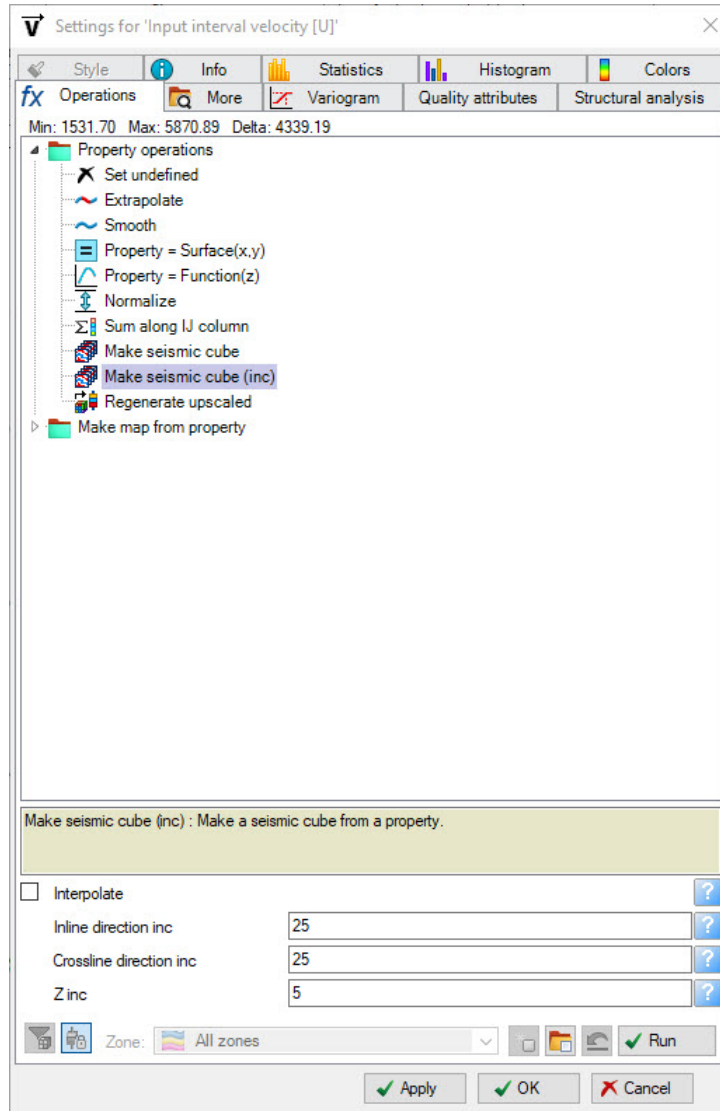


Figure 5.9: Survey setup for the 3D velocity seismic cube created using the 3D-gridded velocity property.

5.3.1 Attempt 2 - Hebron Field Baseline Velocity Model Results

The second attempt at recreating the benchmark model using a 3D-grid based approach is shown in Figure 5.10. Overall, the result using this methodology create a model that resembles the benchmark model. In the Pool 1 area (area in the center of

the model with multiple well penetrations), the velocity structure closely resembles the benchmark model; this is the key area of the model since it is the focus of the 4D seismic study.

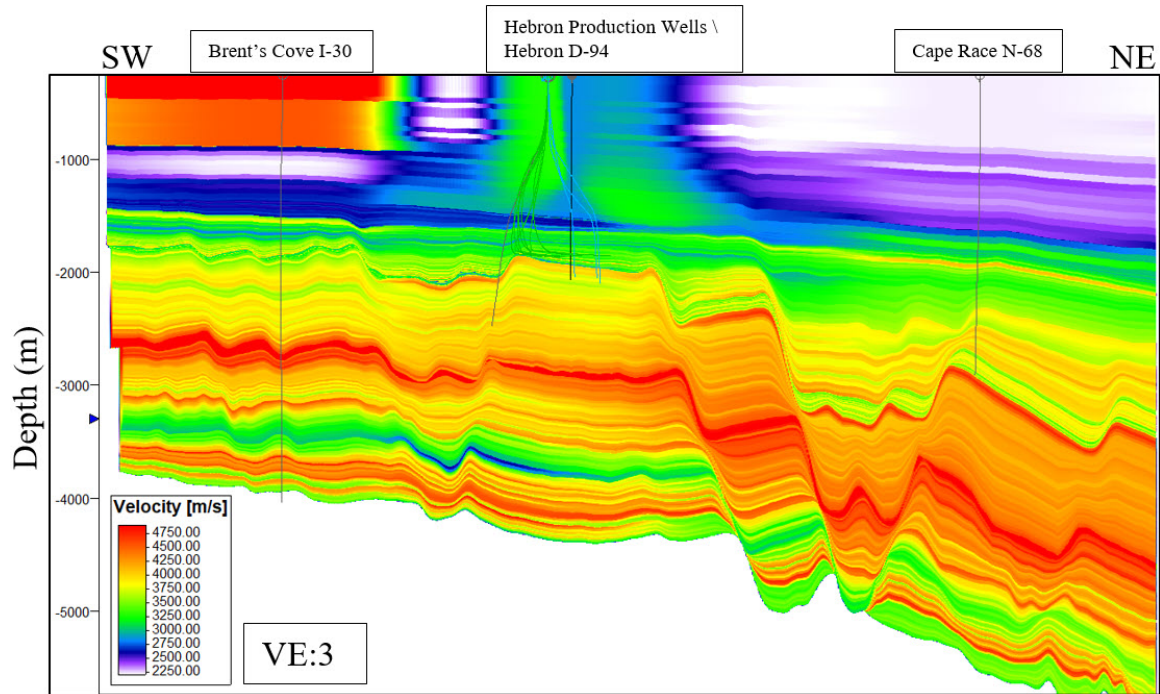


Figure 5.10: Velocity model using the 3D-grid based approach outlined in Figure 5.6. Line location is approximately IL 9089, and the color bar is set to match the benchmark model.

5.3.2 Quality Control of the Hebron Field Baseline Velocity Model

The model in Figure 5.10 resembles the benchmark model in both structure and velocity for most of the model. The Tertiary sediment velocities (0 - 1500 m) of the model are both extremely noisy and contain unrealistic values. Upon further examination of the individual well logs, anomalous velocity values were discovered for a few wells (Figure 5.11). For wells with these anomalous values, such as Brent's Cove I-30, these values are truncated to the start of the well log; for logs with realistic Tertiary velocity values such as West Bonne Bay C-23, these logs are left unaltered

(Figure 5.11).

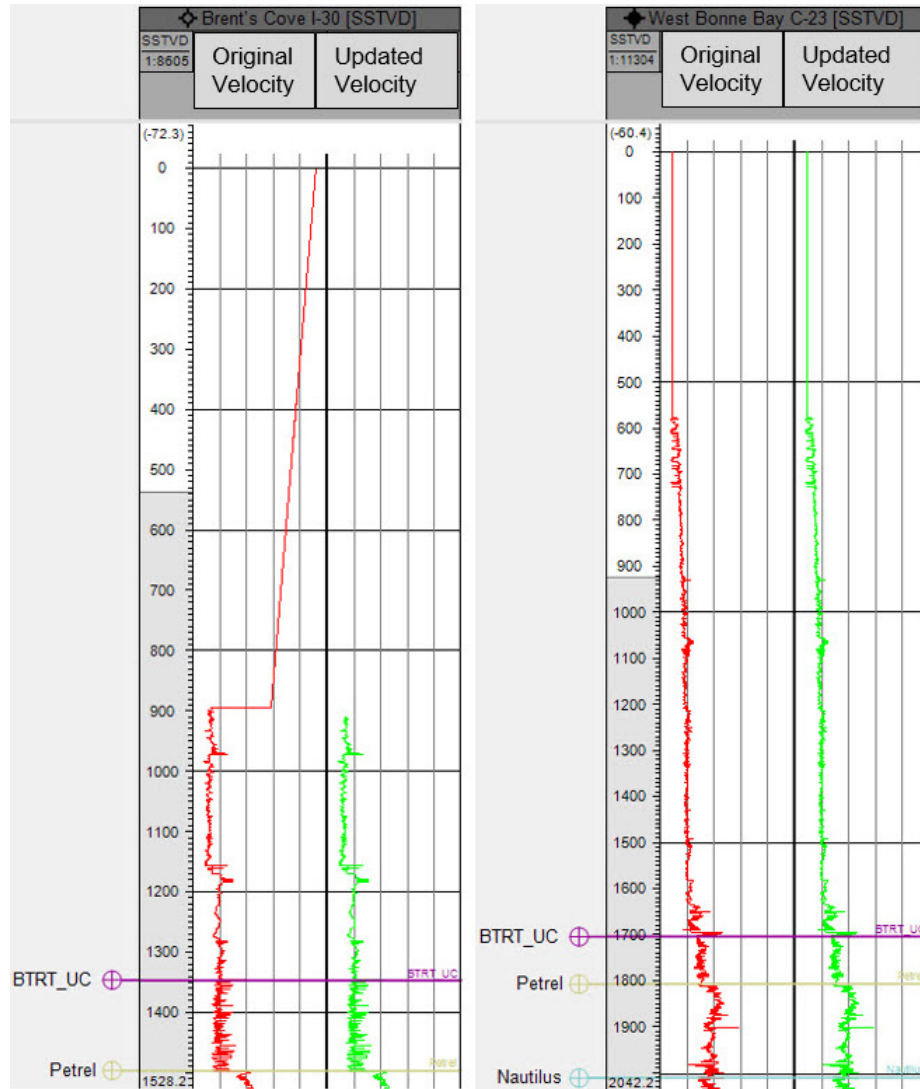


Figure 5.11: Brent's Cove I-30 (Left) and West Bonne Bay C-23 (Right) velocity logs highlighting the need to trim select velocity logs and keep others intact.

Upon adjusting the anomalous Tertiary log values, the velocity model looks much more reasonable and closer to matching the benchmark model (Figure 5.12). The Tertiary velocities now start at $\sim 1500 \frac{m}{s}$ and increase with depth, which is a reasonable assumption for a Tertiary sediment velocity curve (Van Avendonk et al., 2006). Overall, this is deemed to be an acceptable baseline velocity model for the 4D seismic

study on the Pool 1 reservoir of the Hebron Field.

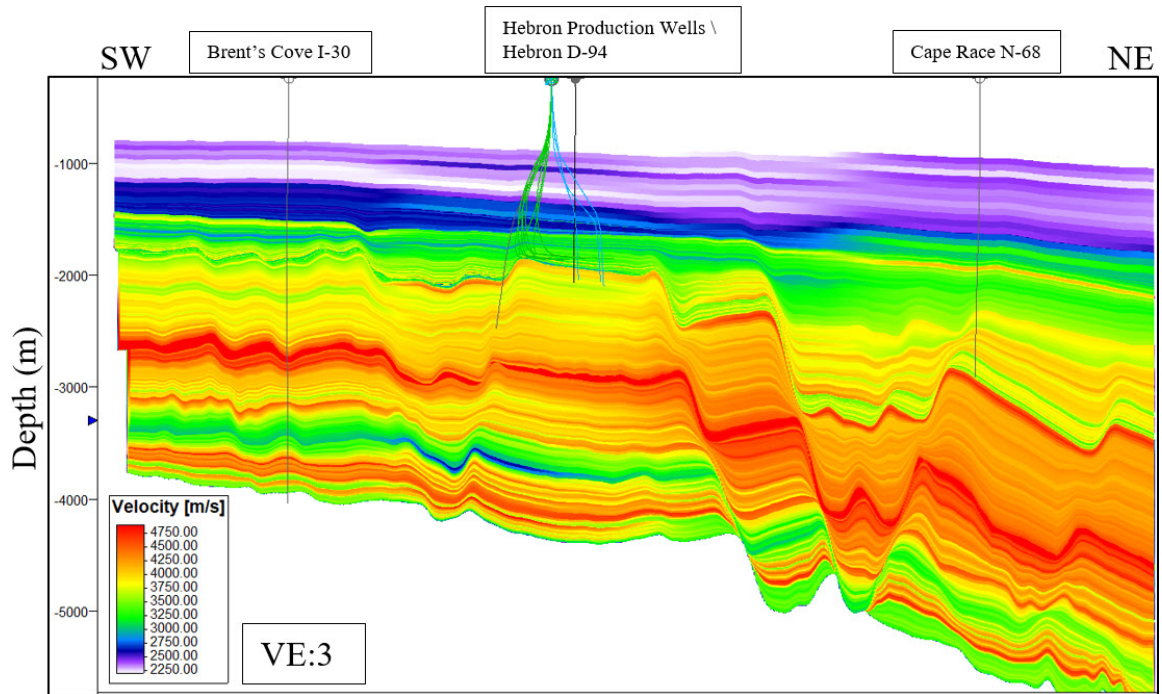


Figure 5.12: Velocity model using the 3D-grid based approach outlined in Figure 5.6 after QCing of select velocity logs. Line location is approximately IL 9089, and the color bar is set to match the benchmark model.

Chapter 6

Hebron Field Monitor Velocity Model

In this chapter, we will discuss the construction of the monitor model representing the Hebron Field after some production of the Pool 1 reservoir. The monitor model is generated through a log fluid substitution process using the RokDoc software completed for each of the wells drilled within Pool 1.

6.1 Log Based Fluid Substitution

To induce an accurate velocity change within the baseline velocity model, we use the RokDoc software to synthetically update the well log by replacing a portion of the pore space with water compared to the assumed initial oil fill. This technique uses

Gassmann's equation,

$$\begin{aligned}\frac{K_{sat}}{K_s - K_{Sat}} &= \frac{K_{Dry}}{K_s - K_{Dry}} + \frac{K_f}{\phi(K_s - K_f)}, \\ \mu_{Sat} &= \mu_{Dry}, \\ \text{and} \\ \rho_{Sat} &= \rho_{Dry} + \phi\rho_f,\end{aligned}\tag{6.1}$$

where K_{Sat} and μ_{Sat} represent the bulk and shear moduli of the fluid saturated rock, respectively, with ρ_{Sat} representing the saturated rock density (Johnston, 2013). K_{Dry} , μ_{Dry} , and ρ_{Dry} represent the bulk modulus, shear modulus, and the density of the unsaturated rock framework; K_s is the bulk modulus of the mineral grains making up the rock framework, K_f is the bulk modulus and ρ_f is the density of the fluid filling the porosity of the rock (ϕ) (Johnston, 2013). This equation predicts the bulk modulus, shear modulus, and density for a rock saturated with a given initial fluid (Fluid A) which is then fully or partially replaced by a second fluid (Fluid B) as depicted in Figure 6.1. For the fluid substitution performed within RokDoc for the Pool 1 reservoir, Fluid A is oil and Fluid B is water from water injector wells, which aim to displace the oil toward oil producing wells. Using this fluid substitution approach, we assume that only the fluid density is changing, so any subsurface perturbations will be only due to the density perturbation and not any pressure changes.

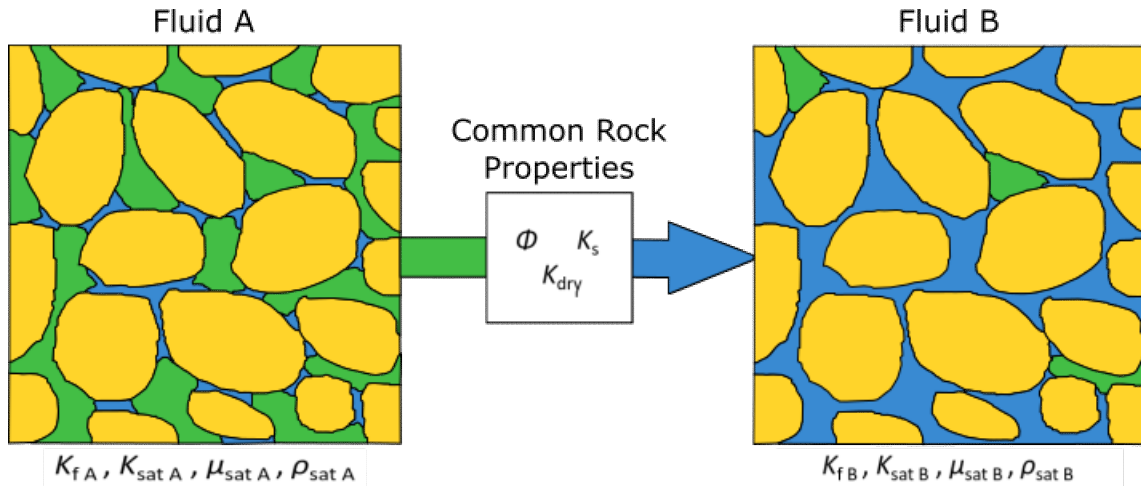


Figure 6.1: Illustration of the general fluid substitution problem for a rock originally saturated with Fluid A that is being replaced by Fluid B. (after Johnston, 2013)

6.1.1 Fluid Properties of the Pool 1 Reservoir

To accurately model the fluid replacement of the oil within the Pool 1 reservoir logs with the data available, the fluid properties of the oil must be accurately assigned in the fluid substitution process. Illustrations of Gassmann's equation predictions of P-wave velocity for differing saturations of oil and gas are shown in Figure 6.2. By comparing a heavy oil-water replacement scenario to an oil-water replacement, the P-wave velocity changes very little for a heavy oil scenario but for the oil water scenario the P-wave velocity increases with increasing water saturation. This is because the bulk modulus of a heavy oil is closer to water compared to the oil bulk modulus, thus accurately representing the fluid parameters of both the Pool 1 oil and the water replacing the oil utilizing the data available is extremely important (Johnston, 2013).

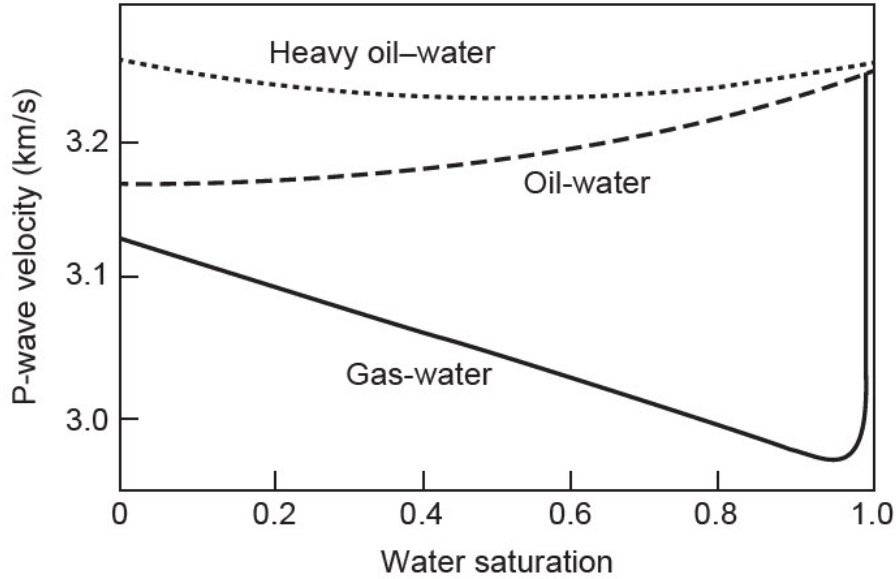


Figure 6.2: Gassman predictions for the P-wave velocity change for a heavy oil, oil, and gas initial fluid scenario where the replacement fluid is water. (from Johnston, 2013)

Table 6.1 contains information from ExxonMobil (2011); this table outlines the hydrocarbon fluid properties for the entire Hebron Field. The values in this table generate a fluid set within the RokDoc software containing the density, P-wave velocity, and bulk modulus for the hydrocarbons within the Pool 1 Reservoir (Table 6.2). These fluid properties represent Fluid A; this is the oil contained in Pool 1 pore space for the RokDoc fluid substitution process.

Description	Units	Pool 1
Reservoir Pressure	Mpa	19
Reservoir Temperature	°C	62
Gas-Oil Ratio (GOR)	Sm ³ /Sm ³	50
Stock Tank Oil Gravity	°API	17-24
Average Gas Gravity	(air = 1)	0.729

Table 6.1: Table indicating fluid parameters input into the RokDoc software to generate accurate fluid properties for the Pool 1 reservoir of the Hebron Field. This fluid information is from the Hebron Field development plan submitted to the CNLOPB for field development approval, thus represents the reservoir prior to production. (after ExxonMobil, 2011)

Description	Units	Pool 1
Water In-situ Density	kg/m ³	1032
Water Bulk Modulus	Mpa	2710
Water P-Wave Velocity	m/s	1637.98
Oil In-situ Density	kg/m ³	826
Oil Bulk Modulus	Mpa	1269
Oil P-Wave Velocity	m/s	1239.5

Table 6.2: Table showing fluid parameters calculated using RokDoc, which represents the oil contained in the Pool 1 pore space from the inputted parameters shown in Table 6.1.

6.1.2 Mineral Properties of the Pool 1 Reservoir

Similar to the fluid properties, determining the mineralogical framework of the Ben Nevis sandstone within the Pool 1 reservoir is also important to correctly predict the updated properties. X-ray diffraction (XRD) data for the Hebron M-04 and Hebron D-94 wells are averaged across the reservoir interval to determine the average mineralogical framework of the Ben Nevis reservoir within Pool 1 of the Hebron Field. Like the fluids data, the mineralogical breakdown is also input into the RokDoc software for use in the fluid substitution process as the K_s variable.

6.1.3 Model Based Well Logs Generated for the Fluid Substitution

The fluid substitution process acts as a pseudo-production simulation. As such, the majority of the wells undergoing the fluid substitution are oil producing wells drilled in Pool 1. The majority of the production wells in this thesis (both oil producing and water injecting) only contain a digitized density log, if any logs at all. The fluid substitution process within the RokDoc software requires density, porosity, P-

wave velocity, and S-wave velocity well logs for every well undergoing this calculation; other than the three exploration wells (Hebron I-13, Hebron D-94, and Hebron M-04) within the Pool 1 reservoir, these logs are not available to use in this thesis.

To account for this lack of well data, synthetic well logs are created along each well trace intersecting the Pool 1 reservoir from the density and porosity properties of the Pool 1 geological model and a P-wave velocity from the baseline full-field velocity model. A density model log, a porosity model log, and a P-wave velocity model log are created for every well intersecting the Pool 1 reservoir independent of whether any of these logs existed already. To generate an S-wave velocity model log, first, an S-wave velocity model is created using the Pool 1 geological model grid from the up-scaled S-wave velocity well log from the Hebron I-13, Hebron D-94, and Hebron M-04 wells; each well trace within the Pool 1 reservoir had a synthetic S-wave model log extracted from this S-wave velocity model. Figure 6.3 is an example model well log set containing the density model log, porosity model log, P-wave velocity model log, and S-wave velocity model log showcasing the well logs that are used for the log based fluid substitution.

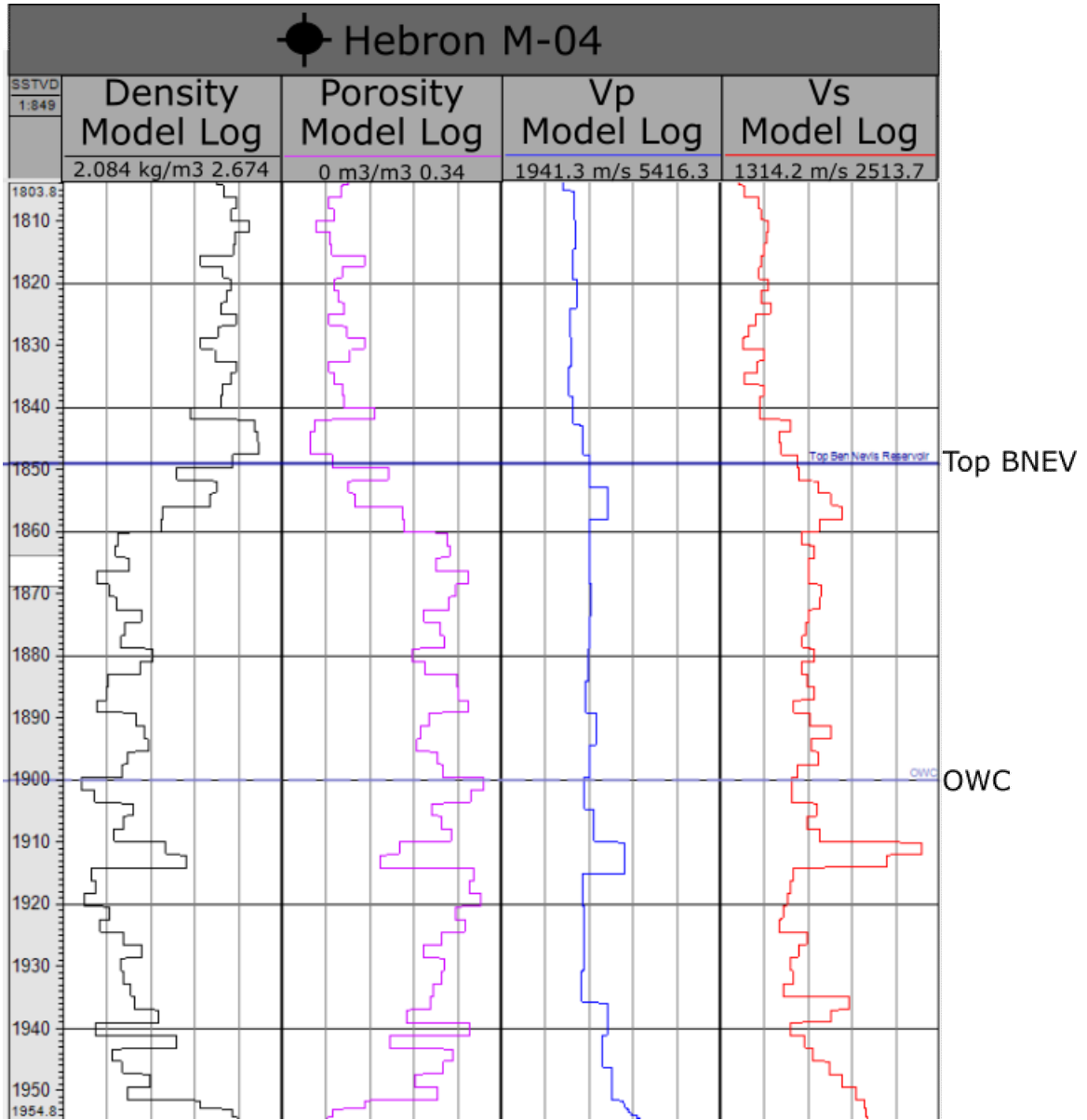


Figure 6.3: Example model well log set showing the density, porosity, P-wave, and S-wave model logs for the Hebron M-04 well used within the log based fluid substitution within the RokDoc software. The well data is displayed in true vertical depth (TVD), with Top BNEV indicating the top of the Ben Nevis sandstone and OWC is the oil-water contact.

6.1.4 Log Based Fluid Substitution Results

For each well in the Pool 1 reservoir, a range of fluid substitution scenarios are simulated ranging from 100% oil to 100% water to create a range of diverse production

scenarios for the perturbed monitor velocity model of the Hebron Field. The Pool 1 reservoir of the Hebron field is considered to not contain a gas cap and has an oil-water contact (OWC) at 1900 m true vertical depth subsea (TVDSS) (ExxonMobil, 2011). This is important information for the fluid substitution work as it allows the initial fluids to be set at 100% oil when the fluid substitution working interval is set from the top of the Ben Nevis sandstone to either the OWC (if crossed by the well trace) or to the bottom of the well (deviated horizontal production wells which do not cross the OWC).

Figure 6.4 is the fluid substitution for the Hebron L-93 7 well. To showcase how the P-wave velocity changes with increasing water saturation, only the 100% oil (black), 50-50 oil-water (blue), and 100% water (red) scenarios are displayed; a 10% change increment in water saturation is calculated for each well beginning at 100% oil to 100% water.

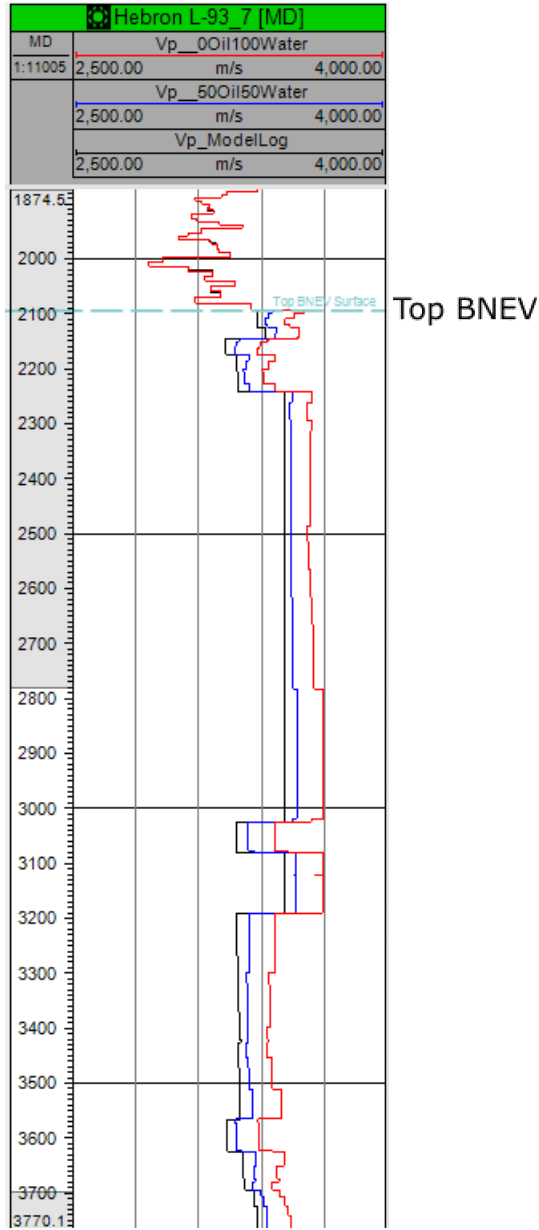


Figure 6.4: Hebron L-93 7 well log showcasing the fluid substitution process updating the P-wave model log from 100% oil (black) to 50-50 oil-water (blue) to 100% water (red). The well log is shown in measured depth along the wellbore.

The general trend in Figure 6.4 highlights that for the Pool 1 wells, as the water saturation increases, the P-wave velocity of the rock also increases, as expected based on Figure 6.2 and the input fluid parameters. It is also important to point out that above the "Top BNEV" line (Figure 6.4), there is only one well log. This is because

the log values start at the initial well P-wave velocity model log (shown as a single red line as all three curves are the same) or the 100% oil case (i.e. baseline model velocity) above the fluid substitution zone. This indicates that only the reservoir section of the well log is being perturbed; thus, for the monitor model, the velocity change should be limited to the reservoir section.

6.2 Fluid Substitution Based Monitor Model

The monitor model for this project is focused on a velocity perturbation by simulating a waterflood of the main fault block (Hebron Fault Block seen in Figure 2.6) of the Pool 1 reservoir within the Hebron Field. This fault block, based on available wells drilled to the date of data collection (November 26, 2019), is being produced by three water injector wells and eight oil producing wells (Figure 2.8). To simulate the production of this reservoir, these eleven production wells and their surrounding exploration wells (Hebron M-04 and Hebron D-94) within the Hebron block of the Pool 1 reservoir are assigned updated velocities based on their well classification and locations (Table 6.3).

Water injector wells (Hebron L-93 5, Hebron L-93 8, and Hebron L-93 11) are assigned a P-wave velocity from the 60% oil 40% water fluid substitution scenario as the estimated recovery factor (RF) of the Hebron Fault block is 40% (ExxonMobil, 2011). Hebron M-04 is also assigned this same P-wave velocity as it is located in close proximity to the Hebron L-93 5 and Hebron L-93 11 water injector wells. Oil producing wells and Hebron D-94 are assigned a P-wave velocity of 80% oil 20% water to simulate a mid-life-cycle production stage of the reservoir. Wells located only within the Hebron fault block are assigned a velocity change to attempt to confine the velocity perturbation to the Ben Nevis sandstone interval within the Hebron fault block.

Well	Well Classification	P-Wave Velocity Used
Avondale A-46	Exploration	Baseline Velocity
Ben Nevis I-45	Exploration	Baseline Velocity
Ben Nevis L-55	Exploration	Baseline Velocity
Brent's Cove I-30	Exploration	Baseline Velocity
Cape Race N-68	Exploration	Baseline Velocity
Hebron D-94	Exploration	80% Oil 20% Water
Hebron I-13	Exploration	Baseline Velocity
Hebron L-93 10	Oil Producer	80% Oil 20% Water
Hebron L-93 11	Water Injector	60% Oil 40% Water
Hebron L-93 12	Oil Producer	80% Oil 20% Water
Hebron L-93 13	Oil Producer	80% Oil 20% Water
Hebron L-93 2	Oil Producer	80% Oil 20% Water
Hebron L-93 3	Oil Producer	80% Oil 20% Water
Hebron L-93 4Z	Oil Producer	80% Oil 20% Water
Hebron L-93 5	Water Injector	60% Oil 40% Water
Hebron L-93 6	Oil Producer	80% Oil 20% Water
Hebron L-93 7	Oil Producer	80% Oil 20% Water
Hebron L-93 8	Water Injector	60% Oil 40% Water
Hebron L-93 9	Oil Producer	80% Oil 20% Water
Hebron M-04	Exploration	60% Oil 40% Water
North Trinity H-71	Exploration	Baseline Velocity
West Ben Nevis B-75	Exploration	Baseline Velocity
West Bonne Bay C-23	Exploration	Baseline Velocity
West Bonne Bay F-12	Exploration	Baseline Velocity
West Bonne Bay F-12Z	Exploration	Baseline Velocity

Table 6.3: P-wave velocity fluid substitution scenarios used for each well for the perturbed monitor velocity model.

Using these updated velocity logs and following the same procedure outlined in the previous chapter (Chapter 5), we produce the monitor model shown in Figure 6.5.

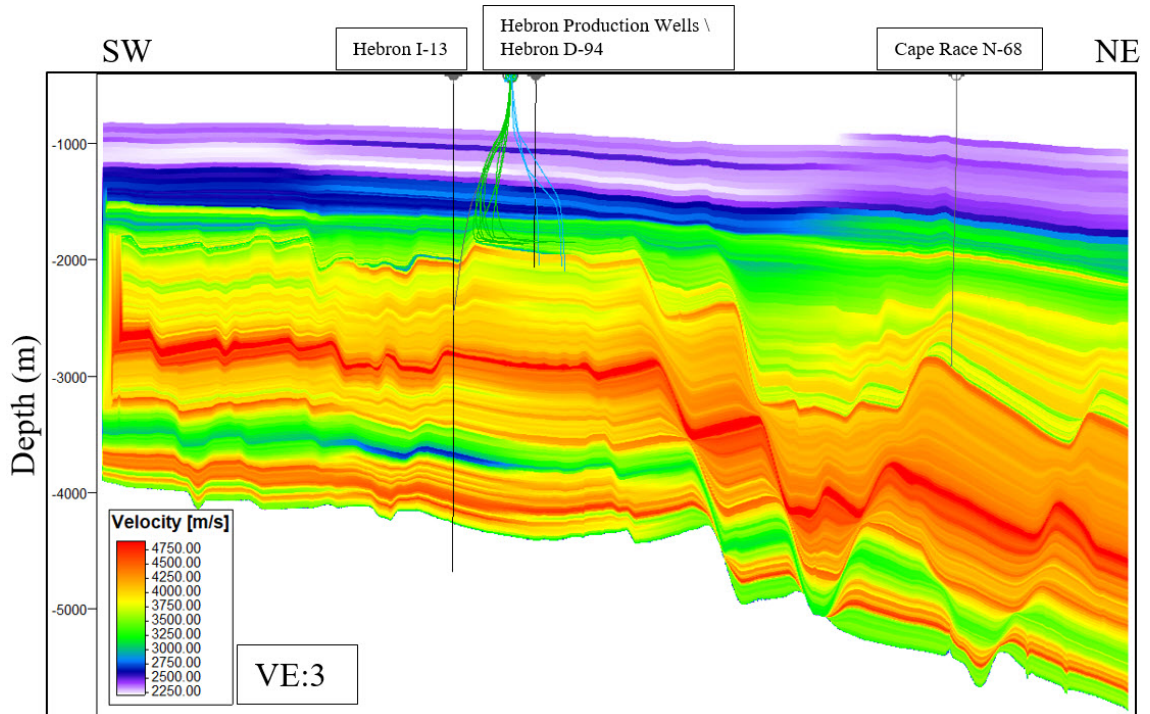


Figure 6.5: Monitor velocity model created using the fluid substituted log data along IL 9281.

The residual between the baseline velocity model and the monitor model along IL 9281 is shown in Figure 6.6. The velocity change extends from the Hebron fault block (block with multiple well penetrations) to the surrounding fault blocks which were not perturbed by fluid substitution. This is because the velocity data are extrapolated between wells within horizon zones in the modeling process used in this project. The map view of the residual is in Figure 6.7, where it shows that the velocity perturbation is the strongest within and surrounding the Hebron fault block but spreads throughout a large portion of the northern section of the Hebron field.

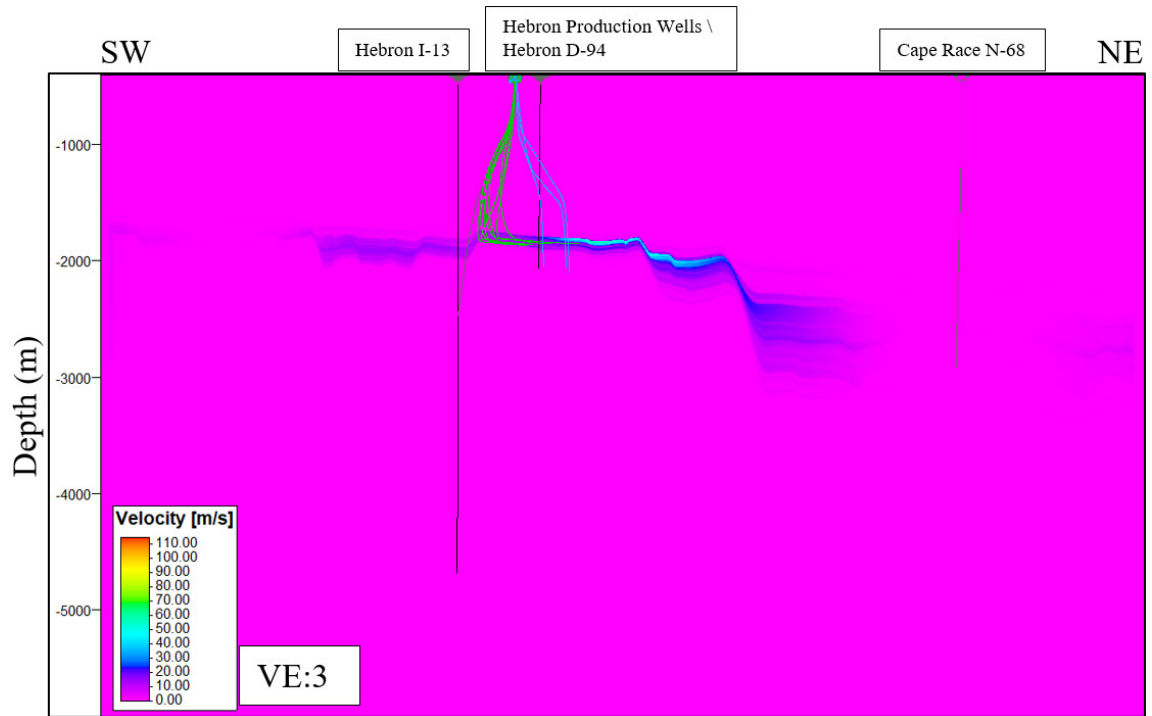


Figure 6.6: Residual between the baseline velocity model and monitor velocity model created using the fluid substituted log data along IL 9281.

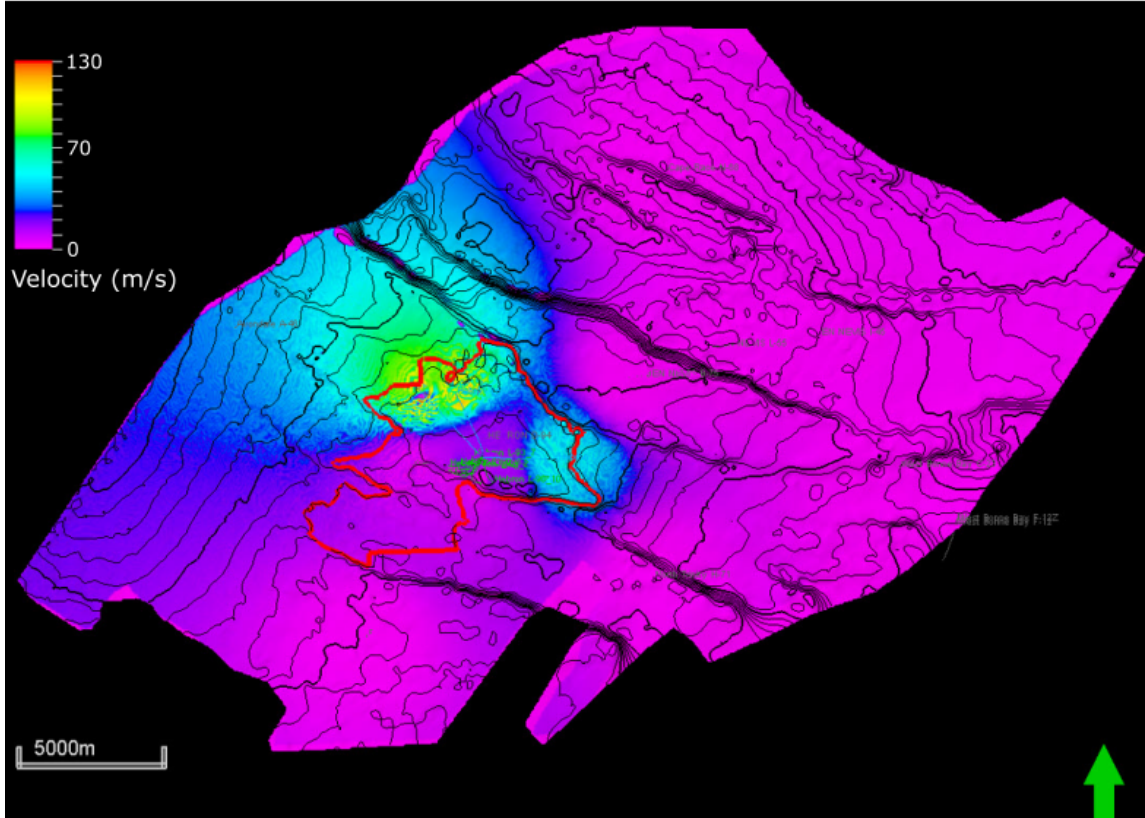


Figure 6.7: Residual between the baseline velocity model and monitor velocity model shown in a 3D map view, the red polygon represents the Pool 1 geological model boundary and the green arrow points northward.

To prevent this extrapolation, we create anchor wells surrounding the Hebron fault block and along the IL 9281 seismic line to contain the velocity perturbation to only the Hebron fault block. These anchor wells are displayed in Figure 6.8; these are prescribed as straight vertical wells intersecting the model with velocity logs directly from the baseline velocity model, creating anchor points to contain the change within the monitor model. The perturbation is required to be constrained within this fault block because of how the local domain 4D seismic uncertainty quantification algorithm used in the following chapter calculates the 4D seismic response. Constraining this velocity change to only the Hebron fault block assumes that there is no communication between the Ben Nevis reservoir within this fault block and the reservoir intervals

within the surrounding fault blocks (I-13 and West Ben Nevis fault blocks).

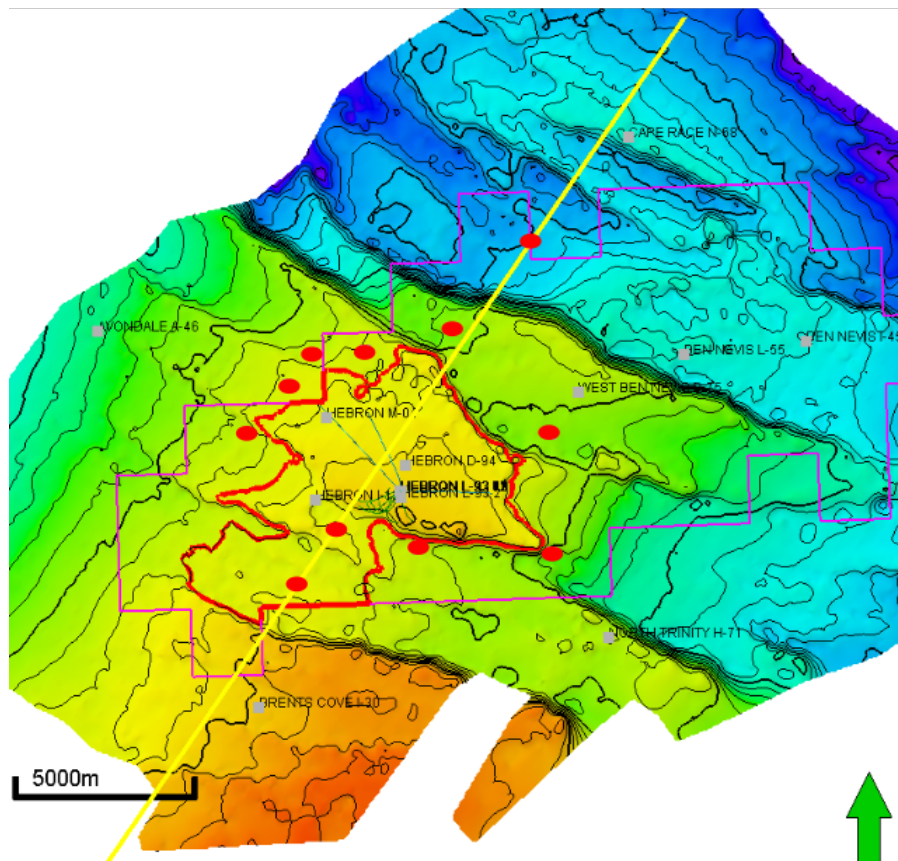


Figure 6.8: Anchor Well locations (red circles) surrounding the Hebron fault block of the Pool 1 reservoir (red polygon) and along the IL 9281 (yellow line) overlain on the top Ben Nevis reservoir 3D seismic surface, the green arrow points northward.

The residual between the monitor and baseline models after the addition of the anchor wells is in Figure 6.9, with these anchor wells constraining the velocity perturbation to the Hebron fault block along the IL 9281 seismic line. Examining this velocity perturbation in a 3D map view (Figure 6.10) shows that the velocity perturbation still bleeds to the north but now at a negligible magnitude.

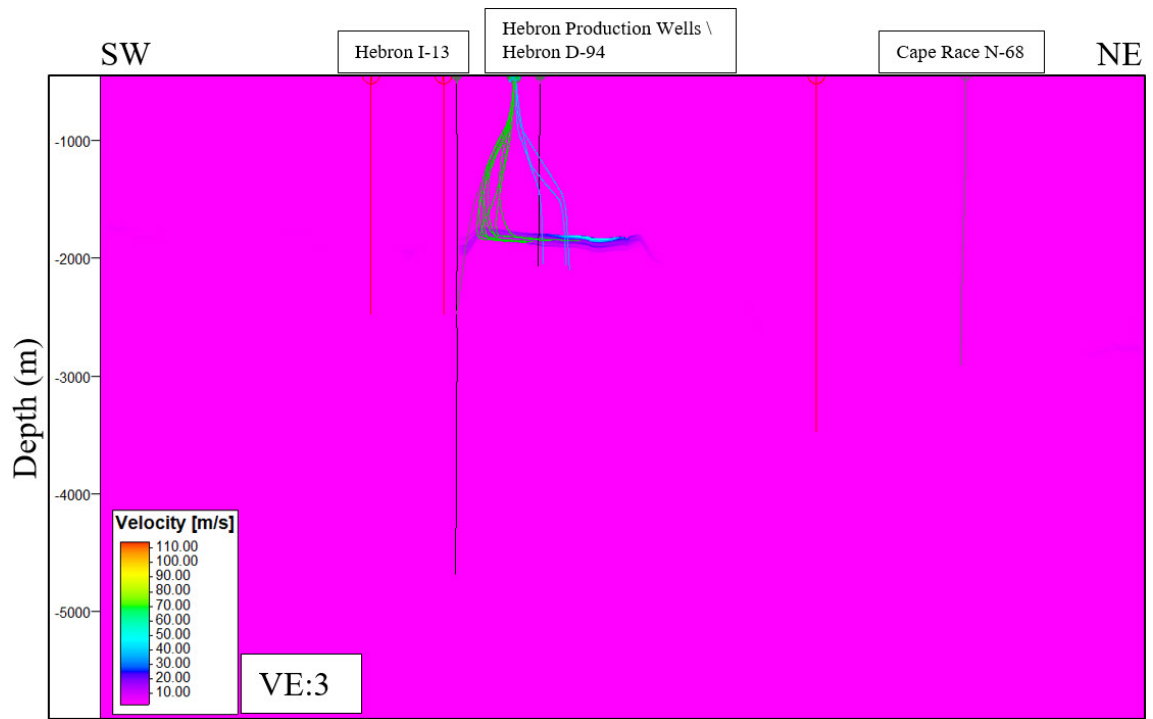


Figure 6.9: Residual between the baseline velocity model and monitor velocity model created using the fluid substituted log data along IL 9281; additional anchor wells shown as the vertical red lines.

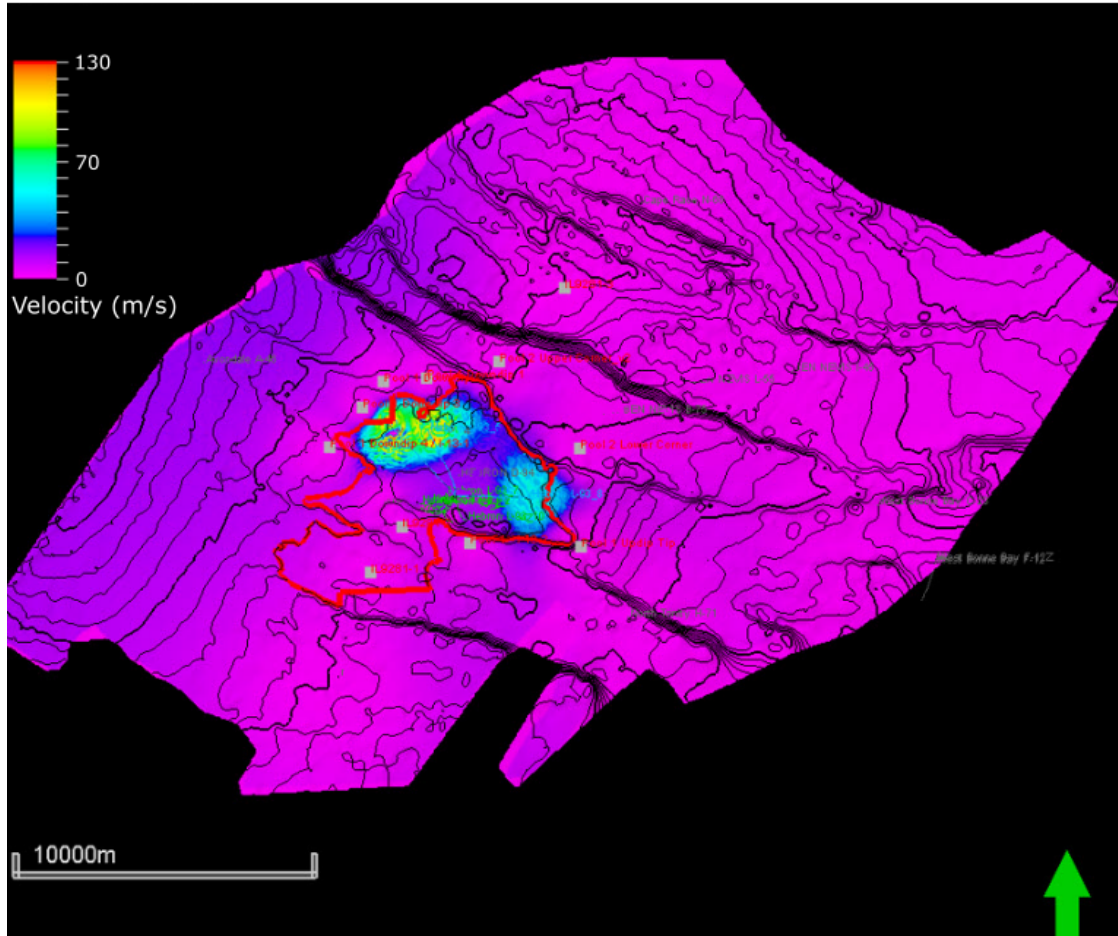


Figure 6.10: Residual between the baseline velocity model and monitor velocity model shown in a 3D map view. Compared to Figure 6.7, the residual velocity change stays within the Pool 1 polygon. Anchor Well locations (grey squares) surrounding the Hebron fault block of the Pool 1 reservoir (red polygon) and the green arrow points northward.

Chapter 7

Time-lapse Seismic Uncertainty Quantification

In this thesis, we use a 4D multi-parameter Metropolis-Hastings seismic uncertainty algorithm introduced by Kotsi et al. (2020), which utilizes a local domain solver. We apply this uncertainty quantification algorithm to both the baseline and monitor velocity models created over the last two chapters to study the uncertainty in the estimates of the synthetic velocity change caused by the production of the Pool 1 reservoir.

7.1 4D Multi-Parameter Metropolis-Hastings Seismic Uncertainty Quantification Algorithm

The 4D multi-parameter seismic uncertainty quantification algorithm used in this thesis is a local domain Bayesian seismic inversion-based algorithm that turns the traditional FWI optimization problem into a sampling problem utilizing a Markov Chain Monte Carlo (MCMC) method (Kotsi et al., 2020). The algorithm exploits

the nature of the 4D seismic problem to use a local domain solver to split velocity models into a local domain and exterior to compute potential velocity perturbations at a much faster rate (Kotsi et al., 2020; Willemsen et al., 2016). In the time-lapse seismic scenario, this local domain is defined over areas of production (i.e. Pool 1) as this is the only portion of the baseline/monitor models that is assumed to change. The MCMC method samples thousands of models to explore a predefined probability space until an equilibrium state is reached (Figure 7.1); at which point this probability space is equal to the posterior probability distribution of the parameters given the observed data (see Kotsi et al., 2020 and references therein).

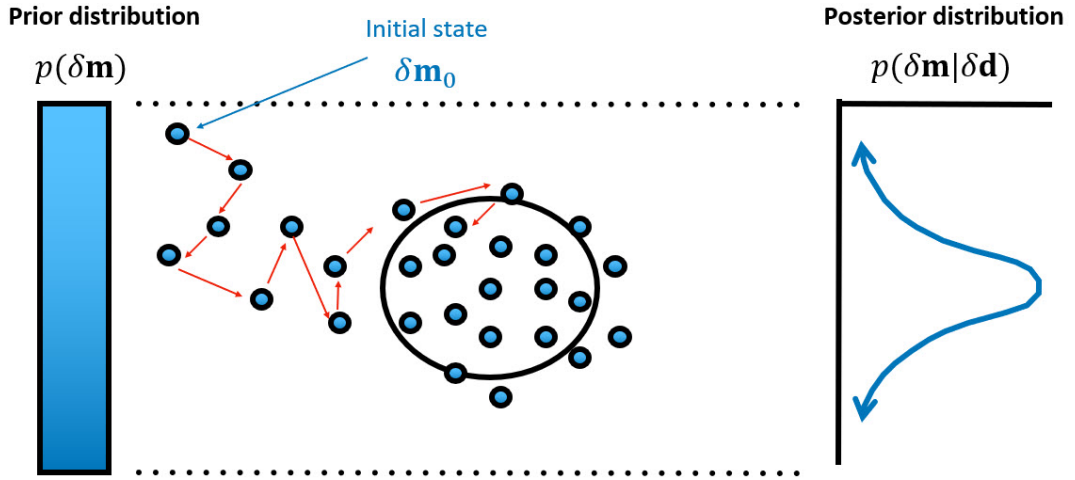


Figure 7.1: Illustration of the Markov Chain Monte Carlo method. (from Kotsi, 2020)

7.1.1 Algorithm Breakdown

Kotsi (2020) describes the uncertainty quantification algorithm used in this thesis in detail; we will summarize this explanation over the following sections. For a more detailed breakdown, we refer readers to Kotsi (2020).

Using Bayes' Theorem in seismic imaging, we can relate our subsurface velocity model (m) to our observed data (d) (Kotsi, 2020). This relationship is,

$$p(m|d) = \frac{p(d|m)p(m)}{p(d)} \quad (7.1)$$

where $p(m|d)$ is the probability of observing a given velocity model, m , given some observed data, d , and where $p(d|m)$ is the likelihood function, which measures the probability of observing a given dataset, d , when the underlying model is m (Kotsi, 2020). $p(m|d)$ is the posterior probability and is the quantity of interest in any probabilistic based inversion process; it gives the probability of the model given the observed data d . For the posterior calculation to be accurate, a large number of samples (hundreds of thousands) are needed so that the first half can be discarded to reduce the effect of the starting model and for the MCMC to still reach equilibrium (Kotsi, 2020; Brooks et al., 2011).

Since thousands of samples and therefore thousands of wavefield solves are needed for the MCMC to reach an equilibrium state, a local acoustic solver is implemented to take advantage of the 4D seismic problem (Kotsi, 2020). This wavefield solver was developed by Willemsen et al. (2016) and is used to calculate the wavefield in the defined local domain for each proposed model. For a 4D seismic study, it is assumed that only the area of the model with a fluid change (i.e. reservoir section) should have a velocity change. This allows the full domain wavefield to be calculated only once before initiating the sampling procedure, with repeated calculations occurring only within the local domain, thus decreasing the computation cost.

This inversion code uses a specific MCMC method, called the Adaptive Metropolis-Hastings method. This is a version of a Metropolis-Hastings method which does not

require the $p(d)$, lowering the computational cost as this is the hardest quantity to compute (Kotsi, 2020; Ely et al., 2018). The pseudocode for this 4D seismic algorithm is shown in Figure 7.2. Following Kotsi (2020), over the following paragraphs, we explain these steps.

```

Require:  $\delta \mathbf{m}_0$                                 ▷ initial perturbation
Require:  $C_0$                                     ▷ initial step size
Require:  $N$                                        ▷ maximum number of iterations
Require:  $N_c$                                     ▷ number of iterations before the updating starts
Require:  $d = \text{length}(\delta \mathbf{m}_0, \dots, \delta \mathbf{m}_{i-1})$ 
Require:  $S_d = \frac{2.4^2}{d}$                                 ▷ value from
Require:  $\epsilon \ll 1$                                 Haario et al., 2001
     $L(\delta \mathbf{m}_0)$ 
2: for  $i = 1, \dots, N$  do
    if  $i < N_c$  then
4:      $C_i = C_0$                                 ▷ fixed step size
    else
6:      $C_i = S_d(\text{Cov}[\delta \mathbf{m}_0, \dots, \delta \mathbf{m}_{i-1}] + \epsilon \mathbf{I}_d)$ , ▷ tune step size based on covariance
        of models
    end if
8:      $n \leftarrow \text{Normal}(0, C_i)$                 ▷ proposed jump
         $\delta m_* \leftarrow \delta m_{i-1} + n$           ▷ proposed model perturbation
10:     $L(\delta m_*)$                                 ▷ get the likelihood of the proposal
         $\alpha_i = \frac{L(\delta m_*)}{L(\delta m_{i-1})}$         ▷ acceptance probability
12:     $u \leftarrow U[0, 1]$                         ▷ uniform distribution
        if  $u < \alpha_i$  then
14:         $\delta m_i \leftarrow \delta m_*$                 ▷ accept proposal
        else
16:         $\delta m_i \leftarrow \delta m_{i-1}$             ▷ reject proposal
        end if
18: end for

```

Figure 7.2: The pseudocode showing the steps of the Adaptive Metropolis Hastings algorithm used for the 4D seismic inversion. (modified from Kotsi, 2020)

To begin, in the inverse problem the data can be described by,

$$d = G(m) + n, \tag{7.2}$$

where G is forward model wavefield solver, m is the velocity model, and n is zero mean Gaussian noise with a covariance matrix Σ ; extending this to the 4D case, the monitor survey is,

$$d_1 = G(m_1) + n_1 \quad (7.3)$$

and the baseline survey is,

$$d_0 = G(m_0) + n_0. \quad (7.4)$$

The time-lapse change between m_1 and m_0 can be represented as

$$\delta m = m_1 - m_0 \quad (7.5)$$

and similarly, the data residual between the two models can be represented as

$$\delta d = d_1 - d_0. \quad (7.6)$$

Plugging Equations 7.3 and 7.4 into Equation 7.6,

$$\begin{aligned} \delta d &= G(m_1) + n_1 - G(m_0) - n_0 \\ &= G(m_1) - G(m_0) + (n_1 - n_0) \\ &= G(\delta m + m_0) - G(m_0) + (n_1 - n_0) \end{aligned} \quad (7.7)$$

Since, n_1 and n_0 are both zero mean Gaussian noise, they can be combined to make one Gaussian, n_2 , with a covariance matrix $\Sigma_2 = \Sigma_1 + \Sigma_0$. Inputting this into Equation 7.7 it becomes

$$\delta d = F(m_0, \delta m) + n_2 \quad (7.8)$$

where $F(m_0, \delta m)$ is equal to $G(\delta m + m_0) - G(m_0)$. To get δd in terms of just δm in Equation 7.8 we first need to examine the model perturbation. If it is assumed that $F(m_0, \delta m)$ is independent of the baseline model, m_0 , then

$$F(m_{0a}, \delta m) = F(m_{0b}, \delta m) \quad (7.9)$$

as when the perturbation to m_0 is small $m_{0a} \approx m_{0b}$.

Since, in 4D seismic studies, we are comparing two surveys over the same area with a perturbation expected within our defined local domain (i.e reservoir target), any other perturbations not explained by the data should cancel out between the surveys. δd should therefore contain only the expected time-lapse change (caused by the change in the model δm) defined within the local domain. Therefore, Equation 7.8 can be written as

$$\delta d = F(\delta m) + n_2 \quad (7.10)$$

and then Bayes' theorem in Equation 7.1 can also be written as

$$p(\delta m|\delta d) = \frac{p(\delta d|\delta m)p(\delta m)}{p(\delta d)} \quad (7.11)$$

with the likelihood function, $p(\delta d|\delta m)$, being

$$\begin{aligned} \mathcal{L}(\delta m) \equiv p(\delta d|\delta m) \propto \\ \exp \left[-\frac{1}{2}(F(\delta m) - \delta d)^T \Sigma_3^{-1} (F(\delta m) - \delta d) \right]. \end{aligned} \quad (7.12)$$

Looking back at Figure 7.2, the algorithm runs with a fixed step size, C_0 , for a set number of iterations, N_c . Kotsi (2020) defines N_c to be 1000 as this leads to a good convergence; as such, we compute the algorithm following the same procedure. After

this set number of iterations, an adaptive step is implemented. This step size is calculated from

$$C_i = S_d (\text{Cov}[\delta m_0, \dots, \delta m_{i-1}] + \epsilon I_d) \quad (7.13)$$

where S_d is assumed to be $\frac{2.4^2}{d}$ (Haario et al., 2001), where d is the number of parameters of the model, I_d is the identity matrix, and ϵ is assumed to be 1×10^{-10} (Haario et al., 2001). For each iteration, i , a new perturbation, δm_* , is proposed by adding a zero mean perturbation to the current perturbation (δm_{i-1}). This zero mean perturbation is drawn from the covariance (Equation 7.13). This new perturbation is then either accepted or rejected based on the ratio of likelihood functions,

$$\alpha_i = \frac{\mathcal{L}(\delta m_*)}{\mathcal{L}(\delta m_{i-1})}. \quad (7.14)$$

The acceptance probability for Metropolis Hastings algorithms is defined as

$$\alpha = p(\delta m_* | \delta m_{i-1}) = \min \left[1, \frac{p(\delta m_*) p(\delta d | \delta m_*) Q(\delta m_{i-1} | \delta m_*)}{p(\delta m_{i-1}) p(\delta d | \delta m_{i-1}) Q(\delta m_* | \delta m_{i-1})} \right] \quad (7.15)$$

where Q is the transition kernel which is a means of jumping to the next perturbation by using the previous perturbation. If a perturbation is accepted, then the proposal becomes the new guess. If it gets rejected, the current guess stays the same and the process repeats.

7.1.2 Degrees of Freedom

Adaptive Metropolis-Hasting algorithms can perform well for up to 200 parameters or degrees of freedom (DoF) (Kotsi, 2020; Haario et al., 2001). Ely et al. (2018) determined that for seismic imaging, only up to 41 DoFs can be used for these algorithms to perform effectively. Even with the local domain approach used by Kotsi (2020), we

need to solve for $Nx_{sub} * Nz_{sub}$ DoFs, where the size of the local domain is Nx_{sub} by Nz_{sub} . To put this in context, the size of the local domain we define in this thesis to represent the Pool 1 reservoir of the Hebron Field is 139 by 45, meaning there would be a total of 6255 DoFs to solve for, which is much larger than the maximum number of DoFs (41). To rectify this, there are many different basis functions we can use to represent our data with fewer DoFs to allow the algorithm to work effectively. Kotsi (2020) utilizes Discrete Cosine Transform (DCT) to compress the velocity model as an image to lower the number of DoFs required to represent the model in the local domain.

The DCT method decomposes a given data set into an orthogonal cosine basis. It is selected by Kotsi (2020) due to the high energy compaction efficiency through the ability to concentrate the majority of the decompressed data into a few frequency coefficients (i.e fewer DoFs are needed to represent the model within the local domain) (Kotsi, 2020). These DCT coefficients for a 2D m by n matrix where $m = Nz_{sub}$ and $n = Nx_{sub}$ for the k_{th} and l_{th} degree are defined as

$$DCT_{kl} = \vec{\alpha}_k \vec{\alpha}_l \sum_{m=0}^{M-1} \sum_{n=0}^{N-1} \frac{\cos \pi(2m+1)k \cos \pi(2n+1)l}{2M2N} \quad (7.16)$$

where

$$\vec{\alpha}_k = \begin{cases} \frac{1}{\sqrt{M}}, k = 0 \\ \sqrt{\frac{2}{M}}, 1 \leq k \leq M - 1 \end{cases} \quad (7.17)$$

and

$$\vec{\alpha}_l = \begin{cases} \frac{1}{\sqrt{N}}, l = 0 \\ \sqrt{\frac{2}{N}}, 1 \leq l \leq N - 1 \end{cases} \quad (7.18)$$

α_k and α_l are normalizing constants. Each component of the DCT matrix is normalized to ensure that they contain the same energy. This is done using

$$DCT_{kl} = \frac{DCT_{kl}}{\|D\vec{C}T_{kl}\|}. \quad (7.19)$$

The number of DCT matrices is determined by the size of the local domain, where the number of matrices is equal to $m * n$. Each of these matrices is stored within a single matrix, Φ , with the time-lapse change, δm , being

$$\delta m = \vec{\alpha}\Phi, \quad (7.20)$$

with regards to the DCT transformation where,

$$\Phi = [DCT_1(\cdot)DCT_2(\cdot)\dots DCT_{m*n}(\cdot)]. \quad (7.21)$$

Each column of the Φ matrix is a vectorized DCT matrix, thus the Φ matrix is an orthogonal matrix.

To solve for the time-lapse change at each iteration, an inverse problem is setup to recover the $\vec{\alpha}$ coefficients, where at each iteration of the MCMC algorithm, we use a new set of alpha coefficients to compute δm ; this proposed time-lapse change is either accepted or rejected based on the likelihood function (7.12) (Kotsi, 2020). The Φ matrix is low-rank as illustrated by the fact that the singular values decay quickly, as highlighted in Figure 7.3. A singular value decomposition (SVD) is completed using only the largest singular values of the Φ matrix; these largest singular values are determined based on the drop-off seen in Figure 7.3 b, where in this case the SVD is computed on the first 300 largest singular values (Kotsi, 2020).

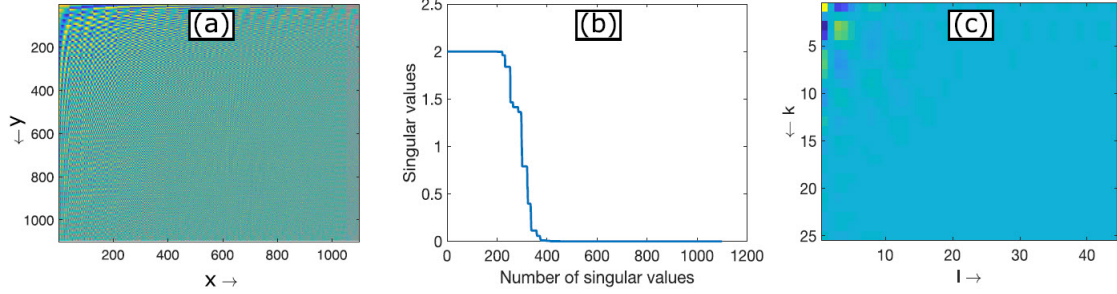


Figure 7.3: a) Example Φ matrix b) Singular values of the example Φ matrix which decay after the first 300 values. c) $\vec{\alpha}$ coefficients (From Kotsi et al., 2020)

Figure 7.4 is an example time-lapse change reconstruction anomaly using 300 $\vec{\alpha}$ coefficients; these $\vec{\alpha}$ coefficients are the largest 300 singular values of the Φ matrix as indicated by Figure 7.3 b. In this example, the algorithm would need to recover 300 $\vec{\alpha}$ coefficients, which is much larger than the maximum number of DoFs (41 DoFs) able to be recovered; thus, to reduce the number of required DoFs, a subset of the $\vec{\alpha}$ coefficients are selected. Figure 7.4 c, highlights the efficiency of the DCT compaction method as the majority of the $\vec{\alpha}$ coefficients are concentrated in the top left corner; these are the essential coefficients needed to reconstruct the time-lapse change (Kotsi, 2020).

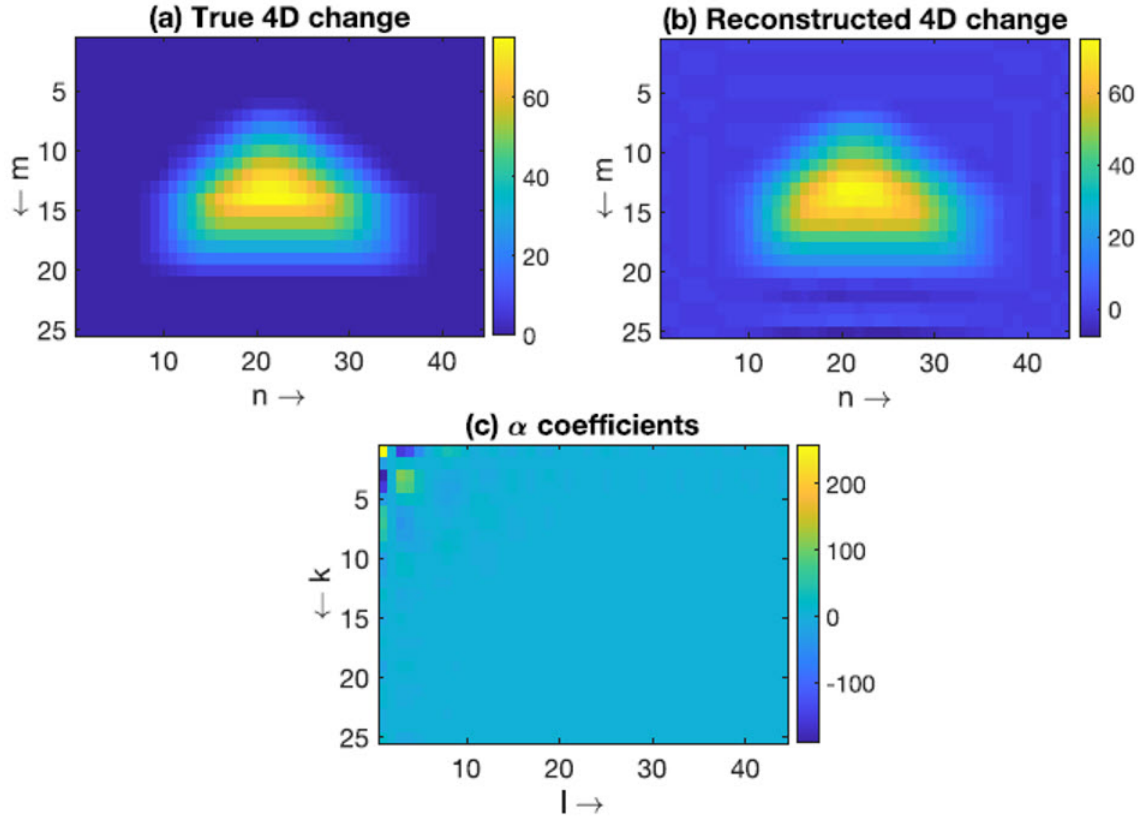


Figure 7.4: a) Example true smoothed time-lapse change b) reconstruction of the example time-lapse change using 300 $\vec{\alpha}$ coefficients c) $\vec{\alpha}$ coefficients (From Kotsi, 2020)

When interpreting the results of the MCMC algorithm, Kotsi (2020) elects to analyze the convergence and quality of the results directly through the recovered $\vec{\alpha}$ coefficients over the obtained reconstructed image (Kotsi, 2020). We use a similar philosophy in the subsequent section (Section 7.2) to interpret the results; however, we also plot the reconstructed image of the local domain for statistical measures to incorporate a visual interpretation of the recovered velocity estimates.

7.2 4D Seismic Uncertainty Quantification Analysis of the Hebron Field Pool 1

To apply this algorithm to the monitor and baseline models generated within the Petrel software discussed in the previous chapters, we first import the models into MATLAB. We do this by saving a 2D cross-section along IL 9281 for both the baseline and monitor models as a SEG-Y file; using a MATLAB add-on called SeisLab 3.02, the SEG-Y data for each model are saved as a matrix. Using these two matrices, a data difference matrix is calculated, representing the time-lapse velocity change for the Hebron Field. For computation reasons, we truncate these matrices (baseline, monitor, and data difference), removing the edges of the velocity model. Since we only compute the uncertainty in a local domain defined over the Pool 1 area, this has no effect on the results. Following this truncation, we smooth the data difference anomaly using a MATLAB function called `smooth2a` to remove hard edges of the anomaly to avoid artifacts (Kotsi et al., 2020). Shown in Figure 7.5 is the smoothed Hebron Field anomaly created over the last few Chapters highlighting the local domain used.

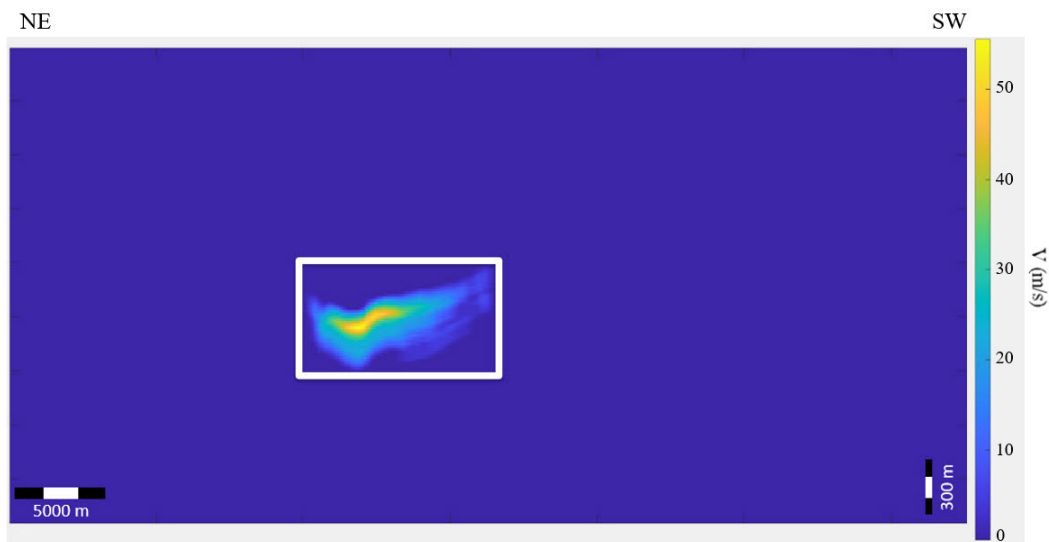


Figure 7.5: Smoothed Hebron Field Pool 1 anomaly with the local domain (white box) highlighted showing the area used in the uncertainty quantification algorithm.

7.2.1 Degree of Freedom Representations of the Pool 1 Anomaly

To determine the number of DoFs ($\vec{\alpha}$ coefficients) that accurately and efficiently represent the Pool 1 anomaly, we compare multiple representations. Shown in Figure 7.6, are the Φ matrix, singular values of the Φ matrix, and the $\vec{\alpha}$ coefficients of the Pool 1 anomaly. Similar to Figure 7.4, we see that for this anomaly, the values decay after 1400 singular values, thus to create the best possible reconstruction, we require a minimum of 1400 DoFs. Since we are limited to a maximum of 41 DoFs, we must select a subset of these $\vec{\alpha}$ coefficients to represent the anomaly. In Figure 7.6 c, we see that the energy is compacted to the upper left corner; thus, subsets of $\vec{\alpha}$ coefficients from this top left corner are examined.

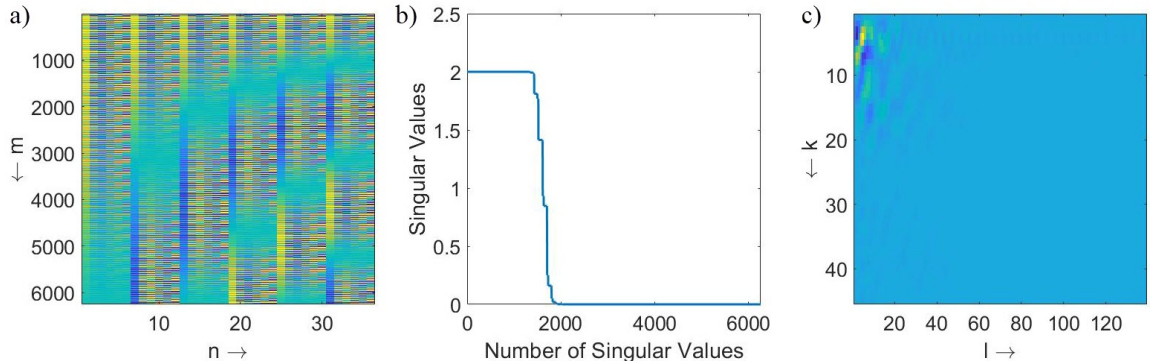


Figure 7.6: a) Pool 1 Φ matrix b) Singular values of the Pool 1 Φ matrix which decay after the first 1400 values. c) $\vec{\alpha}$ coefficients.

Specifically we compare 16 (4x4 square), 25 (5x5 square), and 36 (6x6 square) DoF representations back to the full $\vec{\alpha}$ coefficient reconstruction to determine the lowest number of DoFs that can represent the Pool 1 model accurately (Figure 7.7). The 6x6 (36 DoF) representation of the Pool 1 velocity anomaly is selected to represent the model as we advance within the uncertainty algorithm, as it best depicts the dipping nature of the deeper velocity anomaly extending up-dip to a slight velocity high.

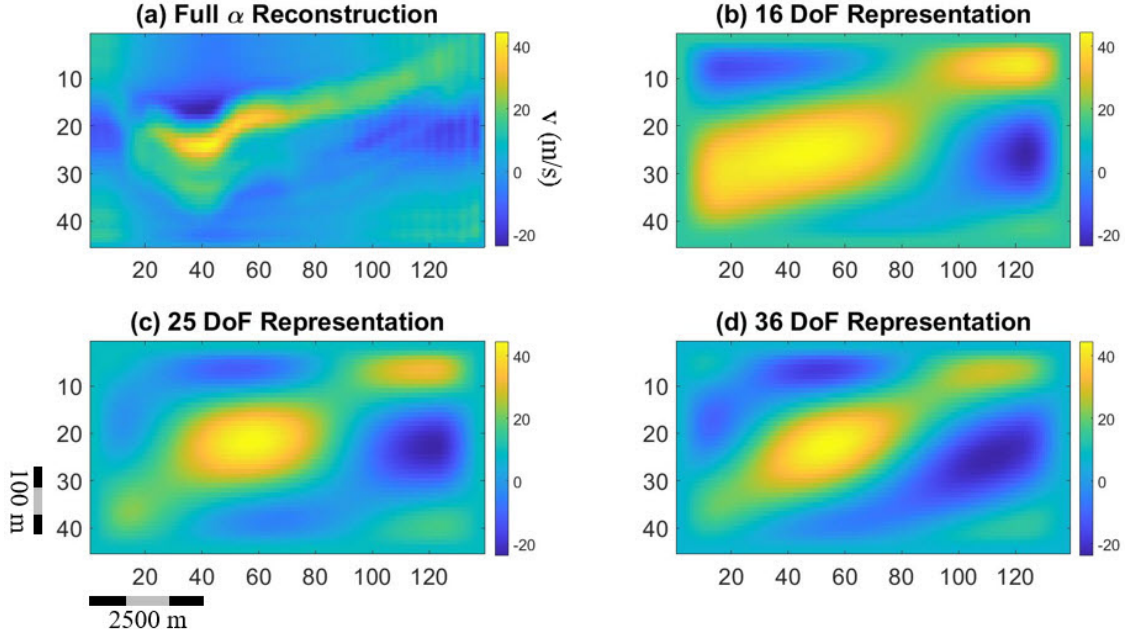


Figure 7.7: a) Reconstruction of the Pool 1 anomaly (Figure 7.5) using the entire alpha matrix (6255 DoF) b) 16 DoF representation c) 25 DoF representation d) 36 DoF representation. The plot area is the local domain which represents a 2D cross-section view of the Hebron fault block.

7.2.2 Time-Lapse Seismic Uncertainty Quantification Results for the Hebron Field

We compute four different Markov Chains at 100,000 iterations per chain (400,000 potential time-lapse seismic changes) for Pool 1 of the Hebron Field, these chains are computed in parallel at 8 Hz in approximately 35 hours on a standard desktop (i7-6700 3.40 GHz processor and 16 GB memory) at an acceptance rate of 18.0 - 21.5%. We choose to compute the local domain data at 8 Hz, as it is a reasonable mid-frequency for FWI experiments. The histograms of the recovered $\vec{\alpha}$ coefficients from the four chains are shown in Figure 7.8; the first half of the iterations are discarded to drop any dependency on the starting model (Figure 7.1). Very few histograms are the same across all four chains indicating that the algorithm has not converged. Likewise, we see that very few of these histograms across all four chains for each of the 36

$\bar{\alpha}$ coefficients have a mean in the confidence interval of the true value (green line); therefore, the algorithm is not approaching the correct model for the Pool 1 anomaly (Kotsi et al., 2020). We assume that this is related to the number of iterations we use and the number of DoFs selected; therefore, for the algorithm to converge, we must either increase the number of iterations and/or decrease the number of DoFs.

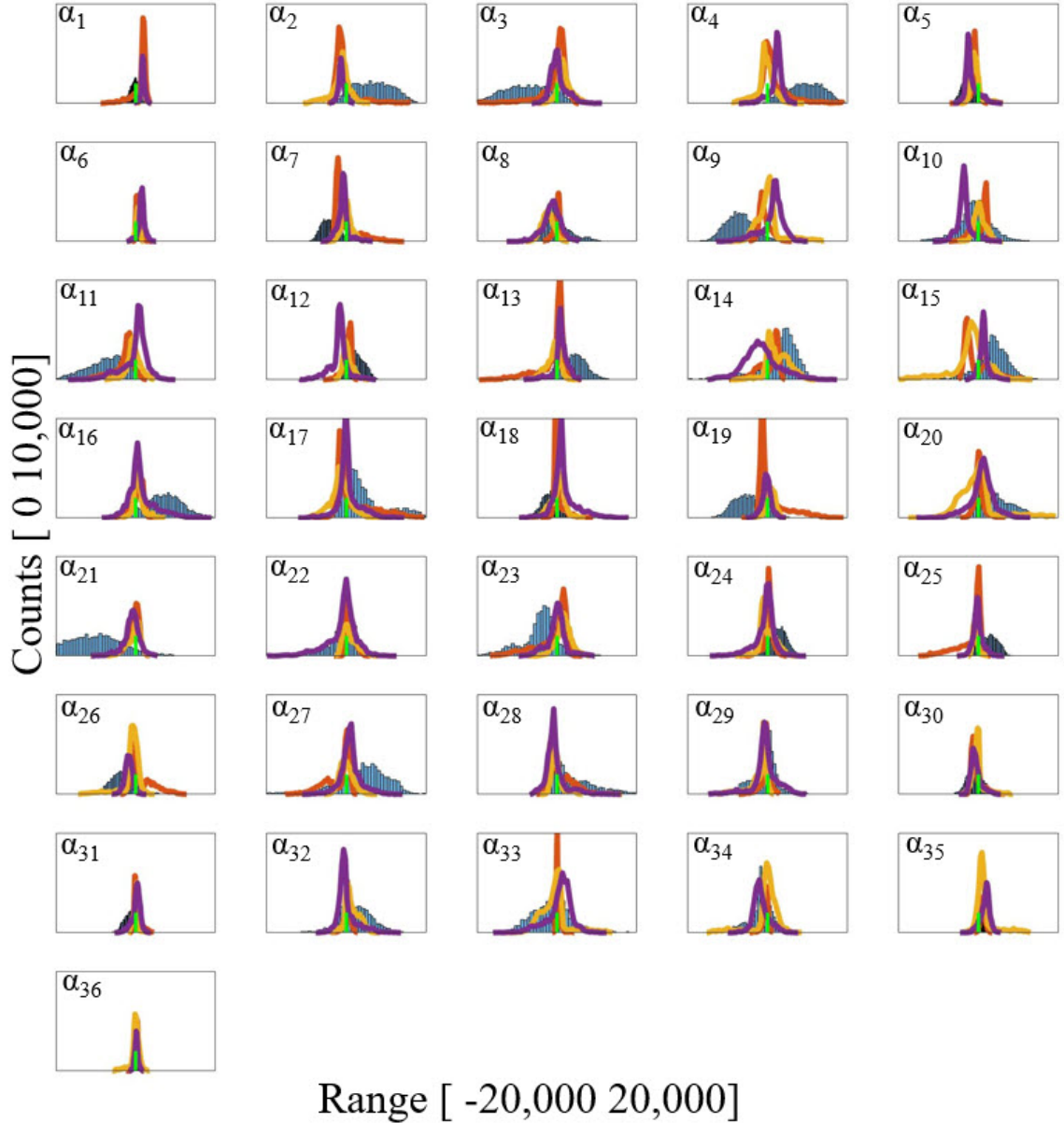


Figure 7.8: Histograms of the recovered $\vec{\alpha}$ coefficients for the four Markov chains computed for 100,000 iterations on the 36 DoF representation of the Pool 1 time-lapse anomaly. Each colored line represents a different chain, with a random chain selected to be the displayed histogram. The green line highlights the true value for the given coefficient.

First, we explore the latter, setting the algorithm to compute using the 25 DoF representation seen in Figure 7.7 c. Comparing the 25 DoF and 36 DoF representations in Figure 7.7, the overall velocity anomaly is similar. The main difference is that the 25 DoF representation lacks the dipping nature of the high-velocity feature. It

contains two separate velocity anomalies compared to the 36 DoF representation. The histograms of the recovered $\vec{\alpha}$ coefficients for the 25 DoF representation are shown in Figure 7.9. Similarly to Figure 7.8, the histograms for all four chains are not the same and do not have a mean in the confidence interval of the true value; therefore, the algorithm still has not converged to the correct model.

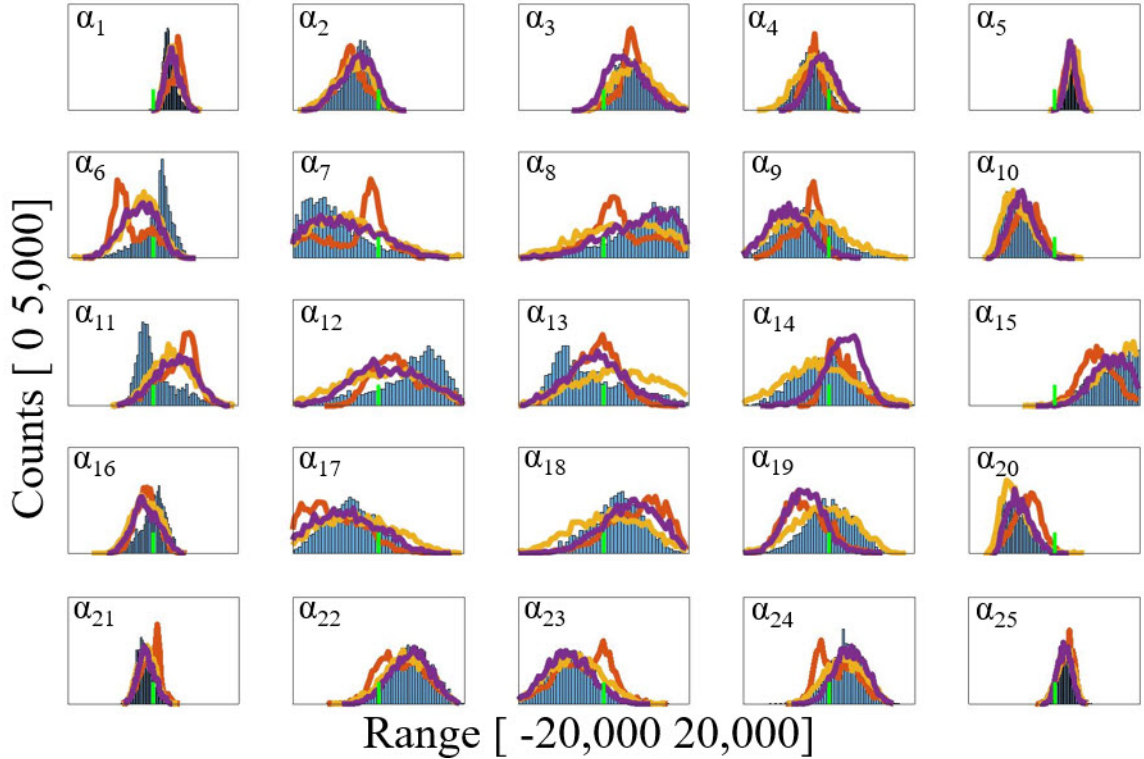


Figure 7.9: Histograms of the recovered $\vec{\alpha}$ coefficients for the four Markov chains computed for 100,000 iterations on the 25 DoF representation of the Pool 1 time-lapse anomaly. Each colored line represents a different chain, with a random chain selected to be the displayed histogram. The green line highlights the true value for the given coefficient.

Since decreasing the number of DoFs used to represent the Pool 1 time-lapse anomaly did not affect the algorithm’s ability to recover the true model, we move back to the 36 DoF representation of the anomaly and increase the number of iterations. Increasing the number of iterations to 250,000 per chain, we see that the histograms of the recovered $\vec{\alpha}$ coefficients for all four chains are the same; therefore the

algorithm has converged. We also see that the histograms for each of the $\vec{\alpha}$ coefficients, have a mean in the confidence range of the true value, indicating that the algorithm has arrived at the correct model. These 1,000,000 potential time-lapse changes are computed at 8 Hz frequency in 5.4 days with an acceptance rate of 13.5-16.0% on the same standard desktop (i7-6700 3.40 GHz processor and 16 GB memory). Compared to the previous computations, the acceptance rate has dropped by adding in more iterations but this is still considered to be a reasonable acceptance rate for the algorithm (Kotsi et al., 2020; Roberts & Rosenthal, 2001)

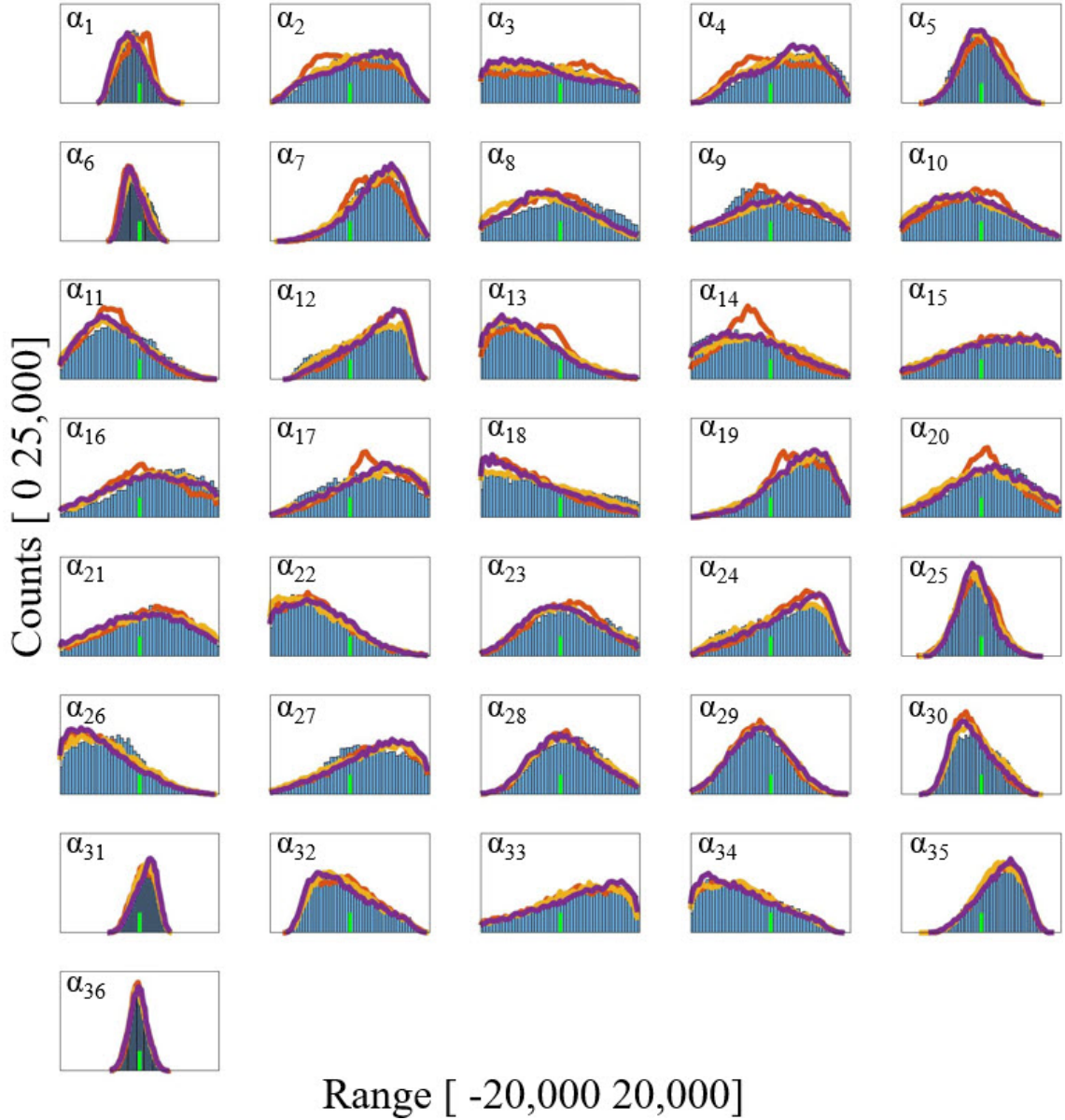


Figure 7.10: Histograms of the recovered $\bar{\alpha}$ coefficients for the four Markov chains computed for 250,000 iterations on the 36 DoF representation of the Pool 1 time-lapse anomaly. Each colored line represents a different chain, with a random chain selected to be the displayed histogram. The green line highlights the true value for the given coefficient.

We define quantities of interest (QoI) to interpret the magnitude and extent of the potential Pool 1 time-lapse anomalies recovered across all the accepted models for all four Markov chains. The QoI that we examine are the area of the velocity change within the local domain (fault block) and the average velocity of the local

domain (fault block); we select these QoI to describe the magnitude and extent of the overall time-lapse change recovered by the algorithm. Figure 7.11 shows the recovered histograms for these two QoI for the accepted models. The histograms for both the fault block area and average velocity calculation of the fault block converge with a mean in the confidence interval of the true value (green) across all four Markov chains, demonstrating that the potential time-lapse changes recovered for the Pool 1 anomaly accurately represent both the magnitude and extent of the true time-lapse change.

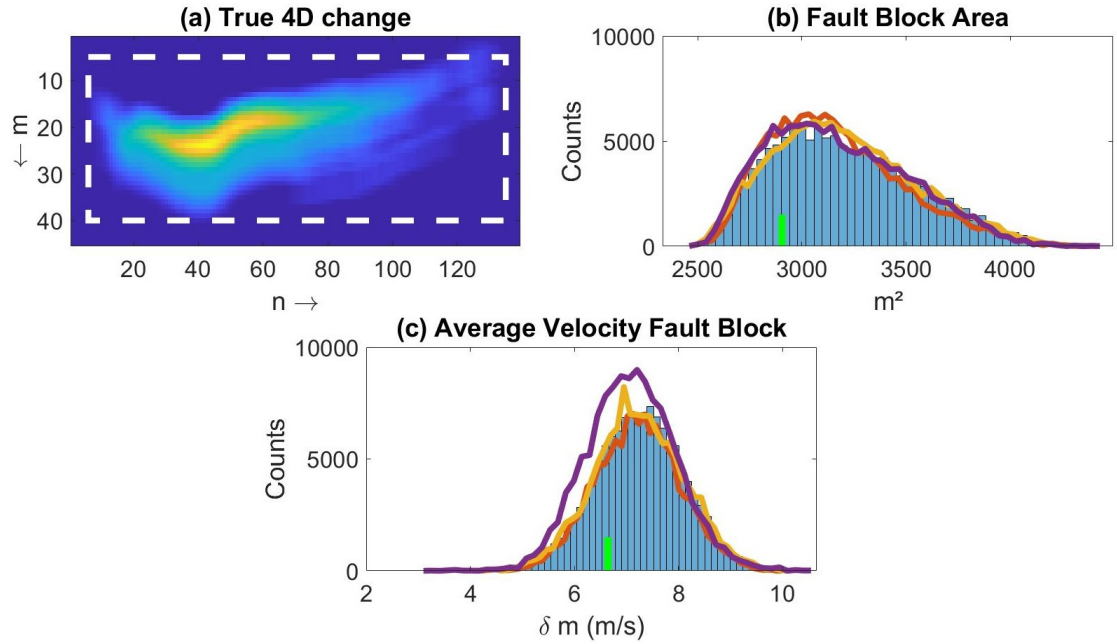


Figure 7.11: a) True Pool 1 time-lapse change with the white dashed line showing the portion of the local domain over which the area calculation was completed. b) Recovered histograms for the fault block/time-lapse change area calculation for the four Markov chains. Each colored line represents a different chain, with a random chain selected to be the displayed histogram. The green line highlights the true value for the given coefficient.

We use the \hat{R} criteria,

$$\hat{R} = \sqrt{\frac{\text{mean}(\text{var}_m)}{\text{var}_{mix}}}, \quad (7.22)$$

to assess the convergence of these QoI; the mean of the variance for a given QoI

for a Markov chain (var_m) is compared to the variance of the four Markov chains combined (var_{mix}) (Kotsi et al., 2020; Gelman & Rubin, 1992). Figure 7.12, shows the \hat{R} value for the three QoI for the 4 Markov chains computed for 250,000 iterations. QoI are said to have converged when the \hat{R} value is less than 1.1. For the Pool 1 time-lapse anomaly this occurs after $\sim 80,000$ iterations (Kotsi et al., 2020). Therefore, for the algorithm to accurately represent the magnitude and extent of the anomaly it requires only $\sim 80,000$ iterations versus the 250,000 iterations needed for the $\bar{\alpha}$ coefficients to converge.

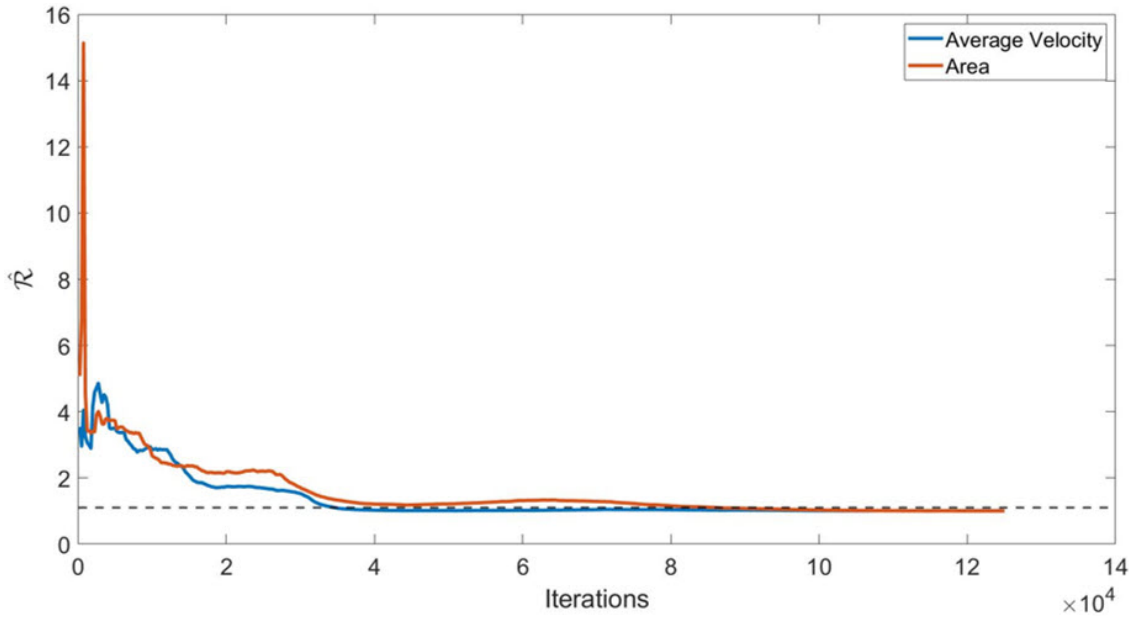


Figure 7.12: \hat{R} criteria for the average velocity and area QoIs for the four Markov chains computed at 250,000 iterations each. The dashed line is plotted at 1.1 to show the value at which the QoIs converge.

To visually examine potential time-lapse anomalies recovered from the algorithm, statistical measures such as the mean and maximum likelihood are plotted along with the standard deviation from an arbitrary Markov chain in Figure 7.13. Comparing the mean (Figure 7.13 b) and maximum likelihood (Figure 7.13 c) models to the 36 DoF representation (Figure 7.13 a), the main difference is that the entire anomaly is

compressed and shifted towards the upper right corner of the local domain (up-dip in the fault block). The shifting and compression of the anomaly is assumed to be due to only computing the time-lapse anomalies for a single 8 Hz frequency; a multi-frequency approach can be used to remedy this. The standard deviation (Figure 7.13 d) highlights areas of the model with the highest variability; these areas are located around the edges of the recovered high-velocity anomaly.

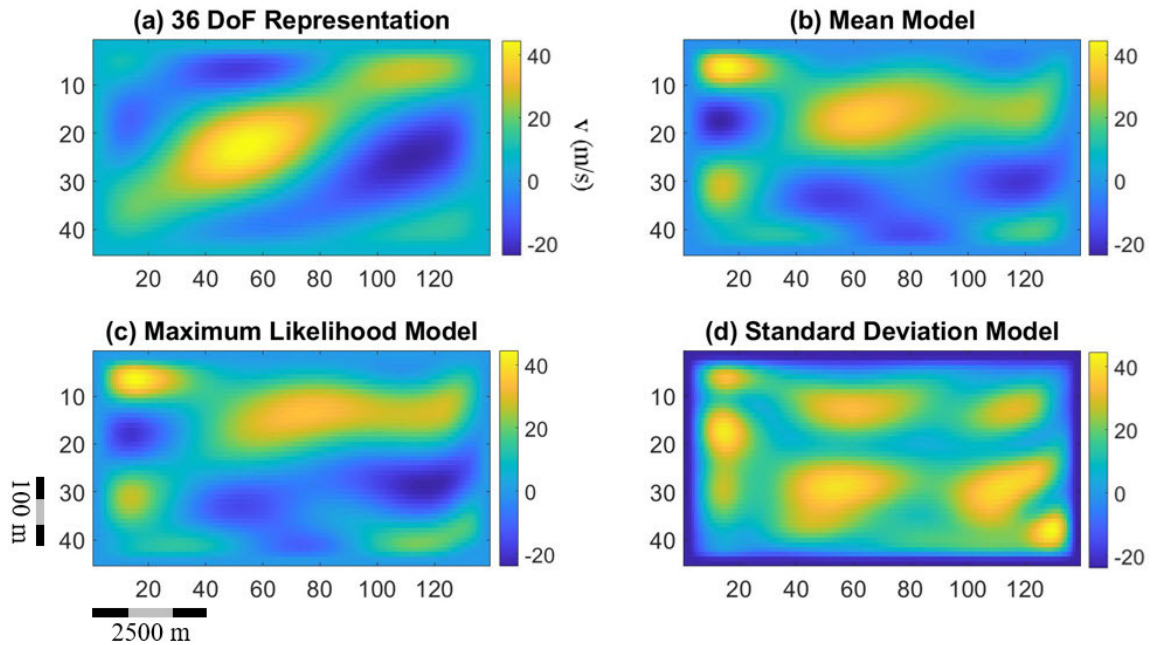


Figure 7.13: a) 36 DoF representation of the true Pool 1 time-lapse anomaly. b) Mean recovered model, c) maximum likelihood model, and d) standard deviation for an arbitrary Markov chain computed for 250,000 iterations. The plot area is the local domain which represents a 2D cross-section view of the Hebron fault block.

Chapter 8

Discussion

Using the subsurface perturbation due to simulated production of the Pool 1 reservoir of the Hebron field, 1,000,000 potential velocity perturbations are generated across four Markov chains. Highlighted in Figure 8.1 are different stages of the time-lapse anomaly from chapters 6 and 7 to illustrate the dialogue within this chapter.

8.1 Interpretation of the Time-Lapse Seismic Results

Overall, the recovered velocity estimates of the time-lapse anomaly (Figure 8.1 d) generated through the production simulation showed an increase in velocity due to the water injection into the Pool 1 reservoir. This velocity increase is stronger at the water injection locations (down-dip in the 2D fault block view) and this high magnitude velocity increase thins out and loses intensity towards the oil-producing locations (up-dip in the 2D fault block view); mirroring the structure of the true time-lapse anomaly seen in Figure 8.1 a. Since the water that is being injected into the reservoir has a higher P-wave velocity compared to the oil within the reservoir (Figure

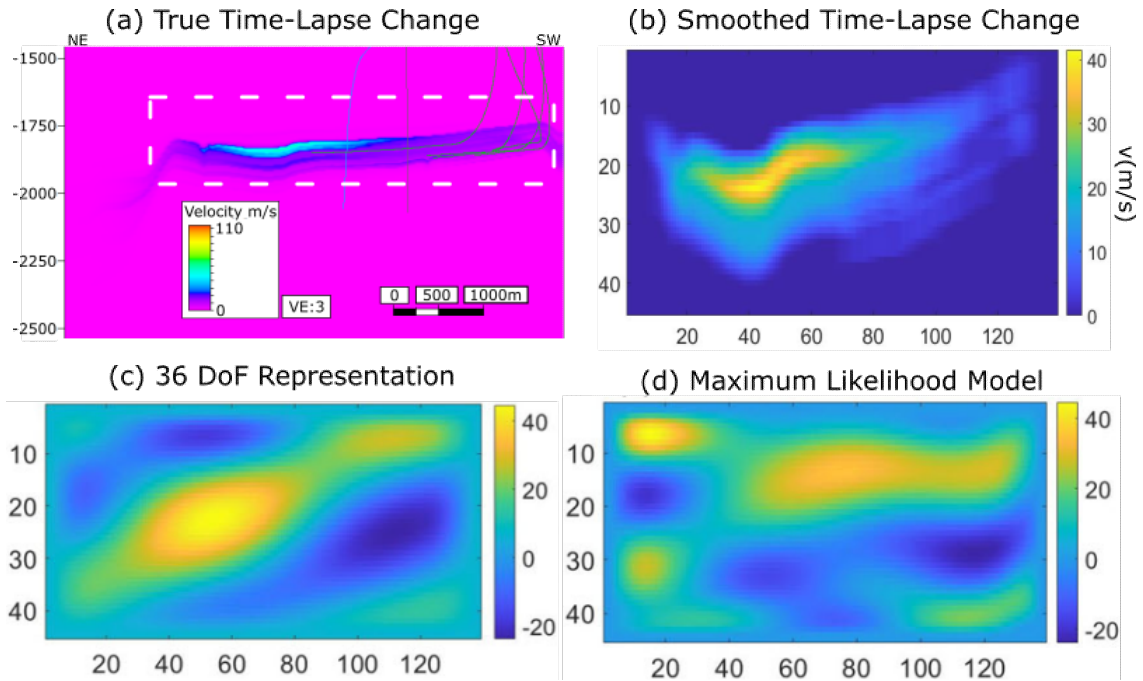


Figure 8.1: a) The true time-lapse anomaly within the Hebron fault block, with the approximate location of the local domain highlighted by the dashed white box. Note, the well locations on this seismic IL are being displayed out of plane (i.e locations of the wells are only approximate within the fault block). b) Smoothed true time-lapse anomaly within the Hebron fault block. c) 36 DoF representation of the time-lapse anomaly. d) Maximum likelihood velocity estimate for the time-lapse anomaly.

6.2), this velocity increase is interpreted to capture the movement of the injected water within the reservoir. The intensity of the injected water velocity anomaly is stronger in the down-dip portion of the Hebron fault block compared to the up-dip portion of the fault block; this is interpreted as water filling up the down-dip pores of the fault block, moving the hydrocarbons towards the up-dip oil-producing wells.

8.2 Implications of the Time-Lapse Seismic Uncertainty Quantification

These results showcase the potential velocity perturbation created from a waterflood of the Hebron Field Pool 1 reservoir after some intermediate amount of production.

Using uncertainty quantification, QoI representing the size (area) and magnitude (average velocity) of the time-lapse change caused by this waterflood of the Hebron fault block give end ranges on the potential velocity perturbations. These end ranges allow for a better understanding of 1) a potential seismic anomaly through the use of forward modeling and 2) provide an accuracy test using acquired time-lapse seismic anomalies to test the validity of a given reservoir simulation model. Applying uncertainty quantification to time-lapse feasibility studies (situation 1) creates a more accurate feasibility study by incorporating data uncertainties into the model. Forward modeling the recovered end ranges of the velocity perturbation would generate a more robust and accurate representation of a potential production-induced time-lapse anomaly. Situation 2 works similarly to situation 1; the method can be used to test reservoir simulation models generated from up-to-date production data against an acquired time-lapse anomaly through a repeat seismic survey (monitor survey). This situation has two benefits for a production geoscience team; it tests the accuracy of the subsurface model generated through the reservoir simulation data. It also models the end ranges for the given anomaly to allow for a more accurate interpretation of the time-lapse seismic data by better understanding the uncertainties associated with the data.

8.3 Limitations to the Time-Lapse Seismic Uncertainty Quantification Study

There are two important limitations on the results shown in this study. The first is using a percentage-based fluid substitution over a reservoir simulation to create the time-lapse anomaly. The second is using only a single frequency while generating the model perturbation seismic data at each iteration of the uncertainty algorithm.

The use of a percentage-based fluid substitution is solely due to the lack of available production data. Ideally, a synthetic forward modeling time-lapse study such as this would be a joint effort of multiple disciplines (geosciences and reservoir engineering) to utilize production-data-based reservoir simulations to generate updated saturation logs for a reservoir. These logs would represent the fluid properties at given well locations and would replace the percentage-based change used in the fluid substitution shown in this thesis. The premise of the fluid substitution is the same as the percentage-based approach used in this thesis, which is in theory less accurate at representing the subsurface rock properties compared to the reservoir simulation method. The actual fluid substitution method stays the same, the ratios of fluids would differ; thus, the velocities used in this thesis are as accurate as they can be using this percentage approach. Overall, these reservoir-simulation-based fluid saturations would better represent the subsurface properties that would be imaged through a monitor survey, thus providing a more accurate velocity perturbation for Pool 1 of the Hebron Field than the method used in this thesis.

The second limitation of this study is only computing the local domain perturbed wavefield for a single 8 Hz frequency. Ideally, the data should have been computed using a multi-frequency approach similar to FWI. The background model data (i.e. area outside of the local domain) is computed for 2, 4, 6, 8, and 10 Hz; doing the same for the local domain data, in theory, would have generated recovered statistical time-lapse models closer to Figure 8.1 c. This would likely remove the compression and shifting up-dip of the anomaly seen in the single 8 Hz frequency model. We would also expect to see an increase in the resolution of the recovered $\vec{\alpha}$ coefficients histograms. Figure 7.10 contains relatively flat histograms (i.e. low resolution), indicating that we are not confident which model the algorithm has converged to. However, we are

confident that all the $\vec{\alpha}$ coefficients have converged to the same model. We leave the computation of the local domain perturbed wavefield with multiple frequencies for future work.

An additional limitation that is worth explicitly mentioning for this study is the lack of amplitude information for the baseline seismic data in this study. Generally, we interpret 4D seismic on an amplitude difference 3D seismic cube generated from the monitor and baseline surveys. Since we do not have a monitor survey for the Hebron field and we lack amplitude information for the baseline survey, we can not interpret the data shown in this study this way. We can, however, analyze the results of the velocity estimates for the time-lapse velocity perturbation (Section 8.1). When coupled with the industry-standard technique of amplitude difference interpretations, these additional velocity estimate interpretations can give a working reservoir geoscientist invaluable uncertainty quantification measurements and a better understanding of a producing fields remaining reserves.

8.4 Additional Applications of the Time-Lapse Seismic Uncertainty Quantification Method

Uncertainty quantification methods can be used in other geophysical situations within the petroleum industry. Two examples of this are using UQ in a forward modeling based scenario to predict the correct timing to acquire a monitor 3D seismic survey or in a de-risking scenario to understand end ranges of seismic data to update the geological chance of success (GCOS) of a given prospect/geological target.

8.4.1 Forecast Ideal Timing for Monitor Seismic Survey(s)

The uncertainty quantification algorithm showcased in this thesis could be leveraged to predict the best timing for a monitor 3D seismic survey through forward modeling. The case shown in this thesis was applying the uncertainty quantification algorithm to a completely synthetic percentage-based fluid substitution perturbation to the subsurface representing the replacement of hydrocarbons by injected water. One could forecast a reservoir simulation history matching the model using up-to-date production data to generate updated fluid saturation ratios for a target reservoir. These fluid saturations can then be used in a Gassmann's fluid substitution (Equation 6.1) to generate a potential velocity model representing the producing field at a selected time in the future. This algorithm can be used to determine the end ranges of potential velocity perturbations in the subsurface due to the change in the subsurface rock properties, using seismic forward modeling with synthetic seismic data representing the potential monitor model that can be generated. These data can then be assessed in a time-lapse feasibility study to determine the usefulness of a potential monitor survey at the selected time in the field production life.

8.4.2 De-risking Geological Targets

In both the exploration and production scenarios, uncertainty quantification can be used to better understand a geological target by updating probabilistic reserves of a reservoir/exploration target (P10, P50, P90). Updating these probabilistic reserves through uncertainty quantification can alter the geological chance of success (GCOS) of a geological target. Since these probabilistic reserves are calculated through a volumetric estimation derived through seismic data, understanding the uncertainty and end ranges on what the subsurface could potentially look like is an enormous

advantage when calculating the probabilistic reserves. Accurately calculating these probabilistic reserves will directly impact the GCOS of every geological target (either increasing or decreasing it) allowing for a geoscience team to make better informed business decisions leading to more successful exploration wells and a more lucrative exploitation of a hydrocarbon field.

Chapter 9

Conclusions and Future Work

9.1 Conclusions

Through the use of a 4D multi-parameter adaptive Metropolis-Hastings seismic uncertainty quantification algorithm, the uncertainty of a synthetic production induced velocity perturbation for the Hebron Field was assessed within this thesis. The synthetic velocity perturbation is added to a full field 3D velocity model generated for the Hebron Field through seismic interpretations and well log data. This perturbation is calculated through a Gassmann's fluid substitution on production wells (oil producers and water injectors) drilled in the targeted Pool 1 reservoir of the Hebron Field. The fluid ratios in the post-production velocity model are generated using a percentage-based fluid change, leading to perturbed P-wave velocity logs representing an intermediate stage in the life cycle of the waterflood of the Pool 1 reservoir. The velocity perturbation generated due to the simulated production is computed using a discrete cosine transform (DCT) to lower the number of parameters/degrees of freedom (DoF) to a reasonable number (36 DoF) so that the Markov chain Monte Carlo algorithm can sufficiently search the predefined model space.

The 4D multi-parameter adaptive Metropolis-Hastings algorithm utilizes repeated sampling through four Markov chains computed at 250,00 iterations each (1,000,000 total iterations) to quantify the uncertainty in a recovered velocity anomaly due to the production of the Pool 1 reservoir of the Hebron Field. Quantities of interest (QoI) are defined to showcase the algorithm’s ability to represent the size/shape (area) and the magnitude (average velocity) of the velocity perturbations to compare the recovered models to the true induced synthetic velocity perturbation. Statistical models are plotted for each chain to visually inspect the recovered mean and maximum likelihood velocity perturbation compared to the 36 DoF representation. Compared to the 36 DoF representation, these models are compressed and shifted up-dip with regards to the Hebron fault block, likely due to the single 8 Hz frequency used during the computation of the Markov chains. Increasing the number of frequencies used would also likely increase the resolution of the recovered $\vec{\alpha}$ coefficient histograms.

Overall, it has been shown that repeated sampling through this 4D multi-parameter adaptive Metropolis-Hastings algorithm generated end ranges on a potential production induced subsurface perturbation for the Hebron Field located in the Jeanne d’Arc Basin offshore Newfoundland Labrador. These end ranges can be used to better understand the uncertainty in an acquired time-lapse seismic response for the Hebron Field, allowing for a more accurate time-lapse interpretation to be made.

9.2 Future Work

As previously mentioned, there are a few additional ways to improve the results shown in this thesis. The first step to improve the results would be to implement a multi-frequency approach to computing the perturbed data for the local domain similar to that of FWI compared to the single 8 Hz frequency approach shown in

this thesis. Upgrading the induced production anomaly from a percentage-based fluid substitution to one derived from a reservoir simulation would increase the accuracy of the recovered velocity perturbations tested for the Hebron Field. Furthermore, having access to a real acquired monitor 3D seismic survey for the Hebron Field to quantify the uncertainty of the time-lapse response acquired over the field would be extremely useful to test the accuracy of the recovered perturbations and the history-matched reservoir model for the field. Incorporating reservoir pressure changes due to the production of the reservoir would further increase the accuracy of the time-lapse anomaly for the field.

Bibliography

- Asnaashari, A., Brossier, R., Garambois, S., Audebert, F., Thore, P., & Virieux, J., 2015. Time-lapse seismic imaging using regularized full-waveform inversion with a prior model: which strategy?, *Geophysical prospecting*, **63**(1), 78–98.
- Brooks, S., Gelman, A., Jones, G., & Meng, X.-L., 2011. *Handbook of markov chain monte carlo*, CRC press.
- CGG, 2015a. 2015 hebron two component isometrix tti anisotropic depth migration processing report.
- CGG, 2015b. Processing report appendix 44 - 2013 hebron conventional tti apsdm velocity model building overview.
- Core Laboratories, 1981. Core analysis.
- Core Laboratories, 1999. Core analysis report for petro-canada oil and gas petro-canada et al hebron d-94 hebron, newfoundland.
- Core Laboratories, 2000. Core analysis report for jeanne d'arc basin operations chevron et al hebron m-04 hebron, newfoundland.
- Cornaglia, V. & McNeill, A., 2018. Geoscience Overview of the Hebron Field, *OTC Offshore Technology Conference*.

- DeSilva, N., 1999. Sedimentary basins and petroleum systems offshore newfoundland and labrador, *Geological Society, London, Petroleum Geology Conference series*, **5**(1), 501–515.
- Dickie, K., Keen, C. E., Williams, G. L., & Dehler, S. A., 2011. Tectonostratigraphic evolution of the labrador margin, atlantic canada, *Marine and Petroleum Geology*, **28**(9), 1663–1675.
- Ely, G., Malcolm, A., & Poliannikov, O. V., 2018. Assessing uncertainties in velocity models and images with a fast nonlinear uncertainty quantification method, *Geophysics*, **83**(2), R63–R75.
- Enachescu, M., 1987. Tectonic and structural framework of the northeast newfoundland continental margin, in *Publication Sedimentary Basins and Basin-Forming Mechanisms*, vol. 12, pp. 117–146, CSPG Special Publications.
- ExxonMobil, 2011. Hebron project development plan.
- ExxonMobil, 2019. Hebron 2013 3d seismic reflection survey - report of initial geophysical interpretation.
- Fowler, M. & McAlpine, K., 1995. The egret member, a prolific kimmeridgian source rock from offshore eastern canada, in *Petroleum source rocks*, pp. 111–130, Springer.
- Gelman, A. & Rubin, D. B., 1992. Inference from iterative simulation using multiple sequences, *Statistical science*, **7**(4), 457–472.
- Haario, H., Saksman, E., & Tamminen, J., 2001. An adaptive metropolis algorithm, *Bernoulli*, **7**(2), 223–242.
- Johnston, D. H., 2013. *Practical applications of time-lapse seismic data*, Society of Exploration Geophysicists.

- Kearey, P., Brooks, M., & Hill, I., 2002. *An introduction to geophysical exploration*, John Wiley & Sons.
- Kotsi, M., 2020. *Time-Lapse Seismic Imaging and Uncertainty Quantification*, Ph.D. thesis, Memorial University of Newfoundland.
- Kotsi, M., Malcolm, A., & Ely, G., 2018. 4d full-waveform metropolis hastings inversion using a local acoustic solver, in *SEG Technical Program Expanded Abstracts 2018*, pp. 5323–5327, Society of Exploration Geophysicists.
- Kotsi, M., Edgar, J., Malcolm, A., & de Ridder, S., 2019a. Combining reflection and transmission information in time-lapse velocity inversion: A new hybrid approach, *Geophysics*, **84**(4), R601–R611.
- Kotsi, M., Malcolm, A., & Ely, G., 2019b. 4d multiparameter adaptive metropolis hastings inversion, in *SEG Technical Program Expanded Abstracts 2019*, pp. 5290–5294, Society of Exploration Geophysicists.
- Kotsi, M., Malcolm, A., & Ely, G., 2020. Uncertainty quantification in time-lapse seismic imaging: a full-waveform approach, *Geophysical Journal International*, **222**(2), 1245–1263.
- Liner, C. L., 1999. *Treatise of Petroleum Geology/Handbook of Petroleum Geology: Exploring for Oil and Gas Traps*, chap. 12: Interpreting Seismic Data, pp. 12–1 – 12–30, AAPG Special Volumes, The American Association of Petroleum Geologists.
- Lumley, D., Adams, D. C., Meadows, M., Cole, S., & Wright, R., 2003. 4d seismic data processing issues and examples, in *SEG Technical Program Expanded Abstracts 2003*, pp. 1394–1397, Society of Exploration Geophysicists.

- Lumley, D. E., 2001. Time-lapse seismic reservoir monitoring, *Geophysics*, **66**(1), 50–53.
- Lumley, D. E., Behrens, R. A., & Wang, Z., 1997. Assessing the technical risk of a 4-d seismic project, *The Leading Edge*, **16**(9), 1287–1292.
- MacRae, A., 2001. Tif2segy, http://seismic.ocean.dal.ca/~seismic/pwp_wiki/static/Tif2segy.html, Accessed: 2020-02-13.
- Magoon, L. B., Hudson, T. L., & Peters, K. E., 2005. Egret-hibernia (!), a significant petroleum system, northern grand banks area, offshore eastern canada, *AAPG bulletin*, **89**(9), 1203–1237.
- McAlpine, K. D., 1990. *Mesozoic Stratigraphy, Sedimentary Evolution, and Petroleum Potential of the Jeanne D'Arc Basin, Grand Banks of Newfoundland*, Geological Survey of Canada Ottawa.
- McIlroy, C., 2014. *Development of extension over time during rifting of the Jeanne d'Arc Basin, offshore Newfoundland*, Master's thesis, Memorial University of Newfoundland.
- Miller, H. G. & Singh, V., 1995. The avalon terrane of newfoundland: geophysical correlations from onshore to offshore as evidence for precambrian to tertiary structural evolution, *Tectonophysics*, **242**(3-4), 183–197.
- Naess, O. E., 2006. Repeatability and 4d seismic acquisition, in *SEG Technical Program Expanded Abstracts 2006*, pp. 3300–3304, Society of Exploration Geophysicists.
- Plessix, R.-E., Michelet, S., Rynja, H., Kuehl, H., Perkins, C., de Maag, J., & Hatchell, P., 2010. Some 3d applications of full waveform inversion, in *72nd EAGE Confer-*

- ence and Exhibition-Workshops and Fieldtrips*, pp. cp-162, European Association of Geoscientists & Engineers.
- Pratt, R. G., 1999. Seismic waveform inversion in the frequency domain, part 1: Theory and verification in a physical scale model, *Geophysics*, **64**(3), 888–901.
- Roberts, G. O. & Rosenthal, J. S., 2001. Optimal scaling for various metropolis-hastings algorithms, *Statistical science*, **16**(4), 351–367.
- Shank, J., 2020. private communication.
- Sinclair, I., 1992. *Petroleum resources of the Jeanne d’Arc Basin and environs, Grand Banks, Newfoundland*, 92-8, Geological Survey of Canada.
- Sinclair, I., Shannon, P., Williams, B., Harker, S., & Mooren, J., 1994. Tectonic control on sedimentary evolution of three north atlantic borderland mesozoic basins 1, *Basin Research*, **6**(4), 193–217.
- Srivastava, S., Verhoef, J., & Macnab, R., 1988. Results from a detailed aeromagnetic survey across the northeast newfoundland margin, part ii: Early opening of the north atlantic between the british isles and newfoundland, *Marine and Petroleum Geology*, **5**(4), 324–337.
- Tankard, A., Welsink, H., & Jenkins, W., 1989. *Structural Styles and Stratigraphy of the Jeanne d’Arc Basin, Grand Banks of Newfoundland: Chapter 17: North American Margins*, AAPG Special Volumes, American Association of Petroleum Geologists.
- Tucholke, B. E. & Sibuet, J.-C., 2007. *Leg 210 synthesis: Tectonic, magmatic, and sedimentary evolution of the Newfoundland-Iberia rift*, vol. 210, pp. 1–56.

- Van Avendonk, H. J., Holbrook, W. S., Nunes, G. T., Shillington, D. J., Tucholke, B. E., Loudon, K. E., Larsen, H. C., & Hopper, J. R., 2006. Seismic velocity structure of the rifted margin of the eastern grand banks of newfoundland, canada, *Journal of Geophysical Research: Solid Earth*, **111**(B11).
- Vernik, L., 2016. *Seismic petrophysics in quantitative interpretation*, Society of Exploration Geophysicists.
- Virieux, J. & Operto, S., 2009. An overview of full-waveform inversion in exploration geophysics, *Geophysics*, **74**(6), WCC1–WCC26.
- Welford, J. K., Shannon, P. M., O’Reilly, B. M., & Hall, J., 2012. Comparison of lithosphere structure across the orphan basin–flemish cap and irish atlantic conjugate continental margins from constrained 3d gravity inversions, *Journal of the Geological Society*, **169**(4), 405–420.
- WesternGeco, 2013. Final field operation report: 2013 hebron 3d/4d baseline seismic survey.
- Willemsen, B., Malcolm, A., & Lewis, W., 2016. A numerically exact local solver applied to salt boundary inversion in seismic full-waveform inversion, *Geophysical Journal International*, **204**(3), 1703–1720.
- Wright, R. J., 2004. *4D seismic analysis of the Hibernia oil field, Grand Banks, Canada*, Ph.D. thesis, Memorial University of Newfoundland.
- Zhang, Z. & Huang, L., 2013. Double-difference elastic-waveform inversion with prior information for time-lapse monitoring, *Geophysics*, **78**(6), R259–R273.